Development of a predictive model for the VAPEX process.

by

James Lowman

A thesis
presented to the University of Waterloo
in fulfilment of the
thesis requirement for the degree of
Master of Applied Science
in
Chemical Engineering

Waterloo, Ontario, Canada, 2018

I hereby declare that I am the sole author of this thesis. This is a true copy of the thesis, including any required final revisions, as accepted by my examiners.

I understand that my thesis may be made electronically available to the public.

Abstract

Heavy oil in-situ recovery in Canada is largely achieved through energy intensive and environmentally detrimental steam assisted gravity drainage (SAGD). By exchanging steam for a vapour solvent, it has been shown experimentally that heavy oil recovery can be achieved with a significant reduction in both energy requirements and environmental impact. This project presents a model for predicting production rates for the vapour extraction (VAPEX) process developed using first principles. The governing equations are solved using the pseudo-spectral Chebyshev collocation method. Simulations replicating experimental results, a detailed derivation of the model, a discussion of model parameters, and numerical analysis of the solution are presented in this thesis.

Acknowledgements

Dedication

Thank you Emma. You were very patient with me for this part of our lives. It cannot be easy to live with someone sits in front of a computer for a living than complains of the "stress of it all." But you were a best friend and great partner through it all.

Thank you Tanya for having the patience to answer all of my inane questions for the last two years, this project would never have existed without your knowledge and expertise. You are the unsung hero of our team. Thank you to Tanya, Jake, Victor, Fred, and Ryan for being fun room-mates and intelligent sounding boards.

Thank you to Nasser and Marios for gambling on me. I struggled in getting grades that would make me shine on paper for a grad school application, but you both saw promise and were willing to stick your necks out to give me chance. I will be eternally grateful to you both. I hold you both in the highest regard as people, and academics, and I hope we find ways to work together in the future.

Table of Contents

List of Tables

List of Figures

Chapter 1

Introduction

Our society is built on energy storage. Cave dwellers gathered stored energy in the form of wood in order to cook and preserve game, achieving rates of protein intake that allowed for our brains to develop. Once we had determined how to produce an abundance of food, energy was stored in grain silos allowing a population's daily caloric intake to be stable year round. Early in the nineteenth century hydroelectric projects stored energy in gravitational potential to later generate electricity, and suddenly we could keep perishable food in our houses and read at night. The most impressive energy storage schism has been the combustible hydrocarbon. It has provided the energy to travel anywhere in the world in less then a day, to ship items unimaginable in some climates so they can be purchased for pennies across the globe, to even explore outer space.

After a century of exploiting easy-to-retrieve light crude oil sources, demand has increased. Reservoirs with more difficult to retrieve oil must be tapped. The Canadian tar sands offer an immense reserve of heavy oil and bitumen trapped in unconsolidated porous media. Easy to access, shallow reserve bitumen can be mined and refined, but the largest reserves are found at depths that make surface mining impractical and unprofitable [9]. Methods have been devised and implemented that can extract deep bitumen in-situ by means of viscosity reduction. The most common and highest producing of these methods is steam-assisted-gravity-drainage (SAGD) which, unfortunately, has an extreme environmental cost in energy consumption, carbon output, and the contamination of large quantities of freshwater.

Until such a time when oil is no longer the most depended upon form of energy storage, more environmental methods of viscosity reduction must be implemented in order to make feasible the extraction of heavy oil and bitumen from the Canadian tar sands. Using a

gas phase solvent, laboratory experiments have shown great promise in in-situ bitumen upgrading and viscosity reduction. The method is called VAPEX, a contraction of vapour extraction.

1.1 Objectives and scope

Attempts to model VAPEX have fallen short of truly predictive solutions. Reasons for failure include making assumptions that ignore important physics, simplifying the non-linear system by reducing the resulting model to a linear system of equations, or assuming geometric restrictions to compensate for a tough to solve equation. The original work on VAPEX, both experimental and mathematical, by Butler and Mokrys [10] was based on an analogue liquid solvent (Toluene) and ignored capillarity. Subsequent work by the same authors on solvent assisted gravity drainage experiments with vapour butane also ignored the role of capillary forces. Not including an equation that governs flow in a system requires one to assume the shape that the solvent chamber forms as VAPEX removes bitumen from the system. Without known velocities from a flow equation in the domain, both advection and dispersion of the solvent/bitumen mixture have been either ignored or approximated in subsequent models. A model including both flow and mass transfer was tested at Waterloo by Tam [1]. Issues arose in implementation of this model that required a simplification of physical phenomena in order to achieve convergence in the software package employed. Changes in capillarity due to reduction of interfacial tension between the two phases had to be crudely approximated with a Heaviside step function, and dispersion/diffusion was assumed velocity independent. There has been little research into inter-phase mass transfer in the VAPEX system, requiring an approximation in Tam's model based on non-aqueous-phase liquid mass transfer as the only available analog.

The overall aim of this research project is to address the challenges of solving a complex physics based model of VAPEX. Through the development and numerical solution of a continuum model which will include all of the physical phenomena that have been neglected in the past, a transient two-dimensional non-linear partial differential equation (PDE) system is developed. Attempting to solve this model using conventional numerical methods, such as the finite-volume and finite-element methods, is difficult. The Chebyshev spectral collocation method is presented as suitable method for such complexity. This thesis describes the model derivation, numerical methods, validation against experimental data of a suitable model for the VAPEX process.

The specific objectives of the thesis are to develop the VAPEX model from first principles. The model is then populated with independently determined fluid and porous media

2

properties. The system is then be solved using a custom written Chebyshev collocation solver, and the results are validated against previous VAPEX experimental studies.

The thesis is organized into the following chapters: introduction, literature review, model derivation, solution setup, results and discussion, and conclusions.

The literature review chapter discusses the history of oil recovery, specifically relating to Canadian reserves. The techniques for enhanced oil recovery are discussed with a focus on steam assisted gravity drainage and the subsequent development of VAPEX. The physical phenomena that are observed in a VAPEX system are discussed as theory and models are examined. A study into the earliest derivation of a VAPEX model will be conducted and discussion on how that model has permeated the narrative since.

The model derivation chapter will show the first principles development of the VAPEX model presented in this thesis. The choice of empirical correlations is justified and included into the model for viscosity, diffusion, dispersion, capillary pressure, interfacial tension, permeability scaling, and relative permeability. A derivation and justification of an approximation to the physics of interfacial mass transfer is discussed in detail.

The chapter titled "Solution Setup" defines how this problem is resolved with respect to the methodology on the numerical solution, as well as the domains, boundary conditions, and initial conditions. An outline of the Chebyshev spectral collocation method restrictions and conditions are described, and a brief introduction into the non-linear solver utilized to solve the system of PDE's is outlined. The boundary conditions for the domain to properly capture the VAPEX system is detailed, and the unique initial conditions required by the spectral method are justified physically. The requirements for a solution at detailed as they pertain to certain physical inputs from the well one wishes to model.

The results and discussion chapter will tackle the validation of the numerical method and of the VAPEX model. The results of the model solution are validated against experimental data. A deconstruction of the contributions of interphase mass transfer is discussed and reviewed in depth. Agreements and deviations from experimental data are discussed, and future work will be suggested.

Chapter 2

Background and Literature Review

2.1 A brief history of oil recovery

Refined animal fat and whale blubber burns bright enough to see in the dark. The concept of oil pre-dates the extraction of it from the ground to use as an energy source. A quote from the Greek epic The Iliad by Homer "and the Trojans cast upon the swift ship unwearied fire, and over her forthwith streamed a flame that might not be quenched. So then was the ship's stern wreathed about with fire, but Achilles smote both his thighs and spake to Patroclus: 'Up now, Zeus-born Patroclus, master of horsemen. Lo, I see by the ships and there be no more escaping!'", implies a flamed acceleratant was used by the Trojans to defend the city, which the demigod Achilles used a lamp with which to continue fighting. Oil as a product has roots in ancient history.

Having an in-demand product without a cheap viable source does not make for good business. There is evidence of natural gas being discovered, transported in bamboo pipelines, and used in China in 600 B.C [11]. This might be the first production and utility of hydrocarbons found in the ground, but the production techniques and ability to scale were lacking. Light crude oil is a flowing black oil that is easy to move, is usable out of the ground, and can be easily refined in to other petroleum products. Some wells would produce light crude by simply placing a bucket down a hole and waiting for the crude to collect. Edwin Drake had access to such a source in Pennsylvania in 1859 [11], and developed a new drilling method with which to extract it in quantities large enough to create a new industry of energy-on-demand for prices previously unachievable.

The Chinese method for salt drilling was responsible for those early discoveries of flammable gasses [11]. They were interested in brine, and devised a method to drill deep

into salt deposits. While drilling they discovered a flammable gas would sometimes pour out of the new well bore. They were able to utilize this gas resource. Drake saw the merit of the methods employed by the salt drillers, and borrowed upon the technique in 1860 to develop the first true production scale oil field opening up a whole new energy industry. He incorporated these unique drilling techniques to drive through the water table and cap rock, tapping into huge reservoirs of easy to pump light crude.

The idea of oil as marketable source of energy, and the ease of access in the Pennsylvania fields made a useful source of energy into a black-gold-rush for prospectors and industry alike. By 1862 roughly three million barrels of light crude was being produced in Pennsylvanian wells [11]. Word spread to Europe of the now cheap and very usable oil, fuelling more speculation and eventually a worldwide addiction to the new world's hydrocarbon riches.

Light crude sources were discovered the world over and exploited during the next century. As new discoveries become fewer and farther between [12], the days of drilling into a pressurized well and reaping the oil or by simply pumping it out are growing short. A change in technology is looming. Techniques are improving to harness difficult hydrocarbon sources in order to squeeze every drop out of the ground.

2.1.1 Exploiting oil reservoirs

Oil recovery can be divided into three phases [13]: primary, secondary, and tertiary recovery. Primary indicates the natural drive mechanisms like pressure already present in a reservoir pushing the oil out the well. Secondary refers to introducing pressure into a well to maintain production. Tertiary recovery are the techniques utilized after primary and secondary methods are fully exploited.

Enhanced oil recovery (EOR) is the act of retrieving oil by means of introducing a substance into a reservoir to coax out production. There are numerous techniques to accomplish such a feat like using thermal energy to reduce the viscosity of remaining oil, or introduction of solvents to mimic the same result.

EOR is not necessarily a last resort of of a depleted well. Many EOR techniques are being field tested for primary production of harder to access reserves [13]. As the availability of light crude diminishes, EOR is being hailed as the new counterbalance in oil production.

2.1.2 Prohibitive viscosity: bitumen and heavy oil

Oil comes in many forms, and from many sources. Light crude has variable viscosity, which in a study tended to an average of $6 \times 10^{-4} \ kg/m \cdot s$ at reservoir conditions [14], making it less viscous than water. On the opposite scale is bitumen with a viscosity in the order of $1 \times 10^2 \ kg/m \cdot s$ [15], immobile enough to be approximated as a solid. The Canadian tar sands, situated in Northern Alberta and parts of Saskatchewan, offer a wealth of petroleum reserves trapped in heavy oil or bitumen form. This resource has been utilized since before European colonizers ventured west, most notably by First Nations peoples as a caulking for canoes. They extracted bitumen from the Athabasca River sands by boiling soil and separating the solids from the liquid. A refining technique that lead to a sample of bitumen being given to the Hudson's Bay Company in 1719 by a First Nations leader Wa-Pa-Su [16].

Bitumen is so viscous it will not flow in productive time-scales unless its viscosity is reduced. To get it out of the ground and refined, two types of extraction exist: mining, and enhanced oil recovery.

Mining digs raw bitumen-laden-soil out of the ground as fast as possible, and is only profitable in areas where the bitumen is found near the surface. EOR is utilized for in-situ production by injecting something into the well in order to reduce the viscosity, ultimately being able to be pumped out of the ground. As a majority of Canadian bitumen is found in deep reservoirs (estimates indicate 80% of Canadian bitumen is too deep to be mined [17]), reducing viscosity is a requirement of hydrocarbon production in western Canada.

2.1.3 Environmental impact of bitumen recovery

Mining bitumen involves stripping out stratified soil layers containing the trapped hydrocarbon. The entire field is dug up and processed (see Fig. 2.2). The soil is detached from the bitumen and returned to the ground [18]. Water is used in large quantities in order to remove the hydrocarbons from the bitumen ladened soil by means of steam. Somewhere between 1.5 to 4 barrels of water per barrel of bitumen produced [19] are required for this separation. The by-product water from this process includes naphthenic acids and trace metals which must be disposed of. Temporary storage in tailing ponds is required as the by-products are toxic to plant and animal life [20] making them unfit to be returned into the environment without processing. It is estimated that upwards 720 billion litres of water is stored in such tailings ponds [17], and that a possible 11 million litres a day are leaking [19].
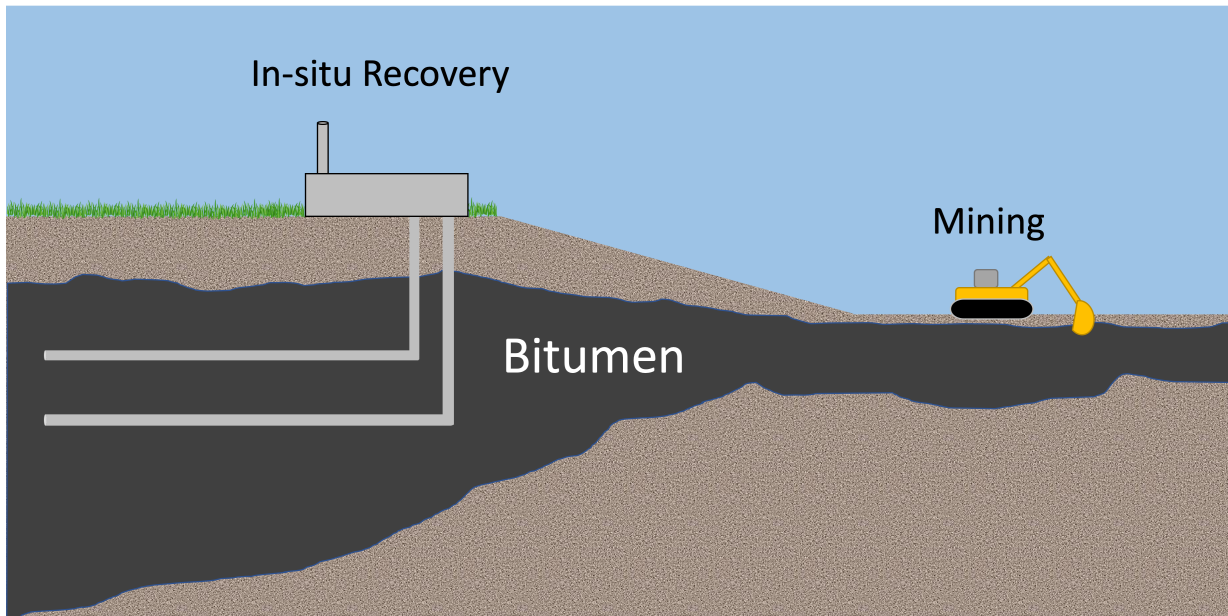
Figure 2.1: Canadian tar sand bitumen recovery.

Current in-situ methods of bitumen recovery are also dependent on large water requirements per barrel of oil extracted. The most utilized method of in-situ retrieval is steam assisted gravity drainage(SAGD). It requires boiling large quantities of freshwater for steam which is then pumped into the well in order to melt the viscous bitumen. This water is returned to the surface laden with bitumen, sand, acids, heavy metals, and other toxins that must be removed before the water is returned to the environment. The energy requirements of boiling the fresh water used in the SAGD method of bitumen extraction is its own environmental cost. It is estimated that the Canadian tar sands accounts for 10% of the carbon output for the entire country (See Fig. 2.3, Source: Environment and Climate Change Canada 2018). The idea of burning hydrocarbons to produce hydrocarbons is inherently inefficient.

2.1.4 The case for VAPEX

Good management can be defined by the searching for and improving upon inefficiencies. This definition needs application to the management of Canada's natural resources. The majority of the Canadian tar sands are too deep for mining to be an effective method of recovery [17], therefore in-situ methods will be increasingly important in moving forward

Figure 2.2: Alberta mining operation and truck with human for scale. Source: The Economist: Science and Technology September 2014.

with economic development. Refining the inefficiencies of in-situ methods is paramount, especially the environmental inefficiencies of energy and water usage.

By introducing a solvent into a bitumen well rather than steam in order to reduce viscosity, it can be argued that the environmental impact is reduced. There is no heat energy requirements for the solvent, the carbon footprint of production wells is reduced. The solvent is miscible with the bitumen, and so the majority of it is recovered when the bitumen/solvent mixture is pumped out allowing for recycling of the solvent. Without complicated heat exchangers to reprocess the water-oil mixture produced in SAGD, there is less capital infrastructure required in solvent based recovery methods. The solvent also upgrades the oil in-situ, via the phenomenon of asphaltene precipitation [21] that ends up leaving some of the unwanted by-products of bitumen in place removing the requirement to process and return such by-products to the environment. Tailing ponds are non-existent as the entirety of the produced oil is shipped for refinement. The case for using a VAPEX method is of particular interest environmentally.

2.2   Current methods of in-situ bitumen recovery

As the focus of this project is the modelling of in-situ method of bitumen recovery, a brief introduction to the types of current methods utilized is provided here.
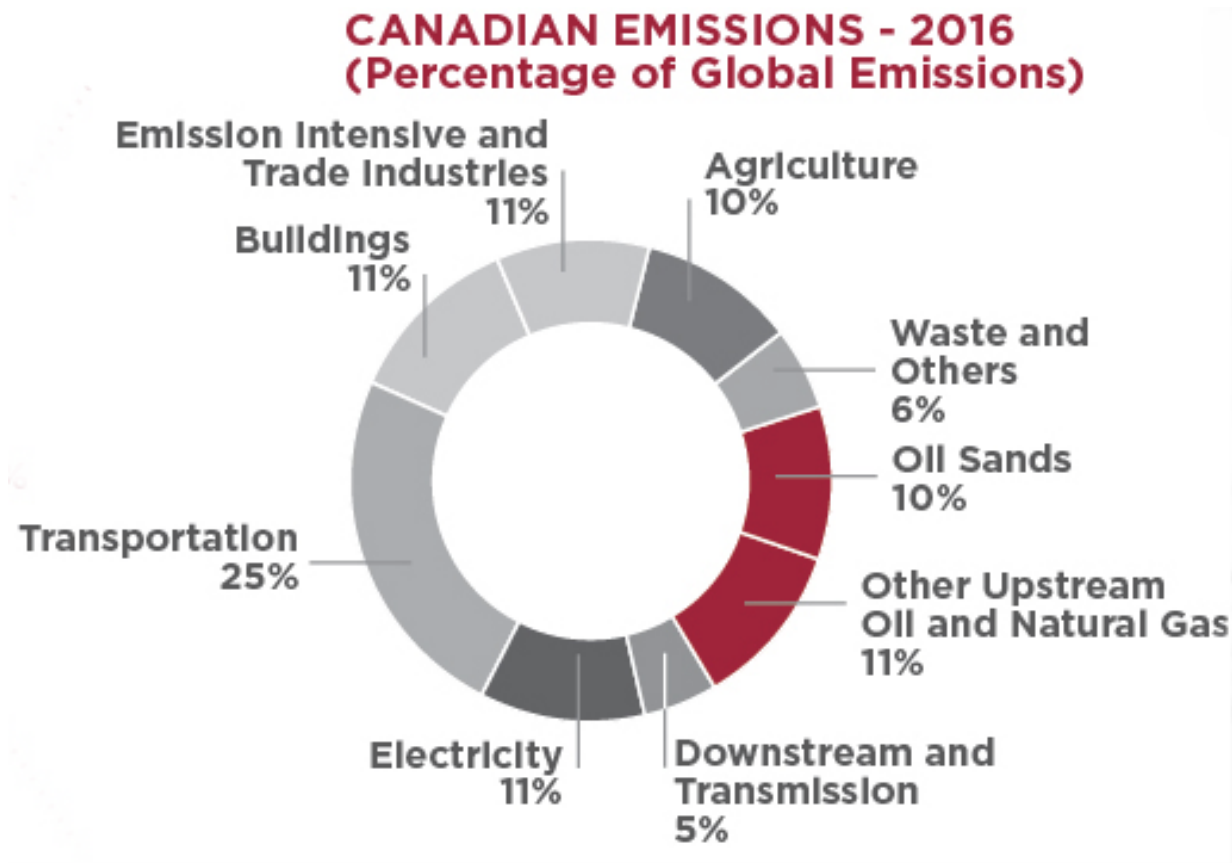
Figure 2.3: Carbon emissions for Canada by industry. Source: Environment and Climate Change Canada 2018

Cyclic steam stimulation: CSS

Cyclic steam stimulation is the original steam assisted gravity drainage method. It was discovered by accident in Venezuela in 1959 [16] when a steam injector produced oil instead of the intended steam flooding of a nearby well. The idea then developed into an injection of steam into a vertical well, soaking the buried bitumen with heat energy. Steam injection is then halted, and the heat is allowed to dissipate (soak) inside of the well for a period of time ranging from a number of days to weeks. Geological formation plays an important role in determining if CSS will be a profitable. Deep wells with pay zones of 80 feet or more are preferred for the vertical well, where duration of steam heat soaking will allow for maximum horizontal viscosity reduction [22]. After this soaking and dissipation the

bitumen is less viscous and able to be pumped out. This process is repeated in a cycle, until such a time as production in the well drops below profitability. See Fig. 2.4 for a visual accompaniment of CSS in action.
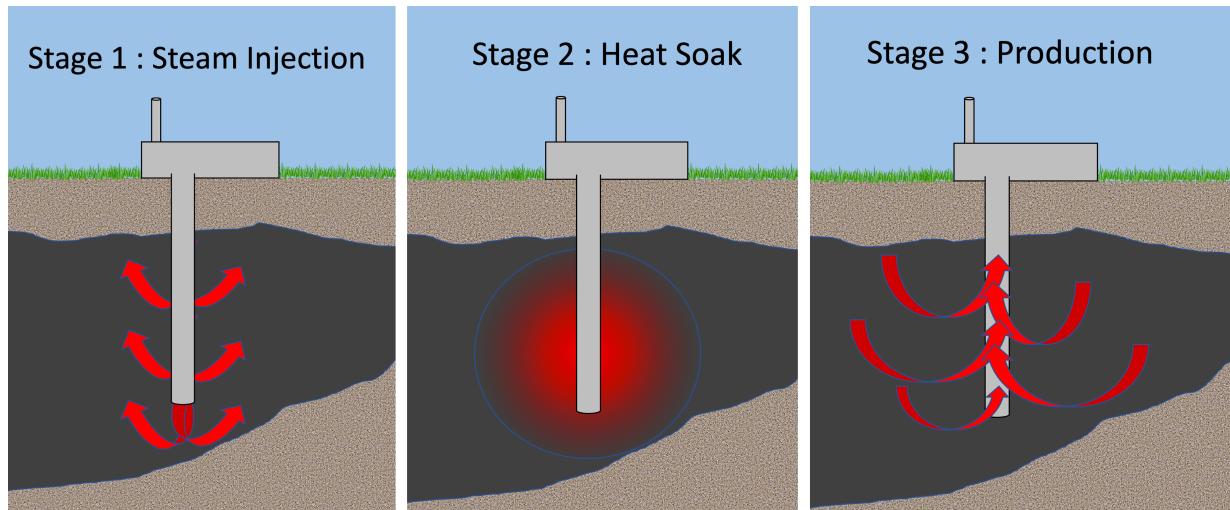
Figure 2.4: Cyclic Steam Stimulation

The Canadian oil sands have made use of CSS since the mid 1980's. The steam/soak/produce cycle occurs over weeks to months making the production rates for CSS predictable, but lacking in continuity. The use of steam as a heat delivery method lead directly to the development of another steam based system utilizing horizontal well drilling.

Steam assisted gravity drainage: SAGD

Steam assisted gravity drainage is the current preferred method for deep bitumen extraction. Much like CSS, SAGD uses hot steam in order to reduce the viscosity of the bitumen. Two horizontal pipes are drilled one above the other, the top being a steam injector while the bottom is an oil producer. The hot steam warms the bitumen, and the reduced viscosity fluid drains through to the bottom producer pipe. See Fig. 2.5 and Fig. 2.6 for visual accompaniment of the process.

Commercial use of SAGD in the Canadian tar sands has been active since the late 1990's. This method is continuous, as opposed to the CSS method, allowing for production to be consistent and predictable. A vertically thin pay zone can still be a profitable SAGD well as the horizontal nature of the process allows for insertion into those types of deposits.
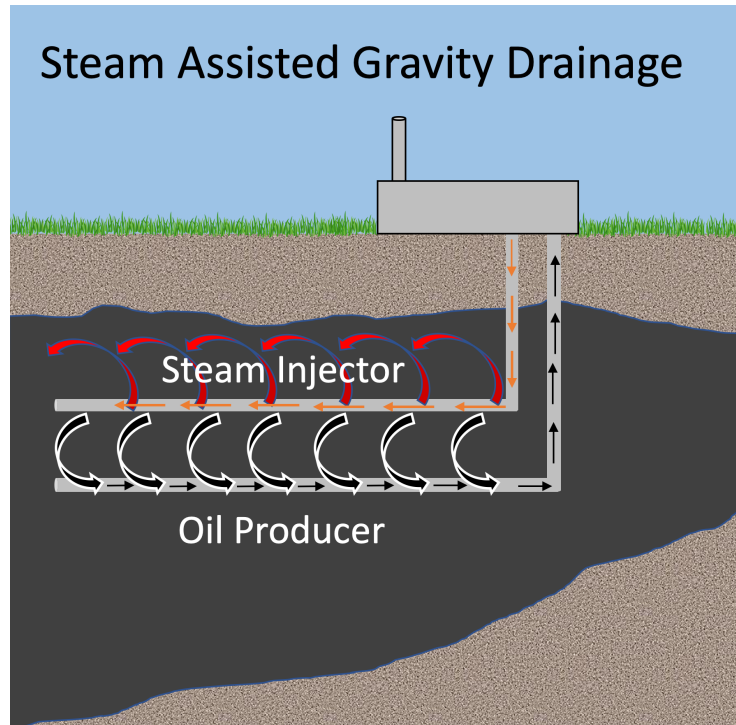
Figure 2.5: Steam Assisted Gravity Drainage

Energy economics of burning natural gas to produce steam makes the appeal of SAGD environmentally incommodious.

Vapour Extraction: VAPEX

In 1989 two researchers named Butler and Mokrys from the University of Calgary published a paper in AOSTRA Journal of Research [10] that investigated an idea to use a solvent to reduce the viscosity of bitumen in-situ both experimentally and mathematically. Using a solvent for in-situ production of bitumen was not unique, but the use of only a solvent as opposed to a solvent-steam combination had yet to be experimented with in the laboratory or in the field. The experiment set-up used toluene as a liquid solvent to reduce the viscosity of bitumen trapped in a Hele-Shaw cell. This experimental set-up uses two plates with the liquid bitumen sandwiched between. The experiment successfully showed that the idea of a solvent-analogue to SAGD worked in principle, and they set out to show that the production rates could be modelled.
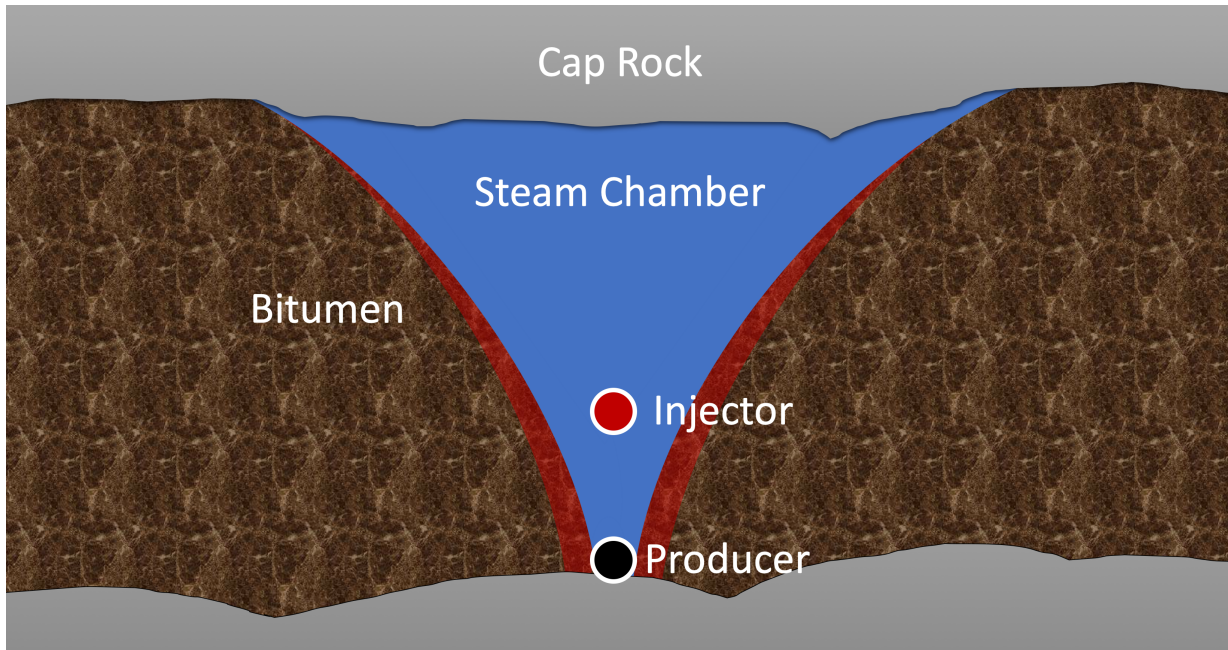
Figure 2.6: SAGD chamber

VAPEX is an analogue to SAGD in that it utilizes two horizontal wells, one a producer and one an injector. The similarities extend to the chamber within the well, in that Fig. 2.6 could be identically replicated with "Steam Chamber" replaced with "Vapour Chamber". Instead of steam as the viscosity reducing agent, a solvent such as butane or propane is used. The reduction of viscosity and subsequent outflow of producible oil to the producing well creates a vapour chamber. This chamber still contains the residual saturation (irremovable bitumen), but is vacated of the majority of bitumen, hence the name vapour chamber.

The vapour chamber has an advancing transition zone where the amount of mass fraction of solvent in the bitumen changes from zero to a value that corresponds to solubility of solvent in bitumen under the prevailing conditions. For butane in bitumen at standard conditions the solubility mass fraction is about 0.45 [23]. The mass fraction of solvent in bitumen reaches a critical value at which liquid viscosity is low enough to become mobile. This happens via mass transfer from the gaseous phase, molecular diffusion, and hydrodynamic dispersion. Gravity is the driving force for the now mobile producible oil which flows towards the lower producer pipe. The bitumen velocity in the transition zone is variable, depending on the mass fraction of the solvent. The body forces keep the mobile bitumen solvent mixture moving, exposing bitumen that has yet to mix with solvent, continuing

13

the advancement. Butler and Mokrys theorized that the miscibility of a liquid solvent and bitumen, and the resulting increased mobility should lead to the development of a chamber similar to the one formed during SAGD or CSS production. This is a "S shape" profile which can be seen in the centre pane of Fig. 2.7 b.
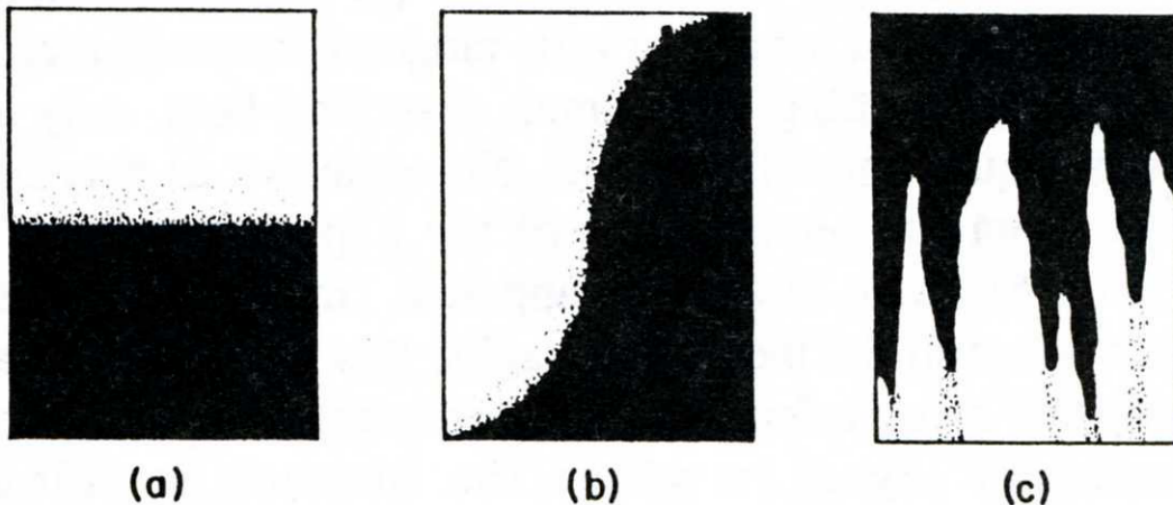
Figure 2.7: VAPEX profiles theorized by Butler and Mokrys [3].

Stages of solvent chamber growth were originally explored in [10] as seen in Fig. 2.7. Butler and Mokrys also investigated the effect of permeability on the solvent chamber as seen in Fig. 2.8. These two original experiments have the baseline for all future simulation work qualitatively. Both simulations show height of capillary rise (the height at which the capillary pressure balances the body force and the wetting phase will not drain from the porous media).

VAPEX has been experimented with in laboratory settings [24, 25, 26, 27, 28, 4, 29, 1, 30, 31, 3, 32] and has been attempted in a live oil field test [33]. Experiments have shown the validity of the method in producing bitumen in-situ. While testing has occurred, profitability has yet to be achieved with VAPEX in a commercial setting. By better understanding the physical phenomena occurring in the transition zones of a VAPEX system, and being able to predict behaviour using a well formulated mathematical model, there is hope that the inefficiencies in the method can be corrected and a more environmentally friendly in-situ bitumen production method emerges.

14

k = 484 Darcy
b = 3 thou

k = 1935 Darcy
b = 6 thou

k = 17420 Darcy
b = 18 thou
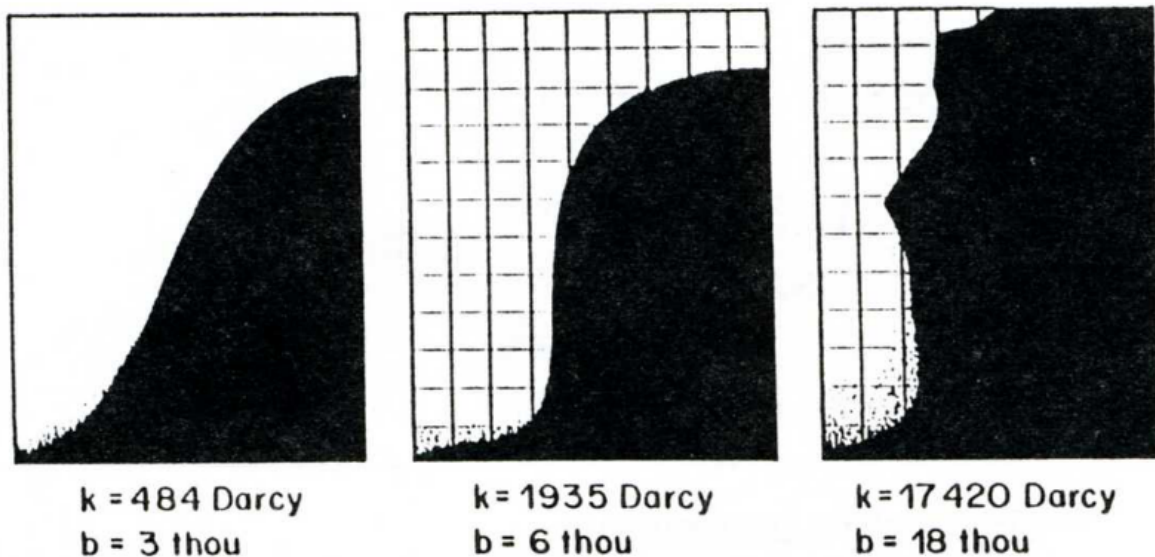
Figure 2.8: VAPEX profiles of various permeabilities [3].

2.3 Porous media physics

Consider two immiscible fluids present within a porous media. One is preferentially attracted to the solid and called the wetting phase, while the other is called the non-wetting phase. In a gas-liquid system the gas is always the non-wetting phase provided the solid is hydrophilic. The two fluids will be separated by a well-defined interface, which can be considered infinitesimally thin. Cohesion between liquid molecules at one side of the interface is different from gas molecules on the other side, making the interface characterizable by some surface tension, which is a measure of the forces that must be overcome to change the interface shape. The existence of surface tension results in a difference between the equilibrium pressures of the gas phase and fluid phase across a curved interface. The pressure difference between the gas and liquid phases can be calculated using the Young-Laplace equation:

$$p_c = p_{nw} - p_w = -\gamma \nabla \cdot \hat{n} = \gamma \left(\frac{1}{R_1} + \frac{1}{R_2} \right) \tag{2.1}$$

where p is pressure, p_c specifically is capillary pressure, $\hat{n}$ is the unit normal on the fluid-fluid interface, γ is the surface tension, and R_1 and R_2 are the principal radii of curvature.

A continuum approximation of porous media physics requires generalization of volume

15

fractions of the three phases present (solid, liquid, gas). All three phases can simultaneously occupy a control volume. Porosity represents the pore volume of the domain (volume not occupied by the solid porous media skeleton). Porosity and saturation define the fraction of bulk volume that is void and the fraction of void volume occupied by each phase.

$$\phi = \frac{V_{void}}{V_{total}} \tag{2.2}$$

$$S_i = \frac{V_i}{V_{void}} \tag{2.3}$$

where ϕ is the porosity, S is the saturation, and V is the domain volume. The sum of phase saturations is equal to unity.

$$S_g + S_l = 1 \tag{2.4}$$

The description of flow in porous media is facilitated by defining a so-called fluid potential relative to a reference location. A reference location is commonly assumed to be at the surface of a free liquid body located at the same elevation as the control volume of the porous media, and subjected to a reference pressure. If the fluid density is dependent on pressure and the only body force is gravity, acting in the direction of increasing elevation z, the potential of the fluid can be expressed in terms of hydraulic head:

$$H_i = \int_{p_{ref}}^{p_i} \frac{1}{\rho_i(\hat{p}g)} d\hat{p} + z = \psi_i + z \tag{2.5}$$

where ρ is the fluid density, z is the height above the reference, g is the magnitude of the gravitational body force, and ψ is the pressure head.

For unsaturated flow, the presence of fluid-fluid interfaces in a porous medium gives rise to a relationship between fluid saturation and capillary pressure at equilibrium. If the medium is fully liquid saturated, it can be usually be invaded by the gas phase only if the gas pressure exceeds the liquid pressure by a specific threshold value. After this value has been exceeded the pores begin to drain and overall saturation of the domain becomes less than one. The specific value of gas pressure for infiltration corresponds to the diameter of the largest pore forming a connection path through the domain. Above the value of the gas infiltration pressure, the water saturation decreases, the rate of which is determined by the uniformity of the pore size. If the pores size approaches homogeneity, drainage occurs quickly above the entry pressure, and the rate of change of the curve is steep. For porous media with significant variability in pore diameter, only a small part of the network drains

16

with each increment of the potential making the decrease in saturation much more gradual. The residual water saturation is reached when drainage rates are reduced to a level such that further liquid flow is no longer possible regardless of pressure increase.

Capillary pressure curves, demonstrated in Fig. 2.9 show hysteresis and dependency on the history of the saturation change. The portion of the curve labelled "P.D." represents primary drainage of the porous medium, while the "S.I" labelled curve is imbibition. Primary drainage and imbibition curves are complementary but not equivalent. It is, in general, not possible to reach full liquid saturation during imbibition, due to the trapping of gas bubbles.

At the pore scale, conservation of momentum for each fluid phase can be represented by the Navier-Stokes equations. Under the assumptions of steady, laminar flow of incompressible, Newtonian fluid in a horizontal tube having a uniform circular cross-section, the Navier-Stokes equations reduce to the Poiseuille equation, which can be used to find the average fluid velocity for flow in a circular pipe. This average fluid velocity has the feature that it is directly proportional to the pressure gradient. By generalizing into three dimensions and using a volume averaging process, a Navier-Stokes solution yields Darcy's law:

$$\boldsymbol{v} = -\frac{\boldsymbol{k}}{\mu}\left(\nabla p - \rho g z\right) \tag{2.6}$$

where $\boldsymbol{v}$ is the fluid velocity through the porous medium, k is the permeability tensor which depends on the geometric characteristics of the pores, μ is the viscosity of the fluid. Under the assumption of an incompressible fluid, the Darcy velocity is written as a function of the hydraulic head from Eqn. (2.5):

$$\boldsymbol{v} = -\frac{\boldsymbol{k}\rho g}{\mu}\nabla\left(\psi + z\right) \tag{2.7}$$

In a general case, if the porous medium is considered anisotropic, the permeability tensor is dependent on the absolute permeability of the porous medium and a function of saturation. The relationship is written in the following simplified form:

$$\boldsymbol{k} = \boldsymbol{k}_a k_r(S) \tag{2.8}$$

where $\boldsymbol{k}_a$ is the absolute permeability, and k_r is the relative permeability; a function of the saturation. The maximum value of $k_r = 1$ corresponds to a fully saturated fluid phase while the minimum value $k_r = 0$ occurs when the fluid phase saturation is reduced to the residual saturation and the fluid becomes effectively immobile.

2.3.1 Governing Equations for Two Phase Flow

The governing equations for two-phase flow in a porous medium are derived from conservation of mass, applied in a continuum approximation to a representative control volume where the pore-scale dynamics can be averaged. In the absence of source or sink terms, the change in the total mass of a fluid phase inside the domain must be balanced by the total mass flux across the boundary. For a rigid solid phase this is expressed as:

$$\frac{\partial}{\partial t} \int_V \rho_i S_i \phi dV = \int_{\partial V} \rho_i \boldsymbol{v}_i \hat{n} d\partial V \tag{2.9}$$

where V is the arbitrary control volume, ∂V is the control volumes surface, and $\hat{n}$ is the unit normal vector to ∂V. By applying the Gauss Divergence Theorem, the equation can be represented in differential form:

$$\phi \frac{\partial}{\partial t} (\rho_i S_i) + \nabla \cdot (\rho_i \boldsymbol{v}_i) = 0 \tag{2.10}$$

Using the Darcy velocity (Eqn. (2.7))of each fluid phase with respect to the solid phase, the system of two coupled partial differential equations describing two phase flow in porous media are:

$$\phi \frac{\partial}{\partial t} (\rho_l S_l) - \nabla \cdot \left(\rho_l \frac{k k_{rl} \rho_l g}{\mu} \nabla (\psi_l + z) \right) = 0 \tag{2.11}$$

$$\phi \frac{\partial}{\partial t} (\rho_g S_g) - \nabla \cdot \left(\rho_g \frac{k k_{rg} \rho_g g}{\mu} \nabla (\psi_g + z) \right) = 0 \tag{2.12}$$

The gas phase is compressible, while the liquid phase is considered incompressible. Density of the liquid phase will be factored out:

$$\phi \frac{\partial S_l}{\partial t} - \nabla \cdot \left(\frac{k k_{rl} \rho_l g}{\mu} \nabla (\psi_l + z) \right) = 0 \tag{2.13}$$

$$\phi \frac{\partial}{\partial t} (\rho_g S_g) - \nabla \cdot \left(\rho_g \frac{k k_{rg} \rho_g g}{\mu} \nabla (\psi_g + z) \right) = 0 \tag{2.14}$$

The two-phase model presented can be further simplified under specific conditions occurring for air and water flow in an unsaturated porous medium. At the temperature of

$20°C$ the air viscosity is about 55 times smaller than the water viscosity [34]. Air mobility is greater than the water mobility by approximately the same factor, if the relative permeabilities of both fluids are similar. Therefore, it can be expected that any pressure difference in the air phase will be equilibrated much faster than in the water phase [34]. Assuming the gas phase is continuous in the pore space and that it is connected one can consider the pore air to be essentially at a constant reference pressure. These assumptions allow to eliminate the equation for the air flow from the system of governing equations. Capillary pressure is now uniquely defined by the liquid pressure. For convenience it is often assumed that the reference atmospheric pressure $p_g = 0$:

$$p_c = p_g - p_l = -p_l \tag{2.15}$$

The formulation of two phase flow in unconsolidated porous media is named Richards Equation, after Lorenz A. Richards [35] presented it in Eqn. (2.16). This formulation is called the mixed formulation due to the change of saturation, S, with respect to time being solved on the left hand side while the matric pressure head, ψ, is the independent variable on the right hand side. This requires a coupling function for S and ψ.

$$\phi \frac{\partial S}{\partial t} = \nabla \cdot \left(\frac{k k_r \rho_l g}{\mu} \nabla (\psi + z) \right) \tag{2.16}$$

2.3.2 Governing Equations for Multicomponent Phases

The governing equations for multi-component mixtures in a porous medium are derived from conservation of mass. Additional terms of source or sink terms and hydrodynamic dispersion, are required to describe the change in species mass within the domain. For a rigid solid phase this is expressed as [13]:

$$\frac{\partial W_i}{\partial t} + \nabla \cdot N_i = R_i \tag{2.17}$$

$$W_i = \sum_j \phi S_j \omega_{ij} \rho_j \tag{2.18}$$

$$N_i = \sum_j \left(\rho_j \omega_{ij} \boldsymbol{v_j} - \phi \rho_j S_j \boldsymbol{D}_{ij} \nabla \omega_{ij} \right) \tag{2.19}$$

where W is species mass per unit volume of continuum, N is the species flux, ω is the species mass fraction, and $\boldsymbol{D}$ is the hydrodynamic dispersion tensor.

19

When fluid flows through a pore network of a porous medium, there can be numerous passages formed from interconnected pore throats. Due to the complexity of the geometry of porous media, an approximation of the mechanical mixing aided by flow on the micro-scale are averaged. Mass transport in a porous medium is carried out in the moving fluid and the phenomenon of hydrodynamic dispersion encompasses the mechanical and molecular mixing of species.

Sources and sinks of a species represents spontaneous introduction of mass into a domain, which can account for interphase mass transfer.

In a binary liquid mixture such as solvent and bitumen, as will be studied in a VAPEX domain, each species must be conserved:

$$\phi\frac{\partial}{\partial t}\left(\rho_l S_l \omega_s\right) + \nabla \cdot \left(\rho_l \omega_s \boldsymbol{v}_l - \phi S_l \rho_l \boldsymbol{D_{sb}} \nabla \omega_s\right) = R_s \tag{2.20}$$

$$\phi\frac{\partial}{\partial t}\left(\rho_l S_l \omega_b\right) + \nabla \cdot \left(\rho_l \omega_b \boldsymbol{v}_l - \phi S_l \rho_l \boldsymbol{D_{bs}} \nabla \omega_b\right) = R_b \tag{2.21}$$

where the subscripts s and b denote solvent and bitumen respectively and the subscript l describes the entire liquid phase. In a VAPEX domain there would be no source of bitumen and the R_b term would be zero. The summation of both components would represent the conservation of mass of the entire liquid phase, forcing an addition of mass source to the right hand side of Eqn. (2.13) and Eqn. (2.14). If the mass source and sink are interphase mass transfer such as occurs in a VAPEX domain, and butane vapour mass is transferred into the liquid phase, then they are equal and opposite source and sink terms respectively:

$$\phi\frac{\partial}{\partial t}\left(\rho_l S_l\right) + \nabla \cdot \left(\rho_l \boldsymbol{v}_l\right) = R_s \tag{2.22}$$

$$\phi\frac{\partial}{\partial t}\left(\rho_g S_g\right) + \nabla \cdot \left(\rho_g \boldsymbol{v}_g\right) = -R_s \tag{2.23}$$

2.4 Mathematical Models of VAPEX

VAPEX, both experimentally and mathematically, was originally conceived as an analogue to steam assisted gravity drainage where the steam has been replaced by composition as the viscosity reducing agent. The first mathematical model due to Butler and Mokrys [3]reflects this. The model was conceived from an experiment in a Hele-Shaw cell that had liquid toluene as opposed to a vapour hydrocarbon solvent. This removed the dependency

20

of capillarity on drainage in the model. The model focuses on the transition zone between pure bitumen and pure solvent as seen in Fig. 2.10.

By assuming that the tangential velocity U of the transition zone occurs at the exact rate in order to balance the flux of a moving control volume, the model assumes a steady state divergence of flux to be zero (Eqn. (2.24)).

$$-D_s \frac{dc_s}{d\xi} = Uc_s \tag{2.24}$$

By balancing the forces (gravity, viscous drag against the cell walls) the flow rate of bitumen was approximated as Eqn. (2.25).

$$Q = \sqrt{2kg\phi\Delta S_o h N_s} \tag{2.25}$$

$$N_s = \int_{c_{min}}^{1} \frac{D_s (1 - c) \Delta\rho}{\mu} \frac{dc}{c} \tag{2.26}$$

This equation was able to predict the flow rate of bitumen from the Hele-Shaw experiment, but fails to capture the porous media physics necessary to describe flow rates in an unconsolidated VAPEX experiment. The model also fails to account for the temporal development of the solvent chamber which by the experiment it was based upon showed changing orientation of the transition zone. Subsequent modelling work has relied almost exclusively on the original development of Butler and Mokrys. Such work has introduced assumptions regarding the evolution of the vapour chamber into the flow rate calculations. For example, assuming that a solvent chamber is at all times a circle of increasing radius and changing centre location, and then assuming that diluted bitumen flows down the outer radius of such a circular chamber, the model suggested by [30] was developed.

$$t_r = \Delta t_r \frac{R_o}{\delta_r} \left[\left(\frac{H}{2R_o} \right)^2 - 1 \right] + t_o \tag{2.27}$$

$$Q(t) = \Delta S_o \phi d\pi R_o^2 \left[\frac{(t - t_o)\delta_r}{\Delta t_r R_o} + 1 \right] \tag{2.28}$$

Equation (2.28) provides a predicted flow rate during the rising phase of the vapour chamber under the assumptions made. However the shape the vapour chamber will take

once again ignores the porous media and fluid mixing physics occurring at the transition zone. Further assumptions about the direction and path of flow within a porous media is non-physical especially during the rising phase depicted in [36].

Research conducted at the University of Waterloo by Tam [1] attempted to include the transient and porous media physics in a VAPEX mathematical model. The model was presented as Eqn. (2.29) and Eqn. (2.30).

$$\phi \frac{\partial S_o}{\partial t} + \nabla \cdot \boldsymbol{v} = 0 \tag{2.29}$$

$$\phi \frac{\partial S_o \omega_s}{\partial_t} + \nabla \cdot (\omega_s \boldsymbol{v} - \phi S_o D \nabla \omega_s) = \frac{R_s}{\rho_o} \tag{2.30}$$

Equation (2.29) conserves the mass of liquid phase, and Eqn. (2.30) conserves the mass of the solvent. The model accounts for interphase mass transfer in the J_s term, but fails to account for the addition of mass in the liquid phase. The research attempted to solve the problem using the COMSOL package. The model failed to converge as presented and was not fully validated against experiments. Although capillary pressure and hydrodynamic dispersion were considered, the processes were roughly approximated. Notwithstanding these limitations, Tam's model is the starting point for this research.
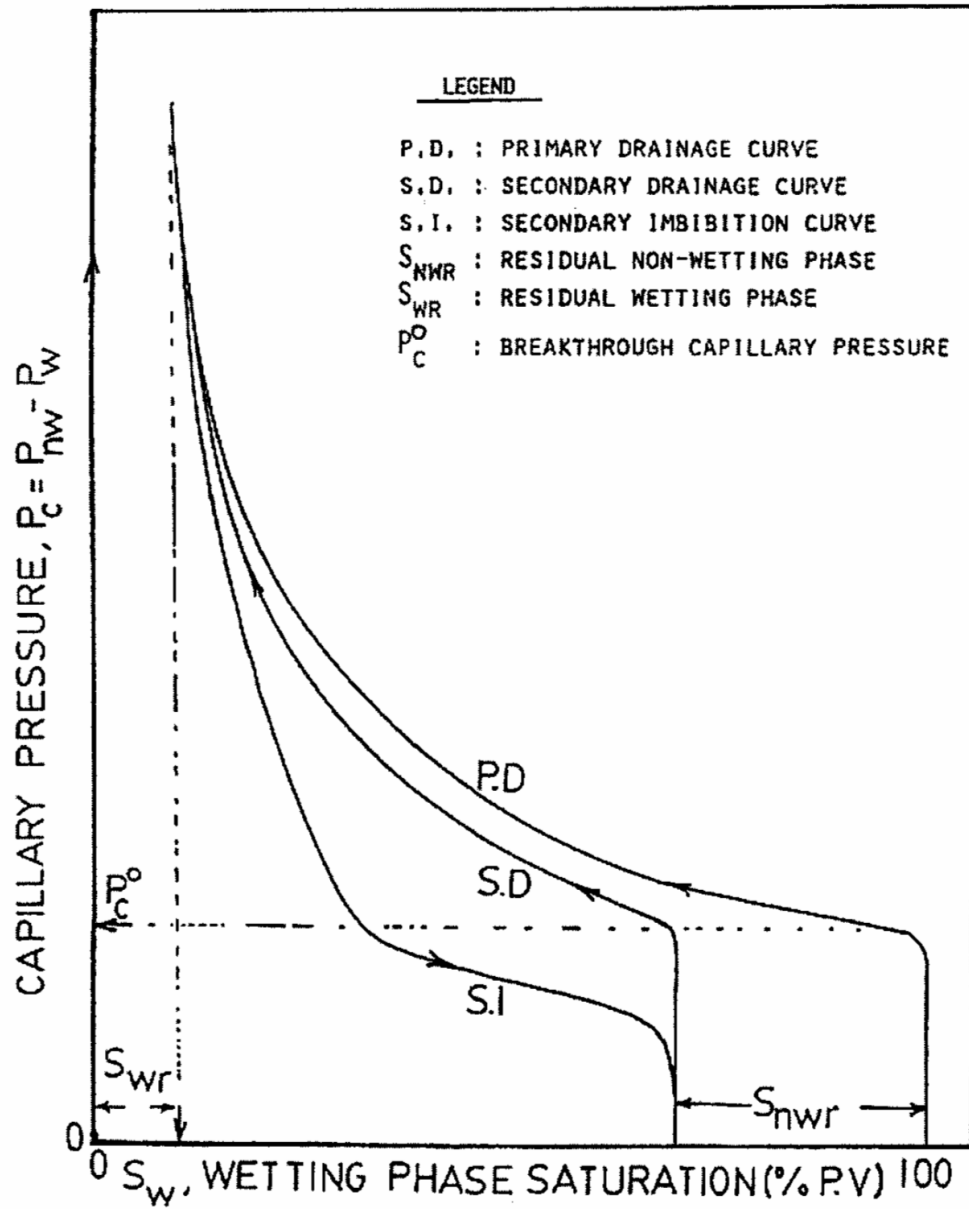
Figure 2.9: Capillary pressure curve show hysteresis of drainage compared to imbibition. Source: Chatzis class notes, CHE 514, University of Waterloo.

23
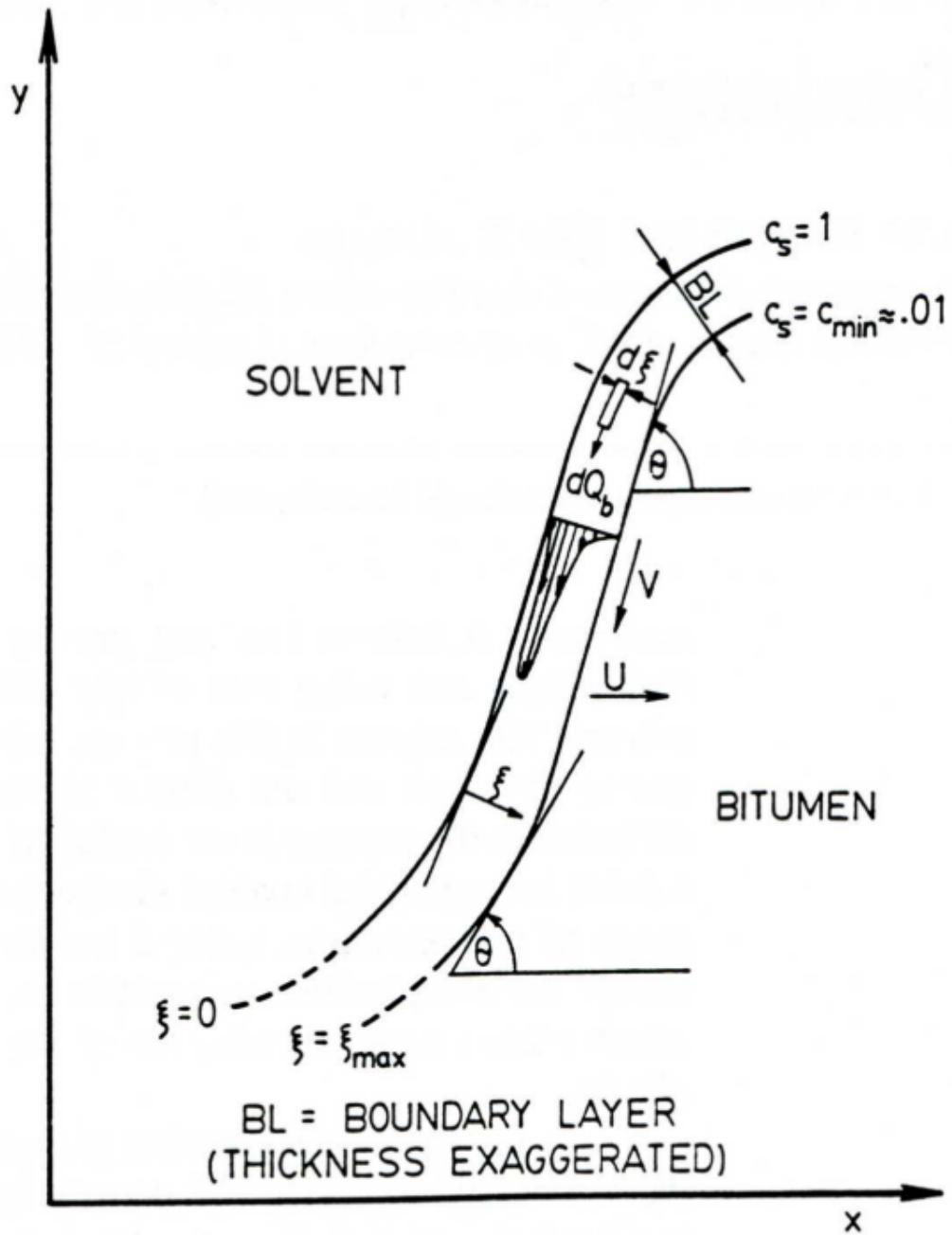
Figure 2.10: Solvent bitumen transition zone as imagined in [3]

Chapter 3

A predictive model of VAPEX

The point of this thesis is to explore a physics first model of VAPEX that captures the physical phenomena and to predict experimental results. The model is developed from first principals and includes physical property closures from empirical correlations including viscosity, capillary pressure, relative permeability, heterogeneous permeability, interfacial tension, saturation, dispersion, diffusion, advection, and inter-phase mass transfer.

3.1 Assumptions

The following assumptions are made:

- The solid phase is rigid, non-reacting, unconsolidated porous media

- The system is isothermal

- The liquid phase is incompressible

- The solvent for this model will be butane

- The liquid phase is a binary mixture of bitumen and butane

- The gas phase is single component butane

- The gas phase reference pressure is 0 psi

- The gas is assumed to be pure butane and to be an infinitely mobile fluid (Richards assumption)

- Domain will be a two-dimensional Cartesian co-ordinate system (x, z) where z is the unit vector in the opposite direction of the force of gravity, measured up from a reference height where $z = 0$

These assumptions are made to either ease the computational complexity of the problem, or due to an experimental observance that makes sense to incorporate into the model. In the tar sands, unconsolidated porous media is not rigid as sand can be produced with bitumen. As solid particulate in bitumen production was not discussed in VAPEX experiment literature, it will be assumed to be negligible in this study. The assumption that the gas phase is single component may not be true due to volatility in the bitumen. It is possible that gaseous components of the bitumen are miscible in the butane gas phase resulting in a gaseous mixture. This possibility was mitigated in the experiments in [1] by exposing the bitumen to low pressures prior to the VAPEX experiment to clear the possibility of volatile components. The gas phase is considered infinitely mobile, an assumption that works in experiment scale models but would have to be re-evaluated in a field-scale model of VAPEX as distances measured in metres as opposed to millimetres would affect gas fluid dynamics. The assumption that only bitumen and butane exist in the liquid phase works in experimentation, but in a field model of the VAPEX system connate water would have to be included. Connate water was explored in experiment 2 and 4 in [1], but are not included in the derivation of this model. The choice to model the bitumen-butane VAPEX system, as opposed to a bitumen-propane or any other vapour solvent, was made due to the abundance of empirical models from butane VAPEX experiments.

3.2 Model Formulation

Conserving the mass of the gas phase, liquid phase, and each of the components of the liquid phase generates the following four general conservation of mass equations equations:

$$\phi \frac{\partial}{\partial t} (\rho_l S_l) + \nabla \cdot (\rho_l \boldsymbol{v}_l) = R_l \tag{3.1}$$

$$\phi \frac{\partial}{\partial t} (\rho_g S_g) + \nabla \cdot (\rho_g \boldsymbol{v}_g) = R_g \tag{3.2}$$

$$\phi \frac{\partial}{\partial t} (\rho_l S_l \omega_s) + \nabla \cdot (\rho_l \omega_s \boldsymbol{v}_l - \phi S_l \rho_l \boldsymbol{D} \nabla \omega_s) = R_s \tag{3.3}$$

$$\phi \frac{\partial}{\partial t} (\rho_l S_l \omega_b) + \nabla \cdot (\rho_l \omega_b \boldsymbol{v}_l - \phi S_l \rho_l \boldsymbol{D} \nabla \omega_b) = R_b \tag{3.4}$$

where the s subscript denotes solvent (butane in this model), b denotes bitumen, R are source terms. Applying the assumption of gas phase dynamics being fast, Eqn. (3.2) is considered solved provided a solution for S_l can be found. The assumption of interphase mass transfer being introduced as the butane component of the liquid phase only, implies $R_b = 0$. Since the liquid phase is a binary mixture, the solution to one mass fraction ω is enough to discover the other mass fraction so only one of Eqn. (3.3) or Eqn. (3.4) is required (solving for ω_s is preferred in this study). The resulting applications of assumptions simplifies the model to the following coupled partial differential equations:

$$\phi \frac{\partial}{\partial t} (S_l) + \nabla \cdot (\boldsymbol{v}_l) = J_s \tag{3.5}$$

$$\phi \frac{\partial}{\partial t} (S_l \omega_s) + \nabla \cdot (\omega_s \boldsymbol{v}_l - \phi S_l \boldsymbol{D} \nabla \omega_s) = J_s \tag{3.6}$$

$$\tag{3.7}$$

where the fluid velocities are the Darcy velocity for the domain, and J_s is the source term divided by the constant liquid density:

$$\boldsymbol{v}_l = -\frac{k k_r \rho_l g}{\mu} \nabla (\psi + z) \tag{3.8}$$

$$J_s = \frac{R_s}{\rho_l} \tag{3.9}$$

The model is defined with two solution domains: ψ and ω_s. Saturation of the liquid phase is a function of ψ, as are relative permeabilities k_r and hydrodynamic dispersion $\boldsymbol{D}$.

Viscosity is dependent on mixture composition, as are interfacial tension and hydrodynamic dispersion. Saturation is dependent on the interfacial tension also, making it dependent on mixture composition. The source term J_s will be shown to depend on composition and saturation of the domain. Re-writing the equations to display these dependencies results in the following:

$$\phi\frac{\partial}{\partial t}\left(S_l(\psi,\omega_s)\right) + \nabla\cdot\left(-\frac{kk_r(\psi,\omega_s)\rho_l g}{\mu(\omega_s)}\nabla(\psi+z)\right) = J_s(\psi,\omega_s) \tag{3.10}$$

$$\phi\frac{\partial}{\partial t}\left(S_l(\psi,\omega_s)\omega_s\right) + \nabla\cdot\left(\omega_s\left(-\frac{kk_r(\psi,\omega_s)\rho_l g}{\mu(\omega_s)}\nabla(\psi+z)\right) - \phi S_l(\psi,\omega_s)\boldsymbol{D}(\psi,\omega_s)\nabla\omega_s\right) = J_s(\psi,\omega_s) \tag{3.11}$$

3.3   Empirical Correlations

The model defined in Eqn. (3.10) and Eqn. (3.11) is generalized and required empirical correlations to provide closures are introduced so the model may be solved numerically.

3.3.1   Saturation

The solution domains of matric pressure head ψ and mass fraction component ω_s are linked to saturation by means of the Van Genuchten correlation. This correlation was chosen due to the height of capillary rise being expressed, as opposed to Brooks-Corey where the height of capillary rise is implied at the bottom of the solution domain. Having the height of capillary rise expressed allows for a more realistic capillary pressure curve. The Van Genuchten correlation is defined as follows:

$$S_{eff} = \frac{S - S_r}{S_{sat} - S_r} \tag{3.12}$$

$$S_{eff} = \left(\frac{1}{1 + (\alpha\psi)^n}\right)^{1-\frac{1}{n}} \tag{3.13}$$

$$\Rightarrow S = \frac{S_{sat} - S_r}{\left(1 + (\alpha\psi)^n\right)^{1-\frac{1}{n}}} + S_r \tag{3.14}$$

where S_{eff} is the normalized saturation of a fully saturated domain, S_{Sat}, and the residual saturation, S_r. A fitting parameter n is discovered by matching the capillary pressure curve

to a known curve, in this case from [2], and α is a scaling parameter that is used to change the capillary pressure curve based upon interfacial tension and permeability relative to a known capillary pressure curve.

A non-linear fitting algorithm was used to generate a closely matching curve that includes the height of capillary rise shown in Fig. 3.1. The shape parameter n is constant for this study as the capillary pressure curve shape for producible oil qualitatively resembles water as shown in [37], and the scaling parameter will be a function of mass fraction which scales with the permeability of the system as well as the interfacial tension.
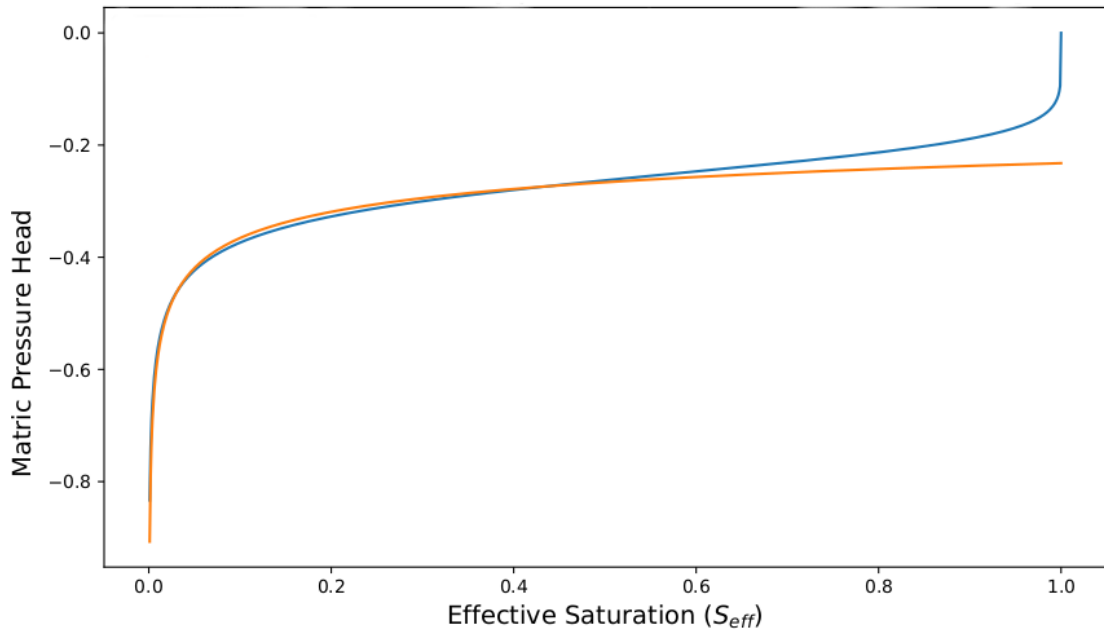
Figure 3.1: Van-Genuchten parameter selection found by curve fitting to Brook-Corey curve in [2]

3.3.2 Relative Permeability

The Van Genuchten correlation [38] provides the equation for relative permeability, establishing the relationship between the matric pressure head and the live oil's resistance to flow. This implies that the relative permeability is a function of both ψ and ω_s and introduces significant non-linearity into the model. The Van Genuchten relative permeability equation is defined as:

29

$$k_r = S_{eff}^{\frac{1}{2}} \left(1 - \left(1 - S_{eff}^{\frac{1}{1-\frac{1}{n}}} \right)^{1-\frac{1}{n}} \right)^2 \tag{3.15}$$

3.3.3 Interfacial Tension

The interfacial tension of a bitumen-butane mixture is dependent on the mass fraction of butane as shown in [39]. The experimental results were digitized and curve fitted (figure 3.2) into a usable function (3.16)

$$\gamma_o = 6.39e^{-13.32\omega_s} + 4.20e^{-10.84\omega_s} + 12.15e^{-2.51\omega_s} + 11.52 \tag{3.16}$$

The change in interfacial tension is directly proportional to the change in capillary pressure, making it inversely proportional to the Van Genuchten scaling parameter α.

3.3.4 Capillary pressure curve scaling (scaled water)

Making the reasonable assumption that Leverett J function scaling applies to the drainage capillary pressure data (p_c vs S_l) of mono-size packing's, then one can compute the changes in capillary pressure due to the interfacial tension of a bitumen-butane mixture, permeability, and porosity of a domain. Leverett's scaling equation is :

$$\frac{P_{c,1}}{P_{c,2}} = \frac{\gamma_1}{\gamma_2}\sqrt{\frac{k_2}{k_1}} \tag{3.17}$$

By finding reliable known capillary pressure data and scaling against it, the change in interfacial tension and permeability can be factored into the capillary pressure in the VAPEX model. The capillary pressure data this study is scaled against is found in [2], and represents the capillary pressure curve of water flowing in a packed bed of glass beads forming a domain of known permeability.

$$\frac{\alpha_2}{\alpha_1} = \frac{\gamma_1}{\gamma_2}\sqrt{\frac{k_2}{k_1}} \tag{3.18}$$

30
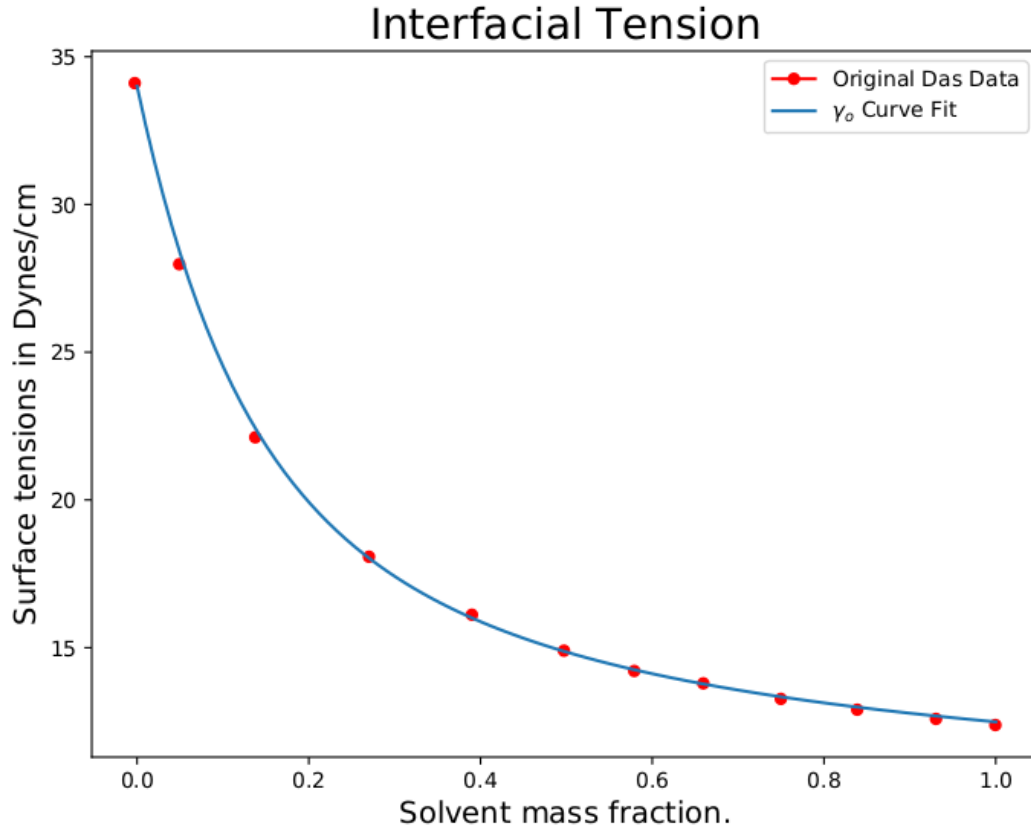
Figure 3.2: Interfacial tension curve fitting

Scalling using the Leverett J function allows for changes in capillary pressure due to interfacial tension change and permeability gradients. This introduces the idea that the model may be able to handle heterogeneity in the permeability field, which will be explored.

3.3.5 Viscosity

The goal of VAPEX is to remove bitumen from a domain. This is achieved by viscosity reduction. Introducing butane to the bitumen, the two miscible components interact to form a less viscous fluid, allowing bitumen to flow in production time scales. Viscosity is, therefore, the most important component of modelling the VAPEX system. Shu [40]

31

created a correlation that predicts the viscosity of the combination of two miscible components as a function of densities, viscosity's, and volume fractions of each component with the application of bitumen and butane mixtures.

$$\epsilon = \frac{17.04 \left(\rho_b - \rho_s \right)^{0.5237} \rho_b^{3.2745} \rho_s^{1.6316}}{\ln \left(\frac{\mu_b}{\mu_s} \right)} \tag{3.19}$$

$$f_b = \frac{\epsilon V_b}{\epsilon V_s + V_s} \tag{3.20}$$

$$f_s + f_b = 1 \tag{3.21}$$

$$\mu_{mix} = \mu_s^{f_s} \mu_b^{f_b} \tag{3.22}$$
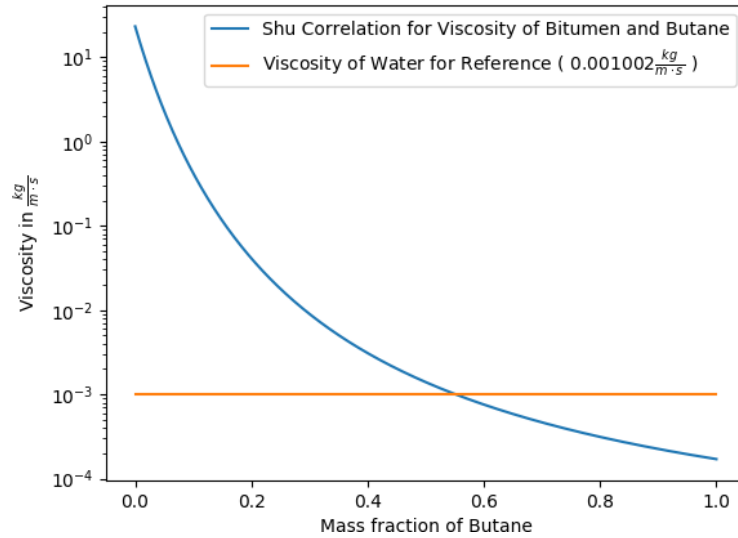
Figure 3.3: Shu's correlation for viscosity reduction of bitumen butane mixtures as a function of butane mass fraction.

3.3.6 Diffusion and Hydrodynamic Dispersion

Diffusion

Molecular diffusion in concentrated liquid mixtures is in general concentration-dependent. This was shown for bitumen and butane in [4]. The experimental approach captured

32

the rate of solvent mass transfer into the bitumen by measurement of bitumen swelling and butane uptake independently. The pressure was held constant so as to not violate equilibrium of solvent concentration at the interfacial boundary. The result was a linear dependence of a diffusion coefficient on the mass fraction of butane in the swelling bitumen-butane mixture:

$$D_m = 4.78x10^{-10}\omega_s + 4.91x10^{-10} \quad m^2/s \tag{3.23}$$
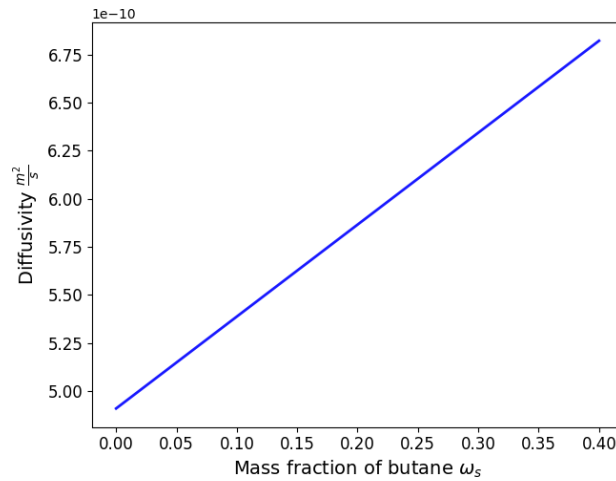
Figure 3.4: Diffusion as a function of mass fraction of butane [4]

Mechanical Dispersion

Mechanical dispersion is the mixing that occurs within the pores as fluid flows in, around, through voids in the porous medium. This idea that molecular diffusion is not the sole contributor on the mass transfer is important in this study. In order to properly account for dispersion it is important to realize that the fluid can flow in any direction due to capillary pressure, but the body force of gravity has a definite influence in a single direction that allows for the mixing to be defined for all directions by a dispersion tensor. A unique approach in [41] developed a two dimensional approximate experiment on a horizontal table top with a pore network. The experimental setup was designed to show the effects of mechanical dispersion on a dye tracer in flow in an unconsolidated porous medium, mimicking ground water flow. By removing the gravitational aspect upon the two dimensional

pore network the dispersion was modelled as a tensor quantity in the x y axes as:

$$D_{xx} = \frac{\delta_{long}u_x^2 + \delta_{tran}u_z^2}{\sqrt{u_x^2 + u_z^2}} \tag{3.24}$$

$$D_{xz} = \frac{(\delta_{tran} - \delta_{long})\, u_x u_z}{\sqrt{u_x^2 + u_z^2}} \tag{3.25}$$

$$D_{zx} = \frac{(\delta_{tran} - \delta_{long})\, u_x u_z}{\sqrt{u_x^2 + u_z^2}} \tag{3.26}$$

$$D_{zz} = \frac{\delta_{long}u_x^2 + \delta_{tran}u_z^2}{\sqrt{u_x^2 + u_z^2}} \tag{3.27}$$

where the values δ_{long} and δ_{tran} are dispersivity coefficients relating to the amount with which hydrodynamic dispersion occurs in the longitudinal and transverse directions. The correlations for the dispersivity coefficients are discussed in [5] and are related to the mean grain size of the porous medium. The choice of δ_{long} can be found using the table from in Fig. 3.5, and δ_{tran} is simply $\delta_{long}/10$ as discussed in [5]. The paper compiled results from approximately 4000 tests into dispersion coefficients both in the lab and in the field in order to find a correlation between dispersivity coefficients and the average grain diameter of the porous medium being investigated.

Grain size (mm)	d_{50} (mm)	U	n	Measuring values, see Fig.	A	B	Lower limit for v_a (m/s)
0.4—0.7	0.61	1.55	0.31	1 curve (1)	1.09	$3.96 \cdot 10^{-3}$	10^{-5}
0.5—1.5	0.75	1.85	0.32	1 curve (2)	1.10	$5.78 \cdot 10^{-3}$	$8 \cdot 10^{-5}$
1—2	1.6	1.6	0.34	1 curve (3)	1.10	$8.80 \cdot 10^{-3}$	$1.5 \cdot 10^{-4}$
2—3	2.7	1.3	0.31	1 curve (4)	1.09	$1.30 \cdot 10^{-2}$	$2 \cdot 10^{-4}$
5—7	6.3	1.3	0.35	1 curve (5)	1.09	$1.67 \cdot 10^{-2}$	$3 \cdot 10^{-4}$
0.9—1.12	1.0	1.1	0.39	2 curve (1)	1.07	$2.15 \cdot 10^{-3}$	
0.5—2	1.0	2	0.33	2 curve (2)	1.08	$3.11 \cdot 10^{-3}$	
0.2—5	1.0	5	0.31	2 curve (3)	1.08	$8.30 \cdot 10^{-3}$	$5 \cdot 10^{-3}$
0.1—10	1.0	10	0.28	2 curve (4)	1.07	$1.63 \cdot 10^{-2}$	
0.05—20	1.0	20	0.28	2 curve (5)	1.07	$7.07 \cdot 10^{-2}$	

Figure 3.5: Table of grain sizes and dispersion coefficients found in [5]. Parameter B used for δ_{long} in this study.

The Diffusion/Dispersion Tensor

Hydrodynamic dispersion is a tensor quantity formed by the sum of the mechanical dispersion tensor and the diffusion function.

$$\boldsymbol{D} = \begin{bmatrix} \frac{\delta_{long}u_x^2 + \delta_{tran}u_z^2}{\sqrt{u_x^2 + u_z^2}} & \frac{(\delta_{tran} - \delta_{long})u_x u_z}{\sqrt{u_x^2 + u_z^2}} \\ \frac{(\delta_{tran} - \delta_{long})u_x u_z}{\sqrt{u_x^2 + u_z^2}} & \frac{\delta_{long}u_x^2 + \delta_{tran}u_z^2}{\sqrt{u_x^2 + u_z^2}} \end{bmatrix} + D_m \quad m^2/s \tag{3.28}$$

3.4   Inter-phase Mass Transfer

There is limited research, and no apparent correlations for interphase mass transfer between gas butane and liquid bitumen. Because the source term J_s in Eqn. (3.10) and Eqn. (3.11) is a rate of mass addition to the domain, some information must be inferred from past research in order to assemble a working approximation to this phenomena.

There is a maximum amount of butane that bitumen will absorb at standard temperatures and pressures. This was found to be $\omega_{s,max} \approx 0.45$ in [23]. This implies there is a dependency on the mass fraction of butane in the J_s term. In most general terms:

$$J_s = k_L \alpha \left(\omega_{s,max} - \omega_s \right) \tag{3.29}$$

where k_L is the mass transfer coefficient, and α is the specific surface area of the gass-liquid interface. Mass is transferred from the butane gas phase only in pores where both liquid and gas phases are present. This introduces a dependency on the saturation of the liquid phase, i.e. it must be less than 1. The interfacial area is also saturation dependent, as the bitumen (or any wetting phase for that matter) will coat the grains and reduce the available pore space for the gas to exist, reducing interfacial area. This phenomenon was explored in [6] and a linear correlation between saturation and interfacial area was discovered as shown in Fig. 3.6

The area can be scaled using the grain size explored in [6] and the grain size of a VAPEX experiment:

$$A = \frac{0.359 \times 10^{-3}}{D_p} \left(-200 \, S + 200 \right) 100 \quad m^2 \tag{3.30}$$

where D_p is the grain diameter, a is the grain diameter used in [6] and b is the grain diameter from the domain being scaled. The mass transfer rate can be approximated as
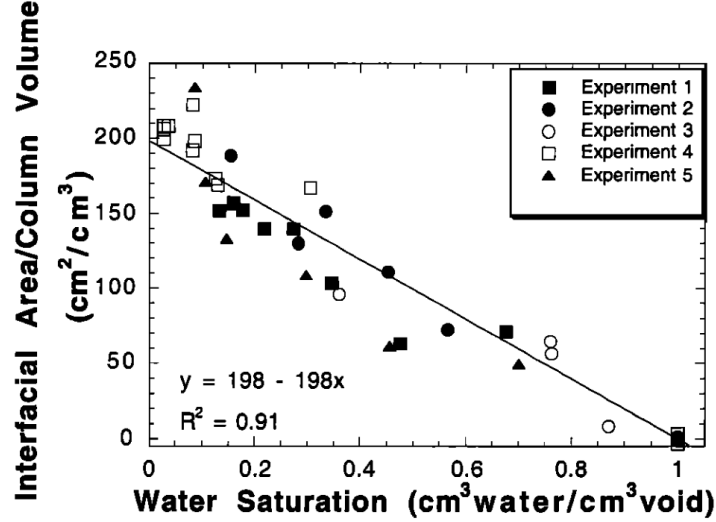
Figure 3.6: Area versus water saturation from [6] experiments 1-5. The straight line represents a linear regression to the data. The x-axes shows the water saturation and the y-axes defines the relationship between interfacial area and saturation.

a fluid flowing over a sphere. This is a approximation to the dynamics occurring in the porous medium, but in the absence of research into this phenomena it is a reasonable expectation that the mass transfer rate should depend on flow of mobile bitumen exposing immobile bitumen. The spherical aspect is to approximate the flow over a porous grain, Fig. 3.7 [42]. This approximation for the mass transfer is:

$$k_l \approx \sqrt{\frac{4D_m \boldsymbol{u_l}}{3\pi D_p}} \quad \text{m/s} \tag{3.31}$$

where D_m is the molecular diffusion, $\boldsymbol{u}_l$ is the interstitial velocity. Combining these approximations for area and mass transfer rate with the interfacail area and the concentration difference gives an approximator for the J_s source term:

$$\frac{R_s}{\rho_l} = J_s \approx \left(\sqrt{\frac{4D_m \boldsymbol{u}_l}{3\pi D_p}} \right) \left(\frac{0.359 \times 10^{-3}}{D_p} \left(-200\, S + 200 \right) 100 \right) \left(\omega_{s,max} - \omega_s \right) \quad \text{s}^{-1} \tag{3.32}$$

It is not expected that this formulation will provide interphase mass transfer rates accurately in the domain, but rather will give an order approximation to a constant value that

should be able to predict interphase mass transfer in a VAPEX domain. The expectation is that a prefactor, β can be discovered based on the interphase mass transfer approximator such that:

$$J_s \approx \beta \left(1 - S\right) \left(\omega_{s,max} - \omega_s\right) \tag{3.33}$$
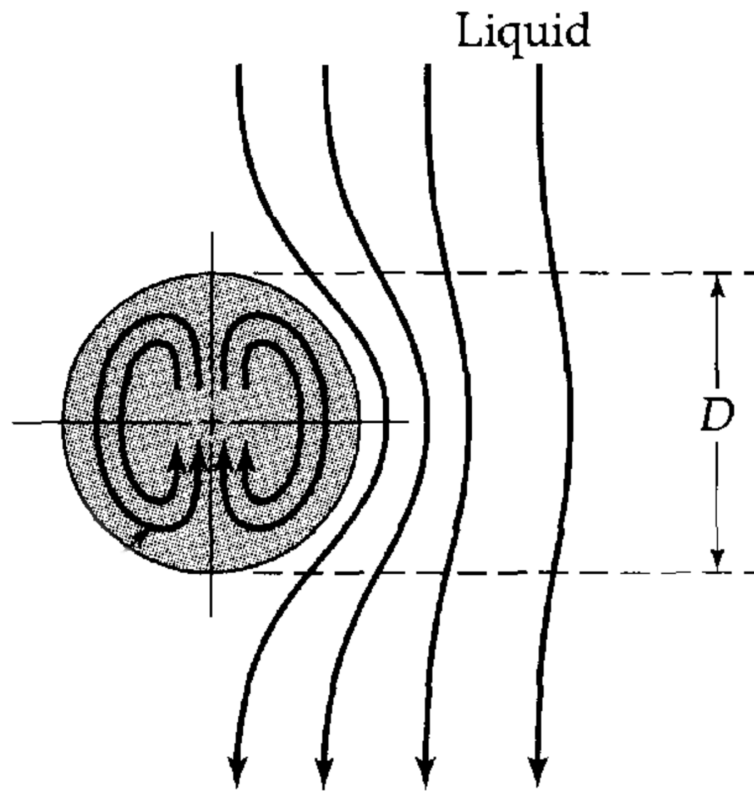
Figure 3.7: Creeping flow over a sphere. [7]

Chapter 4

Solution Setup

Having the model defined, the focus must shift to how to setup and solve such a non-linear problem. The resulting non-linear PDE system solution is achieved using the Chebyshev spectral collocation method coupled with a Newton-Krylov non-linear solver. Special attention is paid to the time discretization due to the stiff nature of the problems competing timescales, namely flow versus mass transfer. Finally special attention must also be paid to the boundary conditions and how they can best mimic the experiments available.

The choice to use Chebyshev spectral collocation was made due to the non-linearity of the proposed model. Chebyshev methods involve a global interpolant, solving the entire domain with a single high order polynomial approximation for each timestep, using fewer grid points. Keeping the number of grid points on which to solve low, while maintaining a high order of accuracy was beneficial to a system with non-linear dynamics. This method is robust and able to perform with high order solutions but is not found in any open source package. As such, the solver was developed in Python to implement the VAPEX model. Chebyshev solutions have a place in chemical engineering research projects as a simple and effective method for model solutions, provided the requirements of the system in question can be matched to the requirements of the Chebyshev polynomial collocation method, namely smoothness of the solution, boundary, and initial conditions.

Once the choice of solution method was made, choosing a non-linear solver was required. This project utilizes the Newton-Krylov solver found in the Python SciPy package. Krylov subspaces are a mathematical construct of superior linear solution speed and accuracy. The Newton method of solving a non-linear problem is coupled with the Krylov subspace in order to achieve results without calculating a Jacobian directly, making solutions of highly non-linear large scale coupled PDE's possible.

Solving for two coupled fields (the mass fraction of butane and the saturation of the liquid phase) was complex due to the disparate characteristic time scales for each domain independently. This was a stiff problem, and since the timescales we are interested in simulating are in the order of thousands of seconds, while the interface for the mass transfer is sharp and relatively slow moving, making for a difficult resolution with respect to time. Generally in a stiff problem one must sacrifice long simulation times or accuracy. In an effort to mitigate the detrimental effects of the stiffness of this system the Backward Euler and Crank Nicolson implicit schemes were employed to provide everywhere-stable solution spaces. Adaptive time stepping by comparison of the order(Δt) and order(Δt^2) time discritization schemes allowed mitigation of some of the negative aspects of the disparate time scales. However, the first order Backward Euler is in stark contrast to the Nth order Chebyshev polynomial solution, where number of grid-points dictates the order of the polynomial interpolant.

Without solving for the gas phase, the domains must be carefully considered in order to properly simulate a VAPEX system while maintaining the physical plausibility of the simulation. The boundary conditions for the mass fraction are different than those for the saturation domain.

Initial conditions for a spectral method require smooth transitions or risk introducing error before the first time step. As a spectral collocation method approximates a solution with an interpolant formed from sine and cosine functions, the basic requirement for an initial condition is that it can be approximated without discontinuity. In the case of VAPEX, this means the mass fraction of butane must be smoothly introduced in the initial condition.

A variety of physical requirements exist to use the developed solver to simulate an experiment. Things like permeability, porosity, heterogeneity fields, densities, domain sizes etc. must all be accounted for in the solution setup.

4.1   Chebyshev Collocation Methodology

An orthogonal function set forming a linearly independent function space is constructed to describe any continuous function within a given domain:

$$y(x) = \sum_{i=0}^{\infty} c_i \, p_i(x) \tag{4.1}$$

where $y(x)$ is the function we wish to describe using the sum of weights c_i with orthogonal polynomial choice p_i. The choice of polynomial is only restricted by the linear independence and orthogonality of the set.

Equation (4.1) represents a polynomial function which solves the function $y(x)$ exactly at each point x_i. In spectral interpolation a combination of sine and cosine functions of varying wavelengths, phases, and amplitudes are constructed in the infinite sum in order to replicate a desired function. The most notable is the Fourier series. Spectral interpolation using Chebyshev polynomials follows this structure as long as the function being described is limited domain such that $x \in [-1, 1]$.

By interpolating a function with a finite sum of weighted polynomials, we enforce that at pre-selected discritization points the actual solution is exact at the interpolated function:

$$y(x_i) = P(x_i) \tag{4.2}$$

where:

$$P(x) = \sum_{i=0}^{n} c_i \, p_i(x) \tag{4.3}$$

The Chebyshev polynomials of the first kind are selected for p_i, restricting the domain such that $x \in [-1, 1]$. The Chebyshev polynomials of the first kind are defined as:

$$T_n(x) = \cos(n\theta), \qquad \text{where} \quad x = \cos(\theta) \tag{4.4}$$

Figure 4.1 shows the first six Chebyshev polynomials. They are orthogonal making them ideal as a function space capable of interpolation on the required domain. Like a Fourier series, the attractive quality of Chebyshev interpolation is that even with a limited number of polynomials the order of the interpolant is high. This allows for rapid convergence to a solution using few collocation points, or in terms of the solution to partial differential equation (PDE) there is no requirement for a large number of nodes in order to solve a PDE with high order accuracy. Unlike Fourier series, the domain is not required to be periodic, or forced to be periodic by replication. Chebyshev polynomial interpolation requires a domain of $[-1, 1]$ in each dimension. This restriction is beneficial in the study of the VAPEX system as we can scale the model or the domain and the resulting derivative matrix to match the domain of study when no complex geometries are considered. The obvious downside is that the domain must be rectangular, i.e. no complex geometries can be considered.

The infinite sum of weighted Chebyshev polynomials will interpolate any function in the domain perfectly for any chosen set of collocation points $x_i \in [-, 1, 1]$. In the real-world

41
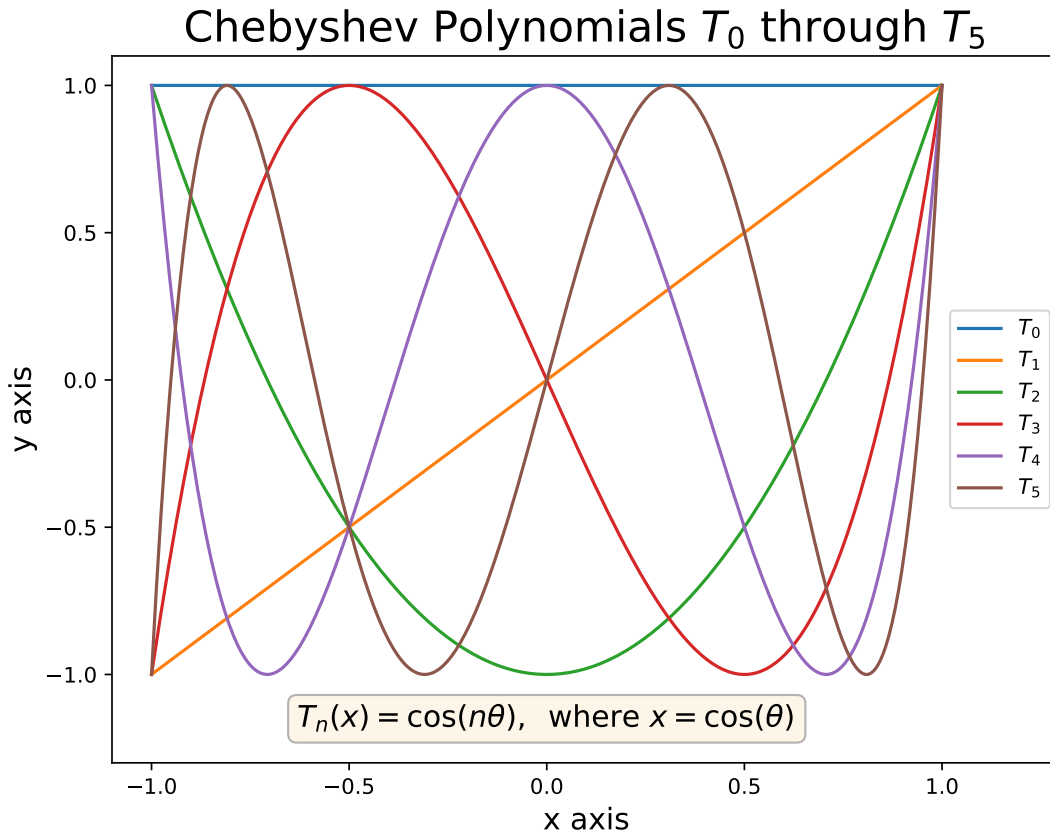
Figure 4.1: Chebyshev polynomial examples.

event that the interpolation will be an approximate solution to a function as opposed to and exact solution, the number of weighted polynomials, n, will be capped according to the accuracy required or the computing power available. The choice of point locations aids in both accuracy and computational expense by simplifying the process of approximating derivatives of Chebyshev polynomial interpolants. Additionally the choice of collocation points will directly limit the effect of Gibbs ringing. The choice of discretization points with exceptional results in all realms are the Gauss-Lobatto points [8]. Instead of linearly discretizing the $[-1, 1]$ domain, the Gauss-Lobatto points are chosen as if a unit circle's circumference was divided into equal arc lengths and projected onto the $1D$ domain. See 4.2 for a visual example:
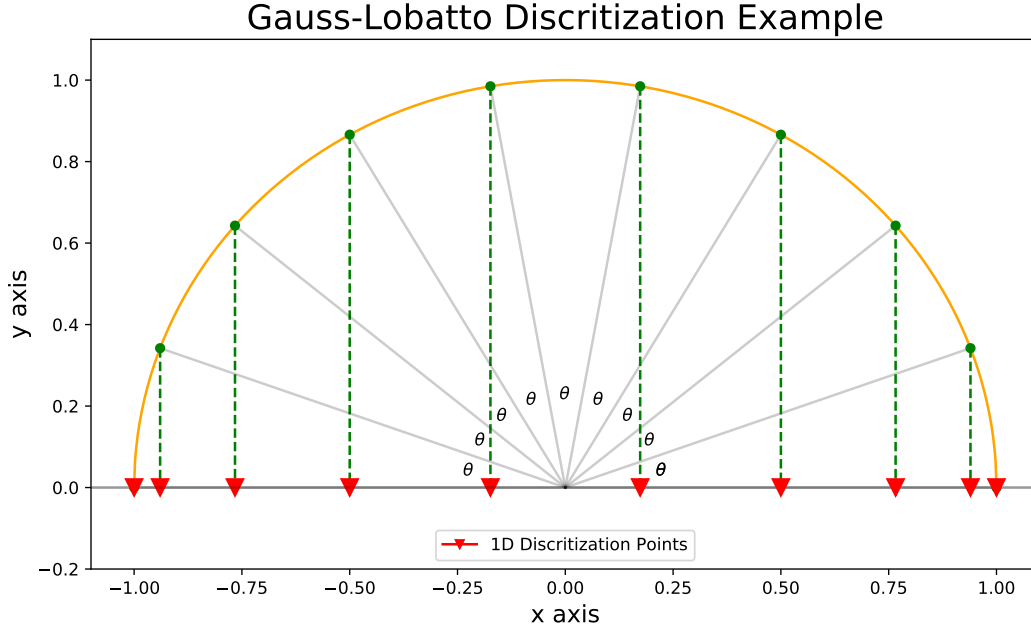
Figure 4.2: Example of the 1D discretization of a $[-1, 1]$ domain using Gauss-Lobatto points.

Once the discretization points are chosen, the derivative of the discretized polynomial interpolant can be calculated by taking the derivative of the interpolating summation:

$$P'(x) = \frac{d}{dx} \sum_{i=0}^{n} c_i \, T_i(x) \tag{4.5}$$

If we know the values at the discretization points x_i then the derivative can be expressed as a linear combination of the polynomial at those discrete points [43]:

$$\begin{bmatrix} P'(x_0) \\ \vdots \\ P'(x_n) \end{bmatrix} = \begin{bmatrix} d_{0,0} & ... & d_{0,n} \\ \vdots & \ddots & \vdots \\ d_{n,0} & ... & d_{n,n} \end{bmatrix} \begin{bmatrix} P(x_0) \\ \vdots \\ P(x_n) \end{bmatrix} \tag{4.6}$$

The derivative matrix has been calculated, and adapted to reduce error by methods derived in previous works [44, 43, 8, 45], recreated here as a generalized algorithm, also shown in Fig. 4.3:

$$(D_N)_{00} = \frac{2N^2 + 1}{6} \tag{4.7}$$

$$(D_N)_{NN} = \frac{-2N^2 + 1}{6} \tag{4.8}$$

$$(D_N)_{jj} = \frac{-x_j}{2\left(1 - x_j^2\right)}, \ j = 1, ..., N - 1 \tag{4.9}$$

$$(D_N)_{ij} = \frac{c_i}{c_j} \frac{(-1)^{i+j}}{(x_i - x_j)}, \ i \neq j, \ i, j = 0..., N \tag{4.10}$$

$$c_i = \left\{ \begin{array}{ll} 2, & i = 0 \ or \ N \\ 1, & otherwise \end{array} \right\} \tag{4.11}$$

Figure 4.3: The derivative matrix for Chebyshev Collocation, [8]

This derivative matrix can be applied in any dimension to calculate derivatives of vectors or matrices. It is sizeable to any number of nodes, but has been shown to have increasing amounts of error as the order of the approximation increases [43]. The Chebyshev method allows for very high ordered approximations with substantially less grid points than other methods.

4.2 Newton-Krylov Methods

The Newton-Krylov method is a non-linear solution tool. A Krylov subspace is a set of spanning vectors generated from a linear algebraic system of equations, and uses its own previous vectors to iterate the next in the spanning set. If we start from the idea of a linear system:

$$\boldsymbol{Ax} = \boldsymbol{b} \tag{4.12}$$

then the Krylov subspace can be assembled as:

$$\mathcal{K}_r = \text{span}\{r_0, A^2 r_0, ..., A^{r-1} r_0\} \tag{4.13}$$

where:

$$r_0 = b - Ax_0 \tag{4.14}$$

The Krylov subspace forms a spanning set, and is used to form a basis of a solution space. Since the previous vector is used to calculate the next, this process can be initialized and attempted using small subsets of the fully spanning set and checking residual convergence. If the system converges with only a limited number of spanning vectors, then there is no need to calculate the remaining set. This allows for quick convergence at lower computational cost of a linear system. Additionally each spanning vector is simply a single matrix multiplication of the previous vector.

To solve a non-linear problem, we establish a residual function such that:

$$F(\boldsymbol{x}) = 0 \tag{4.15}$$

A Newton method solve successive linear systems such that:

$$J(\boldsymbol{x})d_x = -F(\boldsymbol{x}) \tag{4.16}$$

where $J(\boldsymbol{x})$ is a Jacobian matrix of $F(\boldsymbol{x})$. The computational cost of computing a Jacobian at every step is expensive, and so approximations of the Jacobian become attractive. A Krylov subspace can be used to form a trial subspace, and trial vector. The Jacobian approximation can be created iteratively as:

$$J(\boldsymbol{x}) \cdot \boldsymbol{v} = \frac{F(\boldsymbol{x} + \epsilon \boldsymbol{v}) - F(\boldsymbol{v})}{\epsilon} \tag{4.17}$$

where ϵ is a small positive number and $\boldsymbol{v}$ is the trial vector assembled from the Krylov subspace. This is a complicated method, and as such the Newton-Krylov solver was not

implemented from scratch, but rather employed from the SciPy suite of non-linear solvers in the Python programming language. The Newton-Krylov non-linear solver in SciPy allows for an absolute tolerance to be set by the user. The absolute tolerance is the maximum value that may be returned from the L2 norm of the residual function passed to the Newton-Krylov solver, defined as:

$$L_2\left(\boldsymbol{x}\right) = \sqrt{\sum_{i=1}^{n} x_i^2} \tag{4.18}$$

4.3 Time Discretization

The Backward Euler method of discretizing time is implicit and unconditionally-stable, making it an ideal candidate for any difficult PDE. This first order accurate implicit method was applied to the solution for the conservation of mass of the liquid phase and of the butane component. Taking the coupled PDE's of the model and re-arranging for a left hand side containing only the time derivative:

$$\frac{\partial S_l}{\partial t} = \frac{-\nabla \cdot \left(\boldsymbol{v}_l\right) + J_s}{\phi} \qquad\qquad = F_1(\psi, \omega_s) \tag{4.19}$$

$$\frac{\partial S_l \omega_s}{\partial t} = \frac{-\nabla \cdot \left(\omega_s \boldsymbol{v}_l - \phi S_l \boldsymbol{D} \nabla \omega_s\right) + J_s}{\phi} \qquad\qquad = F_2(\psi, \omega_s) \tag{4.20}$$

we apply superscripts to denote time solutions and discretize in the Backward Euler method:

$$\frac{S_l^{n+1} - S_l^n}{\Delta t} = F_1^{n+1}(\psi, \omega_s) \tag{4.21}$$

$$\frac{\left(S_l \omega_s\right)^{n+1} - \left(S_l \omega_s\right)^n}{\Delta t} = F_2^{n+1}(\psi, \omega_s) \tag{4.22}$$

A second order method was employed in order to apply adaptive time stepping. The Crank-Nicolson method is also unconditionally stable and discretized as follows:

$$\frac{S_l^{n+1} - S_l^n}{\Delta t} = \frac{1}{2}\left(F_1^{n+1}(\psi, \omega_s) + F_1^n(\psi, \omega_s)\right) \tag{4.23}$$

$$\frac{\left(S_l \omega_s\right)^{n+1} - \left(S_l \omega_s\right)^n}{\Delta t} = \frac{1}{2}\left(F_2^{n+1}(\psi, \omega_s) + F_2^n(\psi, \omega_s)\right) \tag{4.24}$$

Comparison of the two solutions obtained with the Backward Euler and Crank-Nicolson method enables adaptive time step size control as follows:

$$\Delta t_{new} = 0.9 \Delta t_{old} \min\left(\max\left(\frac{\text{Local Tolerance}}{\text{L2 Norm}\left(\text{Solution 1} - \text{Solution 2}\right)}, 0.3\right), 2\right) \quad (4.25)$$

The new time step is calculated from Eqn. (4.25) with a local error tolerance set by the user. If the time step is smaller than the previous time step, the solution is discarded due to the local error not exceeding the tolerance indicated. If the time step is larger than the previous time step, the first order solution is saved as a successful solution and the new time step is used in the next solution in time.

4.4   Experimental Domain

The solution to the VAPEX model proposed must be able to replicate experimental results. The results produced in [1] are ideal candidates as the experimental parameters are well documented, the results are clear, and the domain can be approximated. Two experiments in [1] are of particular interest. Experiment 1 and Experiment 3. Both were conducted in an annular apparatus, depicted in Fig. 4.4.

The annulus consisted of two plexi-glass cylinders placed one inside the other. The space between the two cylinders was filled with glass beads to mimic the porous media of the Canadian tar sands. Bitumen was warmed until a free flowing viscosity was reached, and poured into the annulus filled with beads and allowed to settle and cool over a period of time. The bitumen used was Cold Lake.

An injector was placed on the inside of the outer cylinder to allow for continuous butane injection into the experimental domain. The injector extended down the entire length of the cylinder to mimic an injection well that had achieved communication with the producing well. The producing port was at the bottom of the annulus setup allowing for oil to flow out of experiment.

The produced oil was then processed in a way that allowed the butane to be recovered and measured. The experiment continued until such a time as it was deemed to have fully produced the domain, or significant drop off of the pseudo-steady-state production occurred. A schematic of the experimental setup is picture in Fig. 4.5

Both experiments 1 and 3 in [1] have unique glass bead sizes, permeabilities, porosities, and experimental running times. The experimental parameters are listed in table 5.2 and

table 5.4. Everything else about the two experiments is similar with regards to bitumen type, solvent type, and domains. The VAPEX model solution should be able to exhibit robustness by replicating both experiments regardless of the changes in the experimental setup.

4.4.1 Solution Domain

The annulus had the following geometric properties:

Property	Value	Units
Outer Shell Inner Diameter	2.5	Inches
Inner Shell Outer Diameter	2	Inches
Height	1	metre
Experimental Domain Volume	1154	cm^3

Table 4.1: Table of geometric properties of experiments 1 and 3 in [1]

The circumference of the outer shell's inner diameter is $\approx 0.2m$ and the circumference of the inner shell's outer diameter is $\approx 0.16m$. Unwrapping the smaller of the two circumferences gives a horizontal dimension of $0.16m$, which will be utilized to create a suitable two dimensional domain for the solution space of the VAPEX model. The height will be the same at $1m$.

The injector port is placed along the entire height of the experimental domain injecting butane vapour evenly at a single horizontal location for all vertical locations. To simplify the solution space the VAPEX model will be solved on half of a domain, considering only only the left side of the unravelled horizontal axes, with the far right representing the injection port. (see Fig. 4.6).

4.5 Boundary and Initial conditions

4.5.1 Initial Conditions

The initial condition (IC) for the saturation of the domain corresponds to a fully saturated domain. Since the independent variable being solved for was ψ the resulting initial condition was that $\psi = 0$ everywhere.

The mass fraction of butane, being subject to a Dirichlet boundary condition on the right side of the domain in order to model an injector port with communication of butane into an experimental domain, required a smooth initial condition. The equation for this IC was chosen in order to minimize the amount of butane in the domain, while maintaining the smoothness requirement in the transition from $\omega_s \approx 0$ to $\omega_s = 0.45$ at the right edge.

$$\omega_{s,IC} = \omega_{s,max} \exp\left(\frac{50\left(x - x_{max}\right)}{x_{max}}\right) \tag{4.26}$$

The ω_s IC is mapped in Fig. 4.7. The amount of butane in the majority of the domain is negligible, and as the amount ramps just prior to the Dirichlet boundary condition it mimics an experimental requirement for VAPEX called "communication". Communication is the act of removing bitumen from the domain between the solvent injector and the producer port. This allows for the experiment to commence in the complete vertical domain. By having the IC for ω_s effectively pre-saturating the bitumen near the right domain, and therefore giving it instant mobility when the simulation begins, we have effectively replicated the communication stage of a VAPEX experiment.

4.5.2   Boundary Conditions

There are two unknowns being solved, saturation (a function of ψ) and mass fraction of butane (ω_s), each requiring unique boundary conditions. The saturation phase, to which we are solving for the matrix pressure head ψ, requires a no flux condition everywhere except where the fluid is allowed to drain. The outflow condition for the experimental setup was a port with a fixed size that would allow mobile bitumen-butane to leave the domain. For the simulation it was found that by allowing the entire $z = 0$ boundary to be an outflow condition, that the physics of VAPEX would restrict the area that fluid could outflow to a small surface exactly where the outflow port would be. The reason fluid does not escape everywhere is that the viscosity of the majority of the lower domain never being reduced to the point of mobility. Height of capillary rise is present, and as such with the exception of the area that is able to flow due to the initial condition, the rest of the lower domain is held in place. Diffusion would eventually result in the entire lower domain becoming mobile. This was not a concern for these simulations as the diffusive timescale would be far too great in comparison to the drainage timescale occurring during the VAPEX simulation, and as such the outflow condition could be set across the entire $z = 0$ surface. That outflow condition corresponds to a Dirichlet boundary condition of $\psi = 0$ at $z = 0$.

Mass fraction of butane in the liquid phase constitutes the second solution domain, requiring separate boundary conditions. A no diffusive flux condition is established on all sides except where the injector port is simulated. At that side, the right edge, the mass fraction of butane in the liquid phase is set to a constant value of 0.45 representing the fully saturated bitumen-butane mixture. This boundary condition is devised to mimic the area of the domain where pure butane vapour is being injected, and the liquid domain is fully saturated at all times.

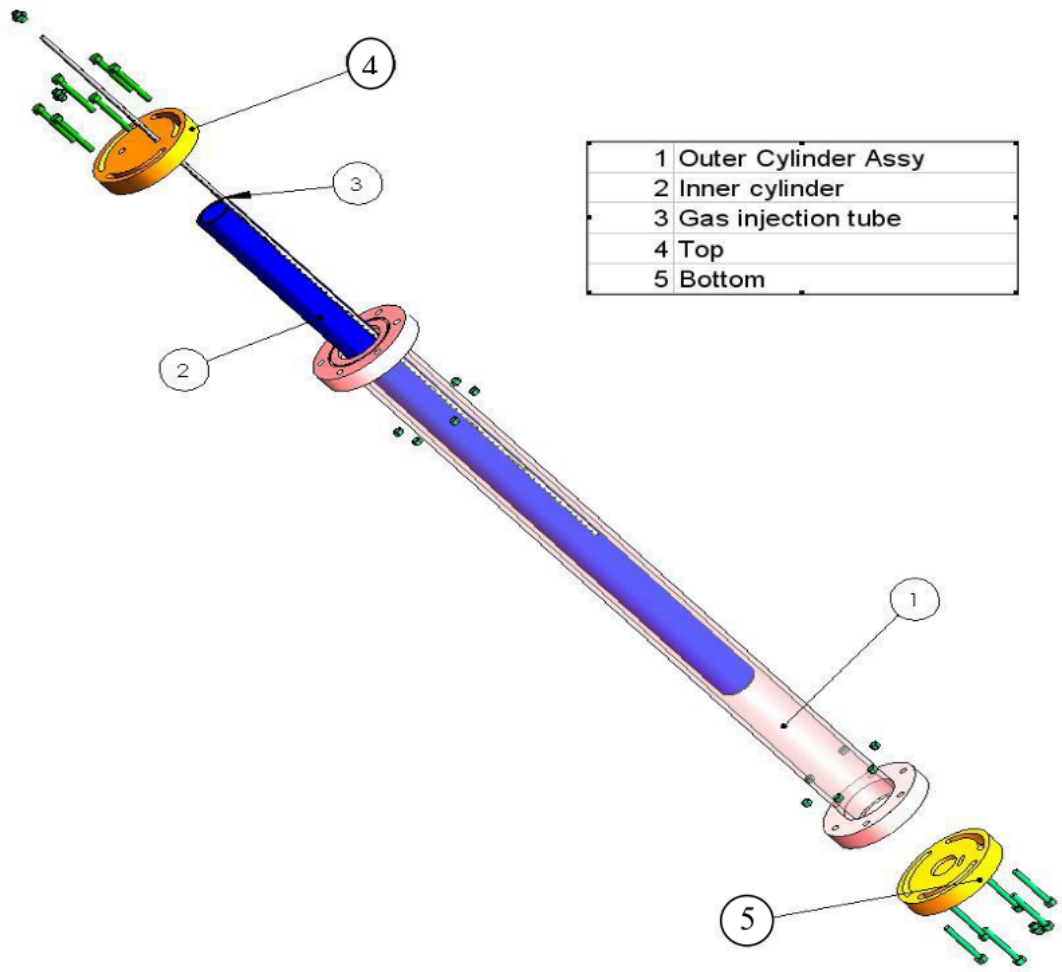| 1	Outer Cylinder Assy
2	Inner cylinder
3	Gas injection tube
4	Top
5	Bottom

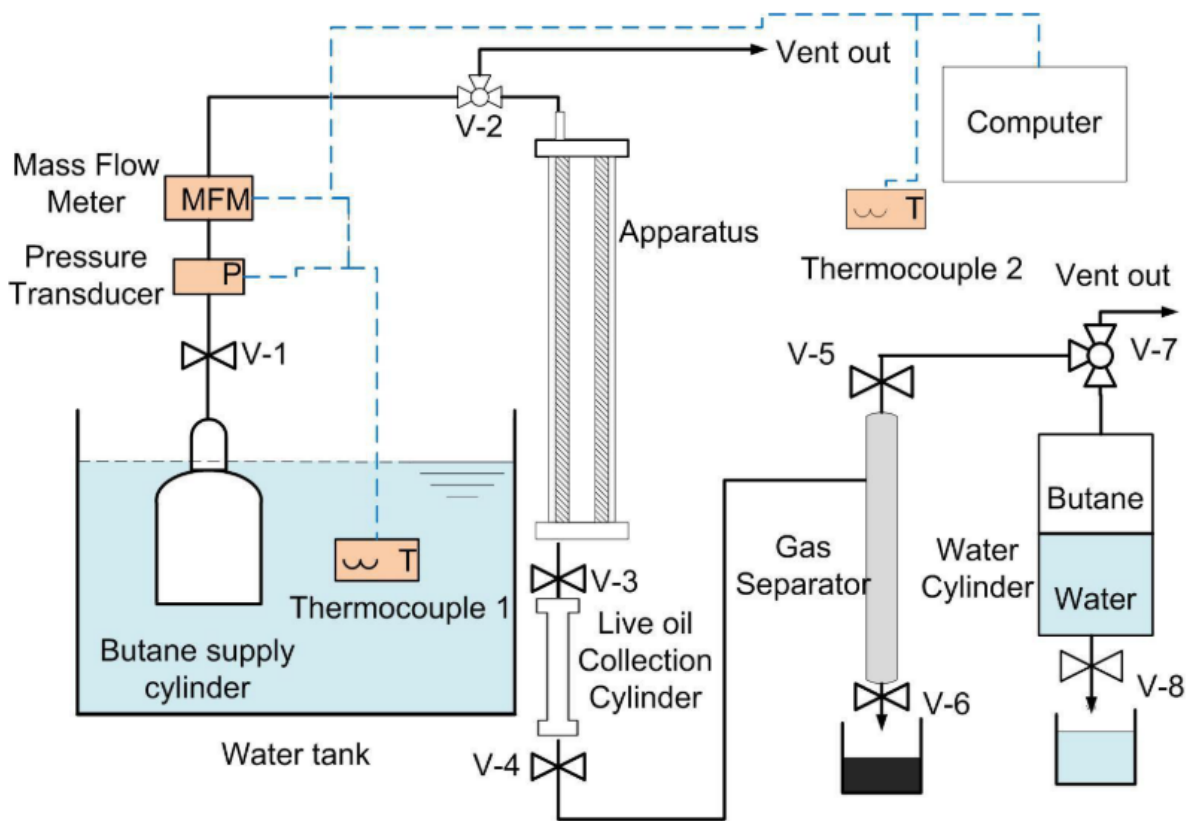Figure 4.4: Tam Experimental Setup. Used with permission

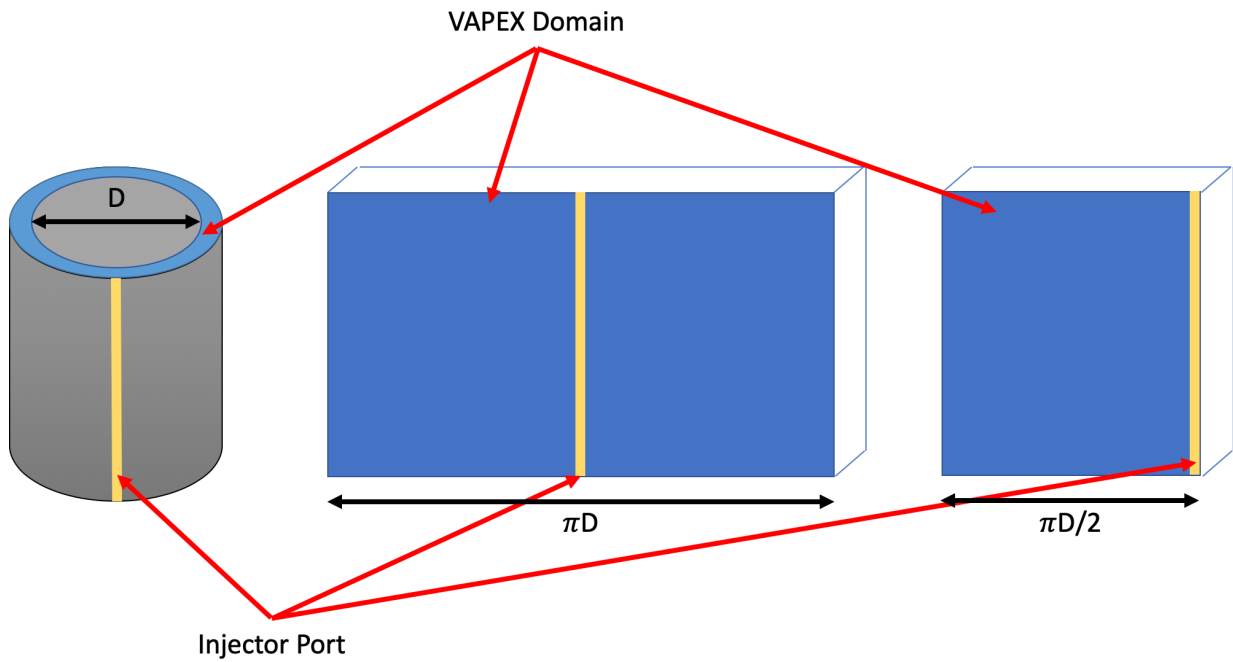Figure 4.5: Tam Experimental Setup Schematic. Used with permission

Figure 4.6: Conversion of experimental domain into simulation domain
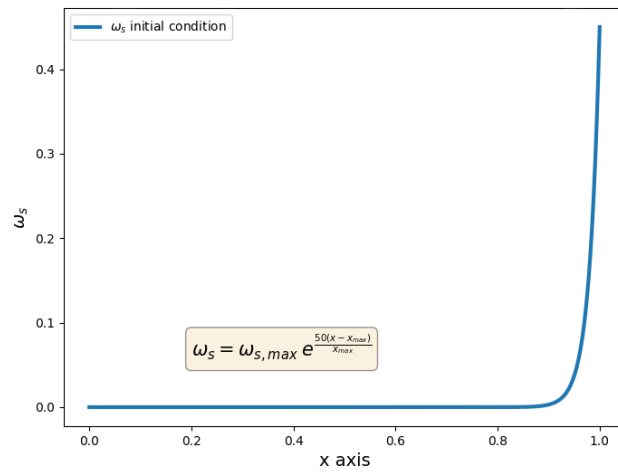

Figure 4.7: A graph in 1 dimension showing the initial condition on the mass fraction of butane.
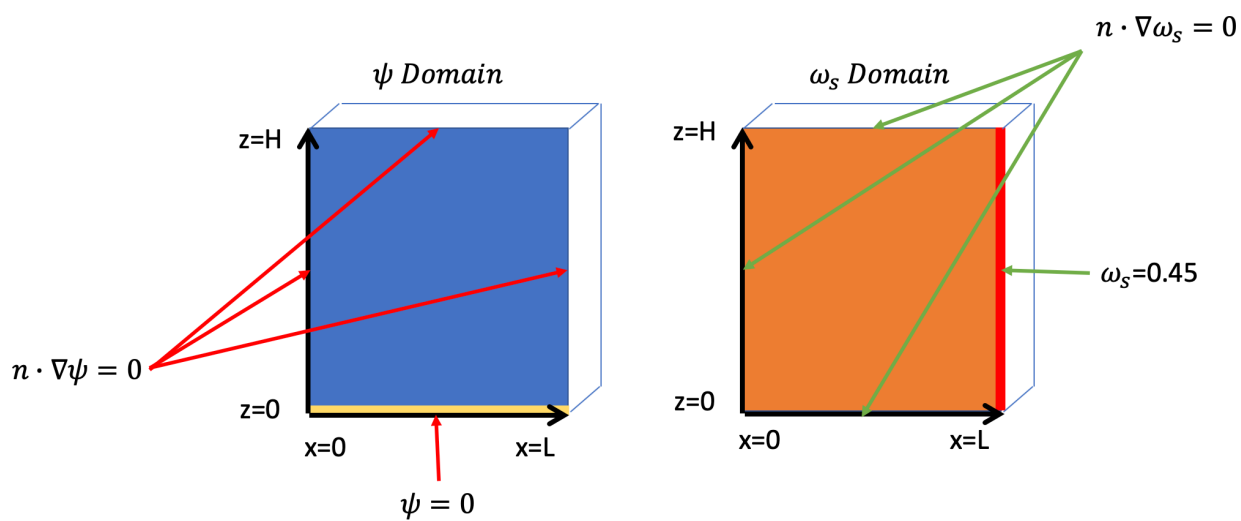
Figure 4.8: Boundary conditions of the simulation domain.

Chapter 5

Results and Discussion

5.1 Validation of Numerical Method

The numerical method used to solve the VAPEX model was custom built in a Python environment. Numerical validation of the method must first be completed in order to instill confidence when using the same numerical method to solve a new model. In order to prove that the Chebyshev spectral collocation method could be relied upon, the custom-built solver was tested on a drainage problem governed by the Richards equation using data from [2].

5.1.1 Water Flowing Through A Porous Column

The experiment conducted in [2] was one in which water flow by gravity out of a burette with glass beads. The experiment was designed to validate relative water permeability directly from relaxation time data at various saturations using nuclear magnetic resonance. The drainage time, cumulative water production, and gravity-capillary equilibrium data extracted and used to populate the Richards model, Eqn. (2.16), and solved using the numerical Chebyshev spectral collocation method. The experimental parameters are found in Table 5.1.1.

Mapping the gravity-capillary equilibrium from the experiment, shown in Fig. 5.1, allowed for the generation of a capillary pressure curve, and the Van Genuchten parameters required to describe that curve. These data are later used to scale the capillary pressure curve in VAPEX simulations using the Leverett J function.

Property	Value	Units
Cylinder Diameter	0.8	cm
Height	125	cm
Grain Diameter	300	μm
Porosity	0.383	-
Permeability	100	Darcy

Table 5.1: Table of experimental parameters [2]

Validation in 1D

The solution to the Richards equation, Eqn. (2.16), in one dimension was used to validate the Chebyshev spectral collocation method. In order to replicate an experimental value the production from the simulation will be compared to experimental production. The one-dimensional solution has a no-flux boundary condition at the top of the domain, and a fully saturated condition at the bottom.

$$\left.\frac{\partial \psi}{\partial z}\right|_{z=1.25m} = 0 \tag{5.1}$$

$$\psi\left(z=0\right) = 0 \tag{5.2}$$

The simulation will be conducted with 40 collocation points, with an absolute tolerance of 1×10^{-6} and a local error tolerance of 1×10^{-3}. The data will be compared to the cumulative water production from a three-dimensional experiment. The experiment was conducted in a cylinder with a diameter of 0.8 cm which was allowed to drain through the entire bottom, and so the one-dimensional simulation will be extrapolated as a three-dimensional volume by multiplying the flux through the bottom by the cylindrical area so as to approximate cumulative water production.

The qualitative comparison is found in Fig. 5.3. As is evidenced by the cumulative production curve comparison, the Chebyshev spectral collocation method is capable of solving the non-linear Richards equation in one dimension. Some variation in the production curves should be expected by the approximation of a capillary pressure curve from the equilibrium state of the experiment, as well as simulation properties being absolutely homogeneous. The simulation predicts 16.2055 grams of water produced after 10 000 seconds of simulated time. The data set from [2] showed ≈ 16.2 grams of water produced at ≈ 9000 seconds.
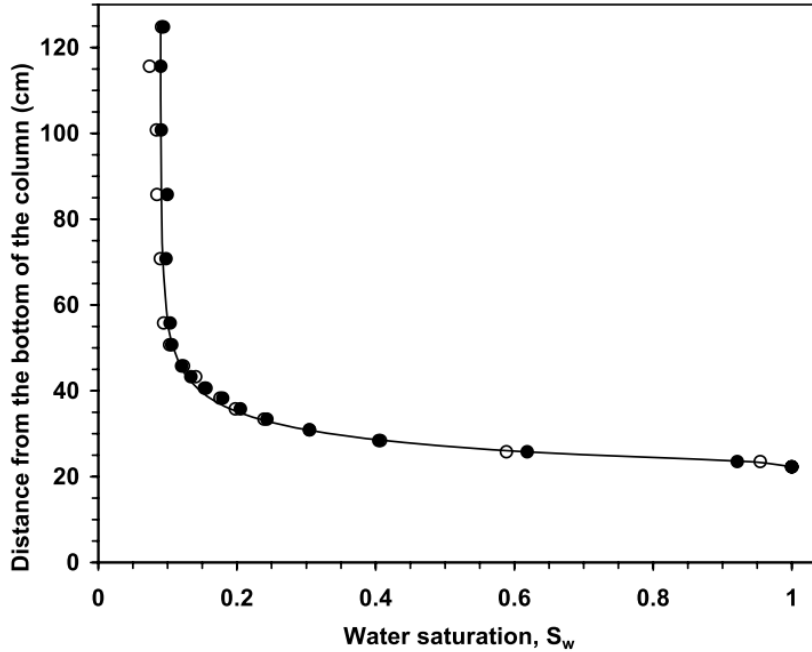
56

Figure 5.1: Water saturation distribution at gravity-capillary equilibrium in experiment [2] (the Brooks-Corey parameter was $\lambda = 5.07$), used in this study to generate Van Genuchten parameters

In order to measure the convergence of the Chebyshev spectral collocation method a number of experiments were run on the one dimensional Richards equation including varying grid size, absolute error tolerance, and local error tolerances. The baseline solution of a 30 point grid was used to compare local and absolute error tolerances. The relative error between solutions of cumulative production at 10 000 seconds of simulation time is plotted for each experiment.

The number of grid points was varied from 10 through 60 to gauge the change in cumulative production at 10 000 seconds of simulation time. All grid convergence experiments were conducted with an absolute tolerance of 1×10^{-4} and a local tolerance of 1×10^{-2}. The relative convergence between successive grid sizes was calculated an displayed in Fig. 5.4. As is evidenced, changing from 30 grid points to 40 and then 50 has relatively little effect on the amount of error introduced. The increased relative error between 60 grid points and 50 can be attributed to a flaw in the derivative matrix explored in [43] that shows stabilization for lower order approximations can be introduced at the expense of accuracy
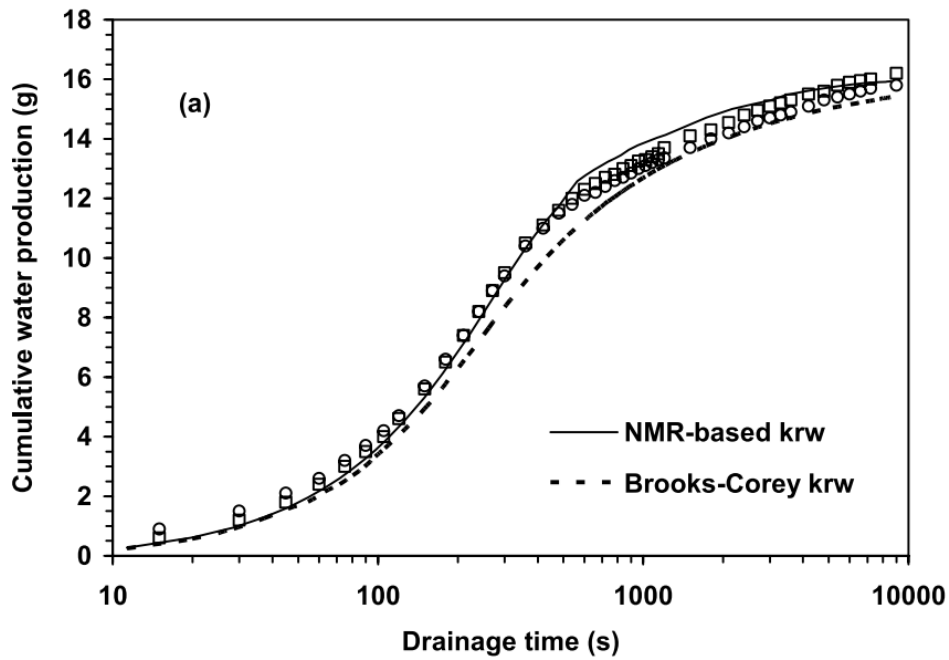
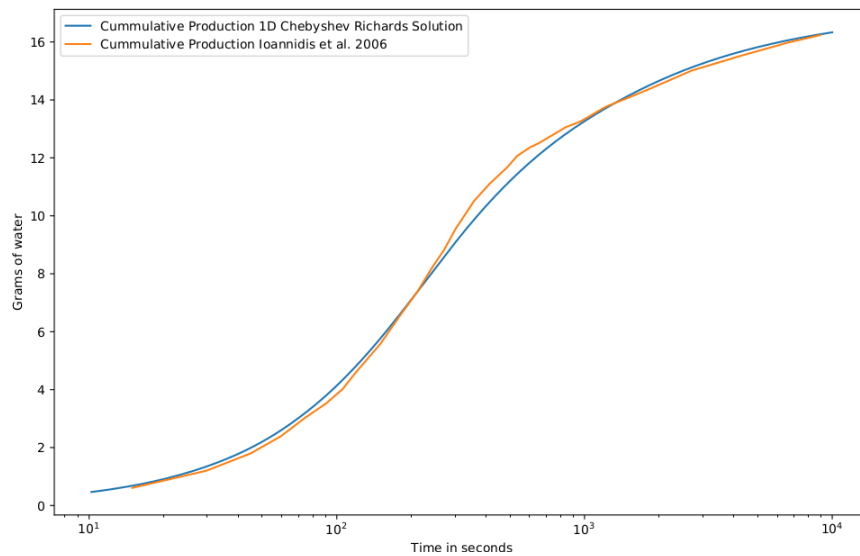Figure 5.2: Cumulative water production in [2], original data

Figure 5.3: Cummulative water production in 1D simulation of Richards equation compared to data in [2]
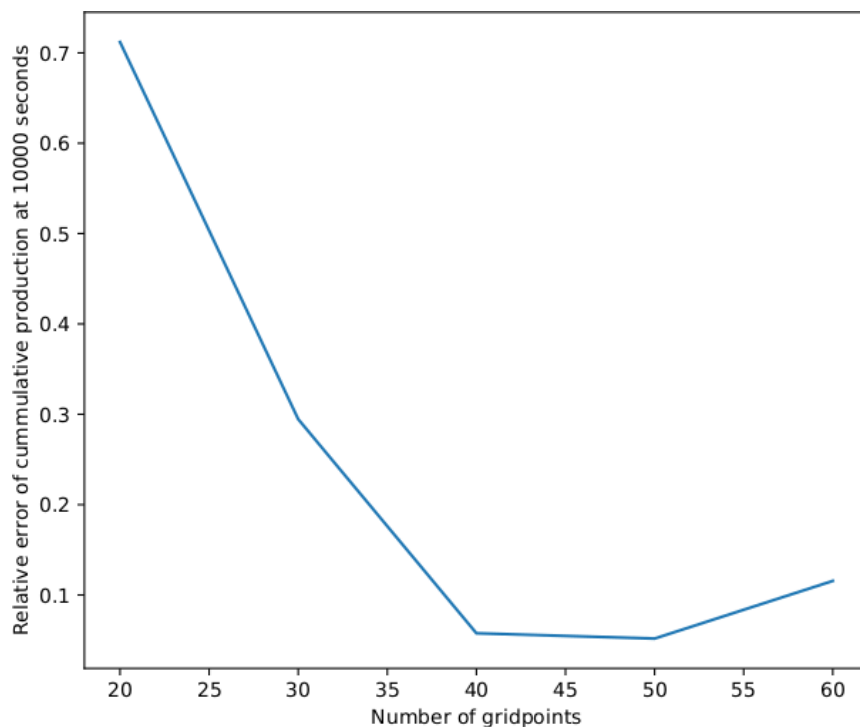
Figure 5.4: Relative error of the 1D Richards solution of cumulative production at 10 000 seconds using successively larger number of grid points.

for higher order approximations. As the number of grid-points translates into the order of the approximation, there is little gain in solving for more than 30 to 50 grid-points.

The absolute error is calculated as the L2 norm of the residual function being solved in the Newton-Krylov solver. The relative error between successively smaller absolute error tolerances is shown in Fig. 5.5. The plot shows that there are benefits to decreasing the absolute error tolerance, but what is not shown in the graph is that the time it takes to solve is exponentially increased as the absolute error tolerance is exponentially decreased. A compromise when choosing an absolute error must be established between the time the solution takes and the amount of error that can be tolerated. For the 1D Richards equation solution, the relative error between successively decreasing absolute error tolerances is negligible after 1×10^{-4}.

The local error tolerance constrains the error between the first and second order solutions in time. The relative error between successively smaller local error tolerances is shown in Fig. 5.6. The plot shows some benefit to decreasing the local error tolerance, but
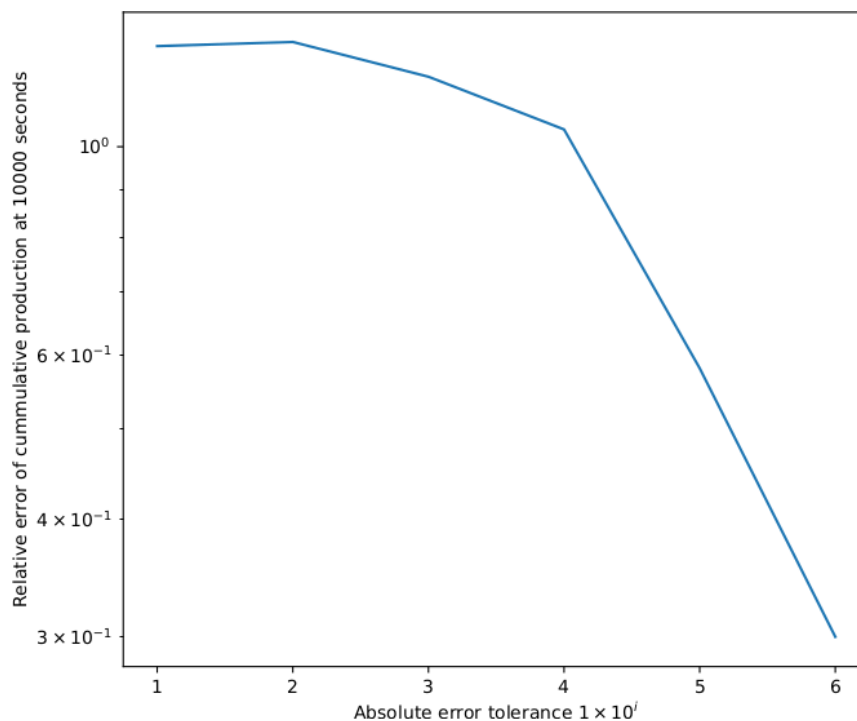
Figure 5.5: Relative error of the 1D Richards solution of cumulative production at 10 000 seconds using successively smaller absolute error tolerances.

much like absolute tolerance, the increase in accuracy is a decrease in the time it takes to solve the system. For the 1D Richards equation solution, the relative error between successively decreasing local error tolerances is ideally found to be 1×10^{-2}.

Validation in 2D

Solving the VAPEX system will require a two-dimensional solution, so validating the Chebyshev spectral collocation method in two dimensions can be achieved using the same methodology as for the one-dimensional problem. The same data set from [2] were used and a two-dimensional rectangular domain was multiplied by an appropriate width to simulate a three-dimensional domain so that the outflow area matched the open cylinder outflow from the experiment. The simulation in two dimensions was run with a height of 1.25 metres, a width of 0.1 metres and an assumed depth of $5.02654824574 \times 10^{-6}$. The grid size is 30 by 30 for the two dimensions. The absolute and local error is set to 1×10^{-4} and 1×10^{-2} respectively. The boundary conditions are identical to the one-dimensional
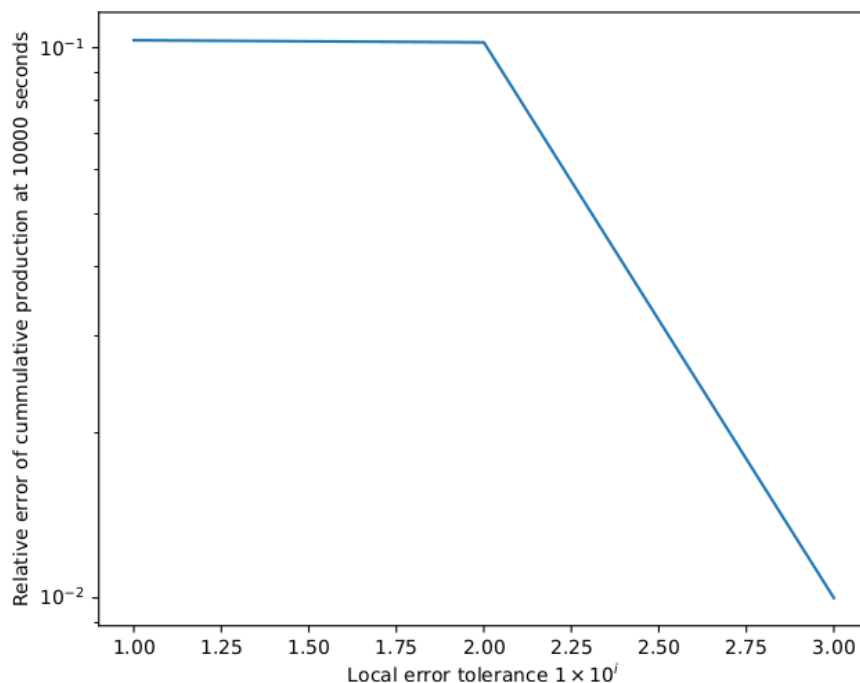
60

Figure 5.6: Relative error of the 1D Richards solution of cumulative production at 10 000 seconds using successively smaller local error tolerances.

solution, the fluid is allowed to flow out the bottom of the domain.

Qualitatively it can be visually confirmed in Fig. 5.7 that the cumulative water production in the two-dimensional model is as expected. The amount of water produced in the two-dimensional simulation was 16.2 grams, which matched the experimental results out of the geometry in the time given. The cumulative production profile varied from the one-dimensional solution, producing less volume of water earlier, and later during the simulation which may be attributed to the two-dimensional rectangular geometry.

Saturation and velocity profiles of the domain are shown at three distinct times in Fig. 5.9. A $t = 10$ we see that during the first ten seconds of outflow that saturation is already decreasing from the top down as expected from a gravity-driven flow. The saturation profile at $t = 200$ is the approximate point in time when half of the total drainable water has been drained from the domain. At $t = 9000$ the domain is almost completely drained, and the majority of the remaining saturation represents the volume trapped by capillary forces. Velocity profiles are of interest as an indicator of how fast specific areas of the domain are draining, but ultimately a fully open outflow across the
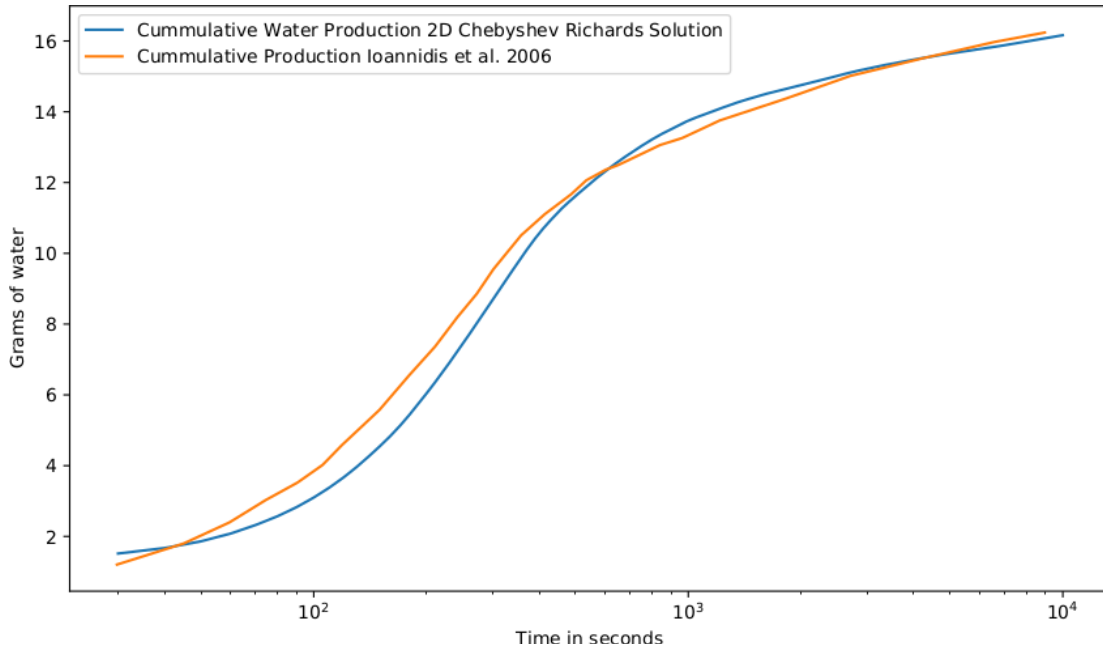
61

Figure 5.7: Cummulative water production in 2D simulation of Richards equation compared to data in [2]

$z = 0$ plane makes the velocity invariant in the horizontal domain.

For interest, and to show that that outflow restriction is possible, a reference 2D Richards solution profile is shown in Fig. 5.9 which has a domain of 1 metre by 1 metre, and an outflow condition where water can only leave the domain via a 10 cm outflow on the lower right of the domain at $z = 0$. Having the outflow condition forces a horizontal pressure to drive flow from left to right across the base of the domain showing how the governing equation of Richards is satisfied in more than one dimension. The non-symmetric saturation profile, most prominently seen at $t = 500$, is exaggerated in a domain of this width (1 metre) where the outflow is disparate and tangential capillary pressure forces are unable to equilibrate. At $t = 1990$ seconds the symmetry of the saturation profile is returning as capillary pressure equilibrates.
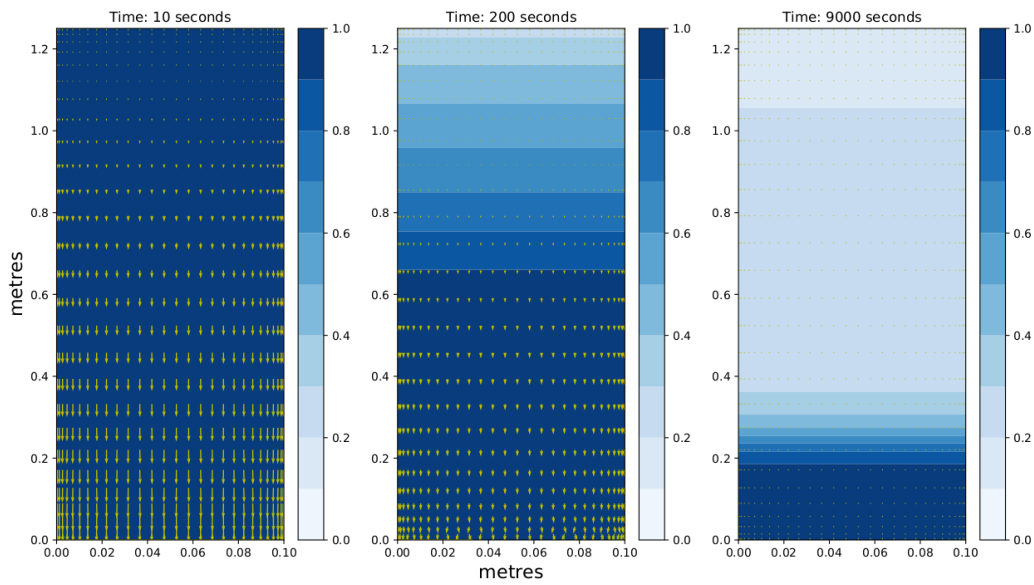
Figure 5.8: Saturation profiles in 2D simulation of Richards equation with full outflow condition at bottom at times $t = 10$, $t = 200$, and $t = 9000$.
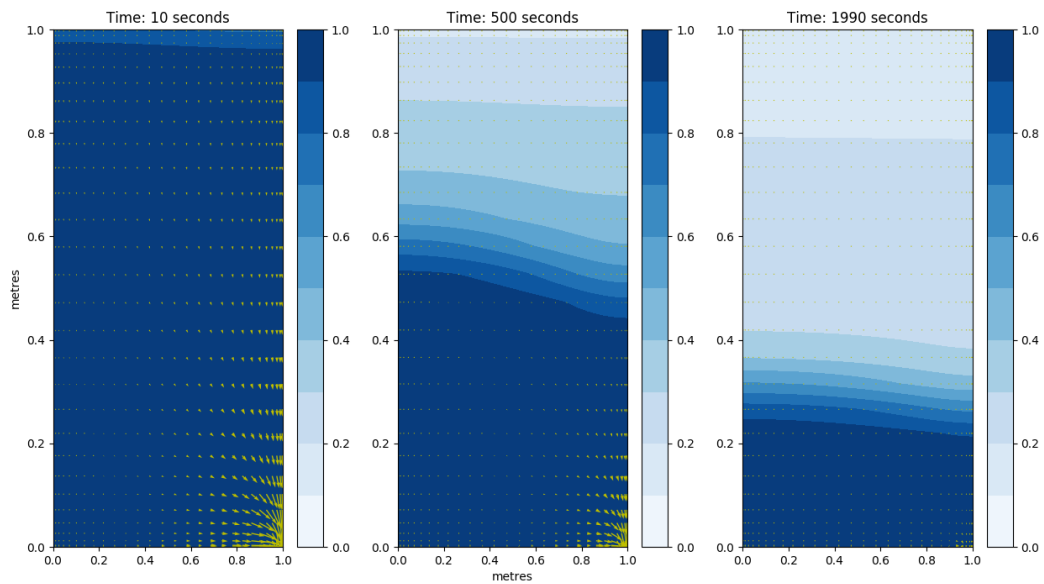

Figure 5.9: Saturation and velocity profiles of a 2D Richards solution with a 5 cm outflow condition on the lower right of the domain at $t = 10$, $t = 500$, and $t = 1990$

5.2   Solution of the VAPEX Model

The numerical solution to the VAPEX model is validated against experimental results found in [1]. This experiment was carried out in an annulus apparatus shown in Fig. 4.4. Sintered glass beads were loaded into the void between Plexi-glass cylinders acting as the porous domain. Bitumen was heated until able to flow, and added into the glass bead domain, which was also kept hot so the bitumen would completely saturate the porous medium. The injector port ran down the entire length of the experiment, delivering butane vapour evenly at all heights. The bitumen-solvent mixture was able to drain out of a collector port at the bottom of the experiment. Initially, the injector was heated and bitumen was allowed to drain surrounding the injector mimicking communication found between an injector well and producer well in a field VAPEX setup. The experiment was started by introducing pure butane into the pre-drained porous medium surrounding the injector port. As expected, the setup produced bitumen solvent mixture for the duration of the experiment. Measurements of bitumen-solvent mixture flow rate were made, as were measurements of the average butane mass fraction in the produced oil, and the cumulative bitumen production.

In order to simulate experiment 3, the VAPEX model must be populated with experiment dependent parameters. A table of parameters is included to detail the experimental setup dimensions and parameters (table 5.2).

Parameter	Value	Unit
Inner cylinder outer diameter	2	inches
Outer cylinder inner diameter	2.5	inches
Height	1	metre
Grain size	0.59	microns
Porosity	0.39	unitless
Permeability	300	Darcy
Time	1221	minutes
Bitumen density	980	kg/m^3
Butane density	573	kg/m^3
Bitumen viscosity	23.2	kg/ms
Butane viscosity	1.71×10^{-4}	kg/ms

Table 5.2: Table of parameters for experiment 3 [1]

The injection port being inserted into the porous domain through the whole height of the

experiment allows for the vapour chamber to form with two drainage fronts moving laterally away from each other around the circumference of the annulus. The inner circumference is $\approx 0.1596m$ and the outer circumference is $\approx 0.1995\ m$. We take the inner circumference as the width of the two-dimensional domain as it should represent the point at which the two drainage fronts meet on the opposite side of the annulus. The two-dimensional simulation has no need to simulate both sides of the drainage fronts, as they are assumed symmetric, and as such the domain width is halved to ≈ 8cm. To aid in computation time, the domain was reduced to 6 cm so the x-axis nodes were more tightly packed in order to better capture the transition zone interface for the duration of the simulation. This domain size will change the length of time the dynamics of the system will evolve when compared to experimental data.

Cumulative production of bitumen as a function of time is measured directly in [1], and those data points are plotted against cumulative production of bitumen from the simulation domain. Because the experiment has a width between the cylinders, the two-dimensional simulation must be extrapolated by a depth in order to match the production of the experiment. The width of the domain between the cylinders is 0.5 *inches* which is $0.0127\ m$. We use this width to determine the production of the simulation. The average production rate of bitumen in experiment 3 from [1] is found in table 5.3.

Production	Value	Unit
Average production rate (bitumen)	0.35	g/min

Table 5.3: Table of production results for experiment 3 [1]

Since the bitumen production reported from the entire annulus domain, in order to match values in the simulation a one-sided production amount is calculated from experimental data. By scaling the production rate into grams per second for a single side of the symmetrical experiment, a value of $223 \times 10^{-3}\ g/\left(s \cdot m\right)$ when halved for a one-sided flow. This value is useful for determining if the simulation is evolving appropriately, but for an accurate comparison to the desired value of bitumen production a better approximation to experiment 3 results is to a compare the cumulative bitumen production over time. The experimental data is replicated in the simulation overlay.

The interphase mass transfer term in the simulation had to be approximated in order to finish populating the model. Equation (3.32) requires an interstitial velocity, and domain dependent variables of saturation and mass fraction of butane. By choosing values for saturation, and mass fraction of butane that appear appropriate for the conditions of

interphase mass transfer to occur, an order of magnitude estimate for a constant prefactor value for Eqn. (3.33) can be discovered. For interphase mass transfer to occur, butane vapour must be present in a pore space with bitumen. A choice of saturation 0.9 is made as an estimate for when diffusion of butane has penetrated the pore and mobility of some of the bitumen present has allowed a gas saturation of 0.1 to occur. For saturation to have dropped below one, the bitumen must already have been mobile which indicates a viscosity reduction. As can be intuited from Fig. 3.3, when the mass fraction of butane accounts for at least 0.15 of the liquid phase mobile bitumen can flow in the pore space. A mass fraction of butane of 0.15, and a saturation of 0.9 are chosen to estimate Eqn. (3.33). The result is an estimated constant prefactor value of 0.004427. This value is rounded to 0.005 s^{-1} and used in the VAPEX model otherwise populated with the parameters from experiment 3 in [1]
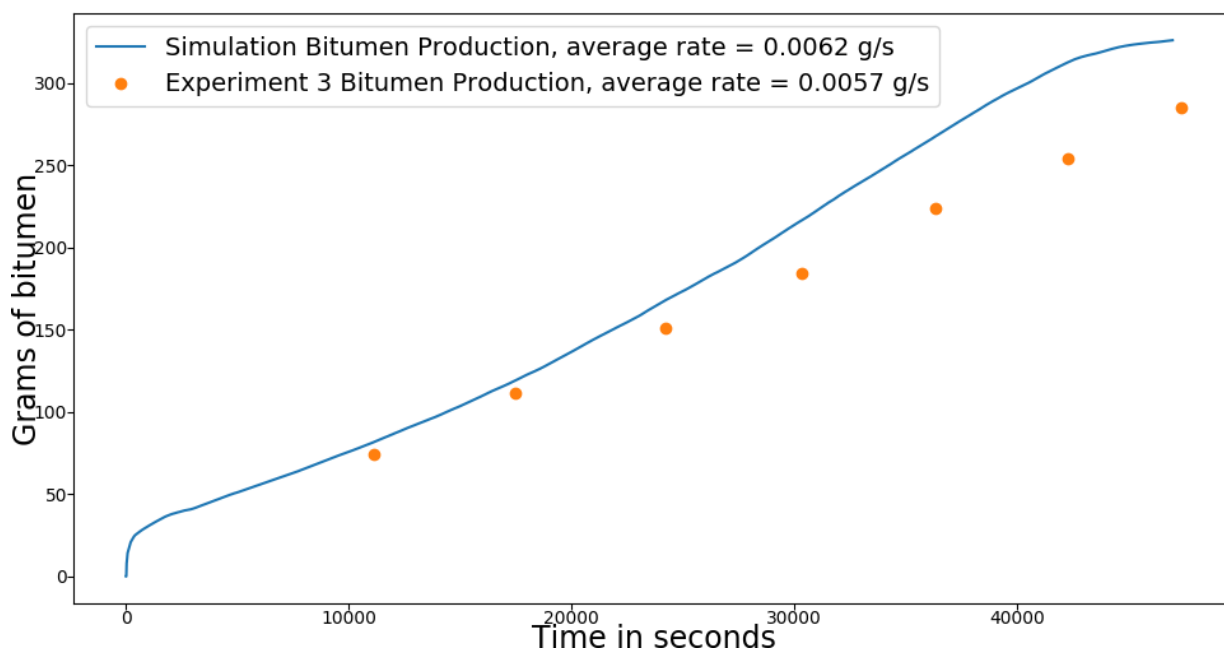
5.2.1 Bitumen Production

Figure 5.10: Cumulative bitumen production of simulation of experiment 3 in [1]

As can be observed qualitatively in Fig. 5.10 the simulation is predicting the production rate of bitumen with a certain degree of accuracy. The average rate of production from

experimental data is 0.0057 g/s of bitumen, whereas the simulation is predicting an average rate of production of 0.0062 g/s of bitumen, an overestimation of approximately 9%. The average rate is the metric of most interest with which to quantify a VAPEX simulation's validity, as it is the goal of any EOR method to produce oil.

It should be noted that an annulus geometry cannot be perfectly approximated by a two-dimensional domain in the simulation. The initial conditions set by the simulation were made to satisfy the spectral condition and approximate as best as possible the physics of a VAPEX experiment initial setup. The offset is therefore a way to negate the initial start-up dynamics of the VAPEX simulation that may be overestimating the initial production results. The steep initial production rate between $t = 0$ and $\approx t = 500$ are a direct result of the pre-saturated initial condition of the domain.
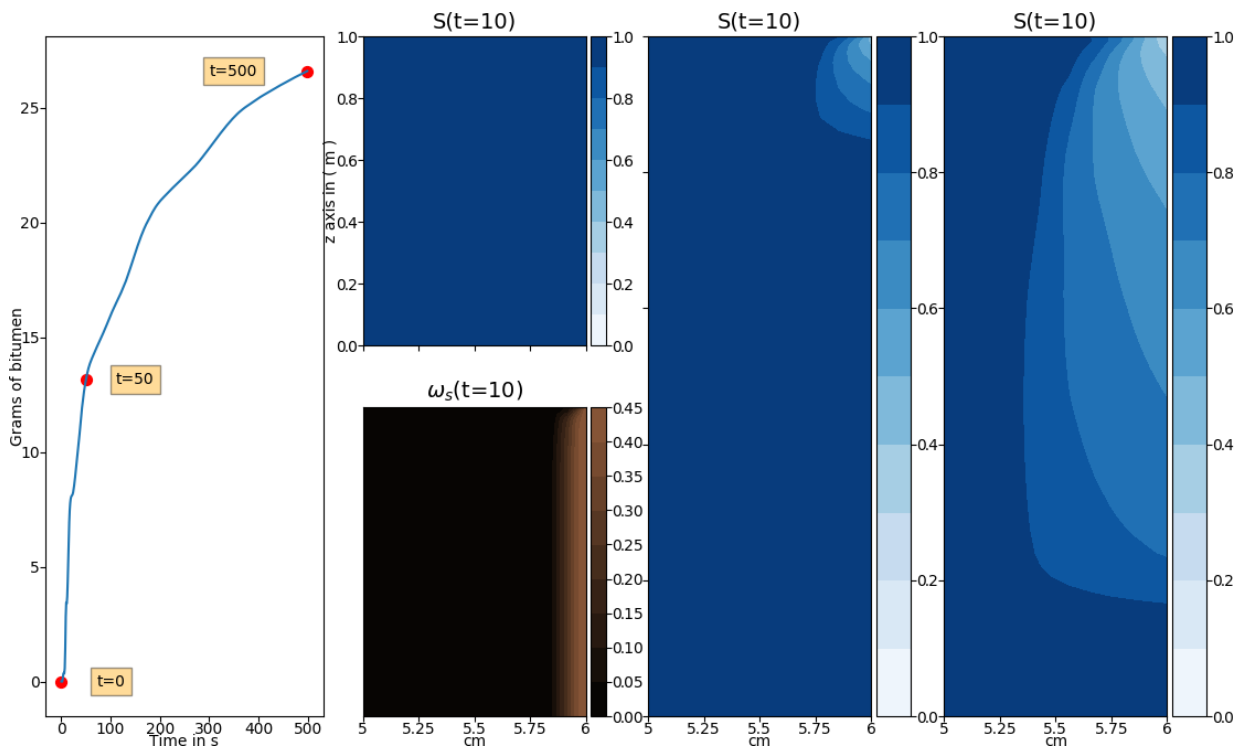
Initial Condition Drainage

Figure 5.11: Initial condition drainage for simulation of experiment 3 [1].

Figure 5.11 shows the evolution of the initial condition drainage. The first graph on

67

the left is a zoom in of Fig. 5.10 with three highlighted time stamps: $t = 0$ seconds, $t = 50$ seconds, and $t = 500$ seconds, within the last cm of the domain (5-6 cm). These times represent the initial conditions, the peak rate of initial condition drainage, and the point when the pre-drain is assumed to be concluded. The initial condition drainage visualized with a zoom in on the cumulative production graph for times $0 - 500$ seconds, the mass fraction in orange is the two dimensional equivalent of Fig. 4.7 showing the saturated bitumen having an exponential increase from left to right of butane until the Dirichlet condition of 0.45 is achieved at the right boundary. The initial condition for the saturation shown in the lower of the two graphs shows the fully saturated domain at the start of the simulation.

In the second graph from the right, at $t = 50$ seconds during peak initial condition drainage, we can observe that the domain is draining in the expected manner from the top down in the areas where bitumen has become mobile due the mass fraction of butane reducing the viscosity of the liquid phase. Those locations correspond to areas where the initial condition of butane is above 0.15 which is approximately the point where the mixture becomes mobile [46].

In the final graph we see the height of capillary rise realized in the lower right of the domain. This area will not drain, for capillarity is holding the liquid in place, but allows fluid to flow through. We take this point to be the end of the pre-drain, as it corresponds to the stabilization of the drainage rate from the maximum slope of drainage at $t = 50$. As is evidenced in Fig. 5.10 the production rate is stable from $t = 500$ seconds until the end of the pseudo-steady-state.

The initial condition drainage is an important phenomena to discuss in the simulation as it is the artefact of a numerical necessity. There is a basis in physical VAPEX experiments of this pre-drain. In experiment, "communication" must be established between the producer and injector ports. Communication is a pre-drain of the domain that linearly connects the injector port and the producer, as in experiment being replicated, by means of heating the domain. This is necessary in a VAPEX experiment in order to allow the process to begin at $t = 0$. If communication were not established, enough time for butane to diffuse, and bitumen mobilize between injector and producer before a vapour chamber could be established. Diffusion in that case would not occur linearly between the ports, but in all directions negating the vapour chamber formation before the experiment begins. Communication is discussed in [1], and is evidenced in Fig. 5.10 by the first data point collection time. Since communication is a requirement of experiment, the initial condition for our simulation has basis in replicating the physics of a VAPEX experiment, but as is evidenced in the simulations, the requirements for an offset value on production rates can be a nuisance numerically by overestimating production in the initial time frame.

68

Pseudo-Steady-State

The pseudo-steady-state for the VAPEX system is defined here as the period of time after the initial condition drainage, during which the vapour-chamber is growing and bitumen production rate is maintained at constant rate. During the pseudo-steady-state it is observed that continuously increasing production can be measured between $t = 500$ and $t = 35000$ in Fig. 5.12. This increase is expected when observing the arc length of the transition zone during the evolution of the vapour chamber from $t = 500$, Fig. 5.13 compared to $t = 22500$, Fig. 5.14. Production increases as the exposed bitumen becomes mobile, a rate that is directly proportional to the surface area of the transition zone.

The pseudo-steady-state for an experiment should end when the chamber growth touches the entire domain left to right. The top of the chamber has the fastest transverse growth, and so the top left of the domain is first to be exposed to the transition zone growth. The production rate will continue to increase slightly even after the end of the pseudo-steady-state as the bitumen is still being made mobile and flowing out of the domain.

The domain continues to drain after the left wall is reached, and although the production rates are no longer reflective of a realistic VAPEX domain, the simulation is still able to capture the same dynamics that are occurring in a closed domain VAPEX experiment. The transition zone continues to have tangential velocity approaching the $x = 0$ axis, and a vertical transition zone begins to descend from the top left down. The effect of a two-sided transition zone on production results in continued increasing production rates as the final portions of the bitumen domain are exposed to butane. The fully drained portion of the domain is also seen to be expanding from the top right as the capillary forces become equilibrated. When production rates start to reduce after $t = 35000$, the end of the pseudo-steady-state is declared.

An S-shaped curve was shown in works [32, 3, 1, 47, 36] as the classic vapour chamber shape for transient VAPEX experiments. With the saturation being profiled in Fig. 5.13, Fig. 5.14, and Fig. 5.15 as a gradient, direct visual confirmation of the S shape curved found in experiments is lost. Figure 5.16 is a view of the vapour chamber at $t = 25000$ in a binary colour scheme with a division at $S = 0.5$ to show the S shape curve is captured in the VAPEX simulation for the evolving vapour chamber.

The velocity profile of the VAPEX domain during the simulation provides insight into how the transition zone evolves. Figure 5.17, Fig. 5.18, and Fig. 5.19 show the saturation profile and a velocity field profile in the domain as they evolve. The velocity profile shows that fluid is transported tangentially away and parallel to the transition zone. The magnitude of the velocity of in the tangential direction when compared to the magnitude of
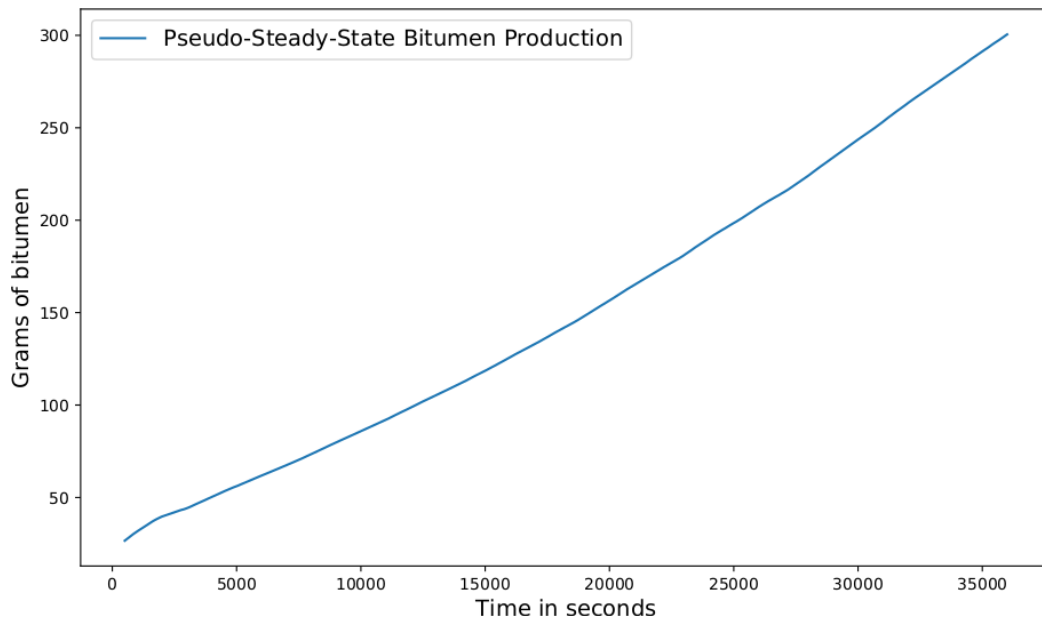
69

Figure 5.12: Pseudo-steady-state production for simulation of experiment 3
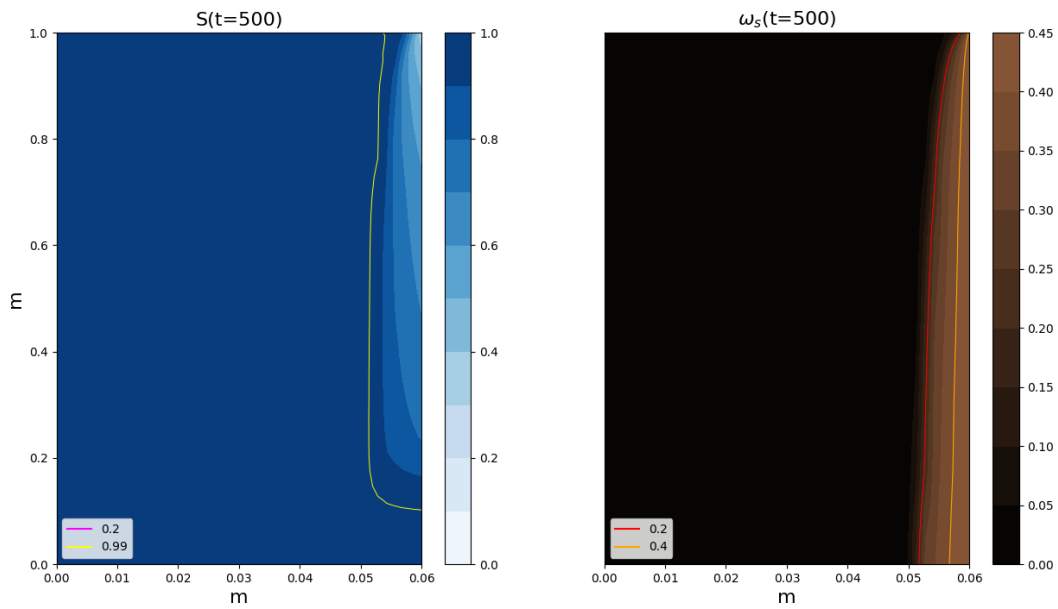

Figure 5.13: Saturation and mass fraction of butane at the start of pseudo-steady-state for simulation of experiment 3
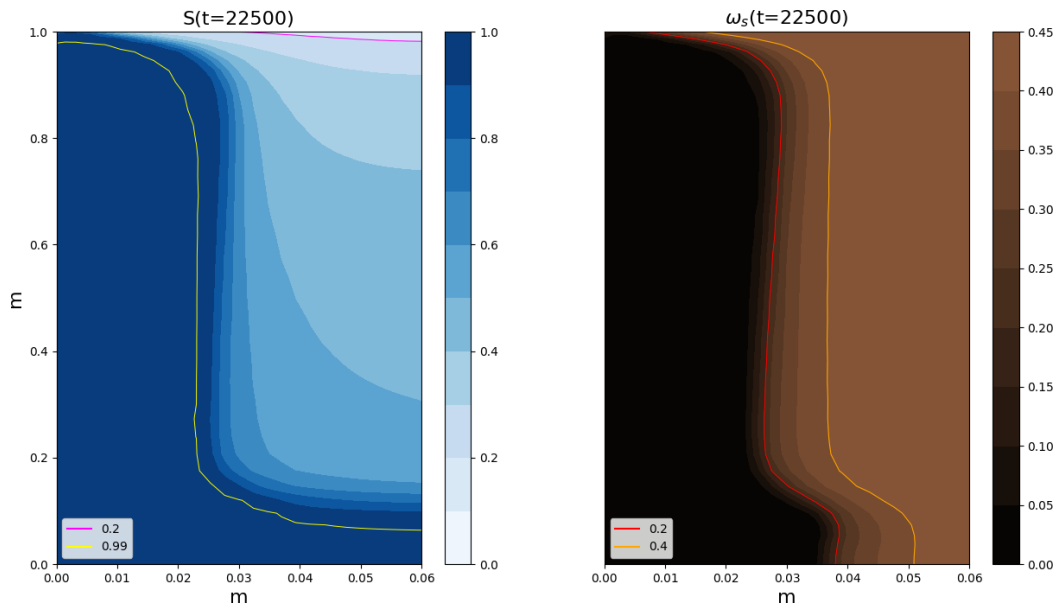
Figure 5.14: Saturation and mass fraction of butane at the point during pseudo-steady-state when vapour chamber reaches $x = 0$ axis for simulation of experiment 3
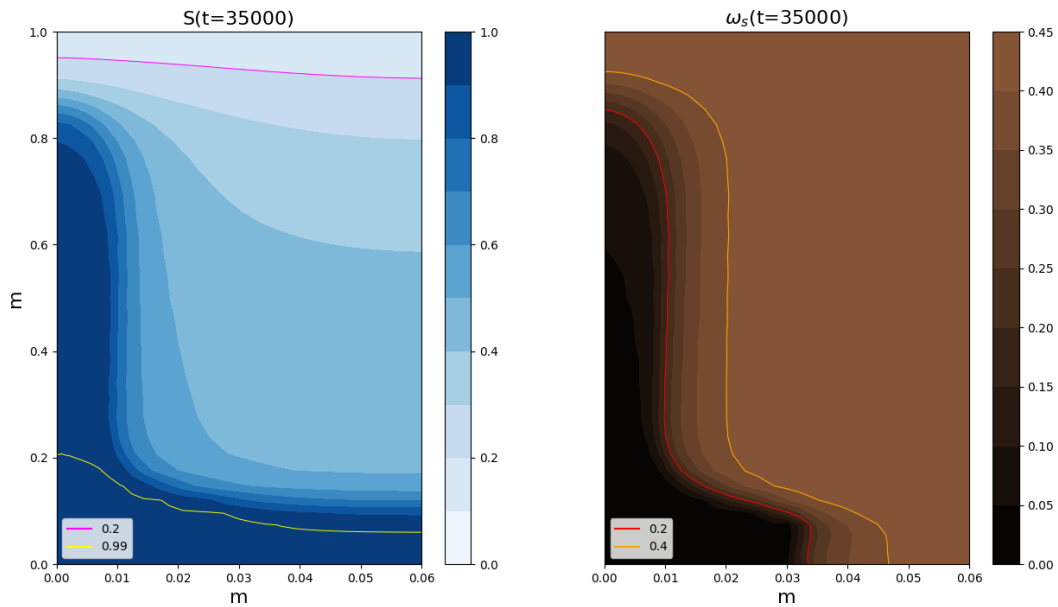

Figure 5.15: Saturation of the liquid phase and mass fraction of butane at the end of pseudo-steady-state for simulation of experiment 3

velocity in the direction of gravity is hard to gauge from the figures, but not inconsequential to the evolution of the VAPEX domain. The tangential velocity is how the domain is equilibrated with respect to how saturation is distributed across the domain. Gravity drainage is the primary mechanism for fluid movement in the domain, but capillary forces create a saturation gradient that is still measured vertically above the drainage outflow.

The butane saturation boundary condition of $\omega_s = 0.45$ at the right side of the domain extended into the drainage area of the lower-right. This was expected to skew the butane production in the liquid phase higher than discovered experimentally. In experiment 3 [1] the mass fraction of butane produced was averaged over the duration of the experiment was found to be $\omega_s = 0.38$. The average butane produced in the liquid phase during the pseudo-steady-state during the simulation of experiment 3 was found to be $\omega_s = 0.395$. The difference between simulated and experimental butane production is negligible.

5.2.2   Interphase Mass Transfer

During the pseudo-steady-state we are given the opportunity to evaluate the impact of phenomena occurring in the liquid phase. The derivation of the equation allows for the graphing of the interphase mass transfer term to show exactly where and how much mass is being added to the domain during vapour chamber evolution. By plotting the contribution the ability to examine the local effects of mass addition into the liquid phase is only capable in a simulation. Figure 5.20, Fig. 5.21, and Fig. 5.22 show the evolution of the saturation, mass fraction of butane, and the interphase mass transfer at times $t = 500$, $t = 22500$, and $t = 35000$.

The interphase mass transfer prefactor coefficient, a value set at 0.005 s^{-1} for this simulation, represents the only tunable parameter in the VAPEX model simulated. It was not tuned to generate results comparable to the experimental results, but rather tuned to an order of magnitude approximation based on mass transfer theory. The production rates for the simulated VAPEX model were higher than the experimental rates. This can be attributed to overestimating the interphase mass transfer coefficient as a slightly lower value would result in less butane liquid mass being introduced into the domain and would therefore slow production. It is also possible that the two-dimensional domain approximation of the annulus used in the experiment is responsible for the differences in production output. A third possibility is the lack of clearly defined outflow conditions, as the computational cost of allowing the entire bottom of the domain to drain was far less than imposing a outflow condition. The outflow of the domain is still restricted to areas where the viscosity has been reduced to the point of mobility, which provides a naturally

occurring outflow area, but the rates would be impacted by restricting that area to a constant area outflow.

5.3 Solution of the VAPEX model for a second set of experimental parameters

The model solution replicating [1] experiment 3 was shown to predict production rates to within 10% of the reported rates, but for the model to be robust it must be invariant to experimental parameter changes. A second experiment, experiment 1, in [1] provides varied parameters in the same annulus architecture. The glass beads used in experiment 1 were twice the diameter of experiment 3 resulting in a different permeability and porosity, and also required updating the dispersion coefficients. A table of parameters for experiment 1 are included in table 5.4.

Parameter	Value	Unit
Inner cylinder outer diameter	2	inches
Outer cylinder inner diameter	2.5	inches
Height	1	metre
Grain size	1.19	microns
Porosity	0.38	unit-less
Permeability	1123	Darcy
Time	600	minutes
Bitumen density	980	kg/m^3
Butane density	573	kg/m^3
Bitumen viscosity	23.2	kg/ms
Butane viscosity	1.71×10^{-4}	kg/ms

Table 5.4: Table of parameters for experiment 1 [1]

By again finding an approximation to the interphase mass transfer prefactor by estimating the saturation at $S = 0.9$ and mass fraction of $\omega_s = 0.15$, the coefficient calculated in Eqn. (3.32) give a value of $0.00422 \ s^{-1}$ which is rounded down to $0.004 \ s^{-1}$. The production rates for the simulation of experiment 1 are found in Fig. 5.23. The evolution of the domain for the simulation of experiment 1 is qualitatively similar to the evolution of simulation of experiment 3. The production rate of the simulated experiment 1 is

0.0148 grams per second compared to the production average from experiment 1 of 0.0138 grams per second. This represents a prediction to within 4% of the experimental production. The ability of the model to predict production rates to within 4% without tuning to specific parameters implies the model can handle variable permeability accurately. The difference in production rates during the pseudo-steady-state from simulation compared to experimental is once again attributed to the constant prefactor for the interphase mass transfer not being able to fully describe the physics occurring within a pore, and by the two-dimensional approximation to the annulus experimental domain not fully capturing the required geometry.

5.4   Heterogeneity

The scaling of capillary pressure using the Leverett J function brings allows for the possibility of experimenting with variable permeability fields within a VAPEX domain. Using a cross correlated permeability field generator in [48] a spatially varying permeability field with a mean absolute permeability equal to the homogenous permeability of experiment 3 is solved for. Figure 5.24, Fig. 5.25, and Fig. 5.26 shows the domain evolution of the heterogeneous permeability field domain, simulated using the same parameters as experiment 1 in [1] found in table 5.2.

Capillarity holds the liquid in areas where the permeability is lower (shown in red) and drains first from areas with higher permeability (shown in blue). The intrusion of the transition zone into the bitumen is now restricted to areas that can drain and no longer forms the S-shaped curve from homogenous permeability fields. Diffusion will eventually increase the mass fraction of butane in areas trapped by low permeability, and provided the interfacial tension is reduced and the liquid can drain, eventually the domain will be emptied. The permeability of the entire field has an average of 300 Darcy, the same as the permeability of the experiment 3 so a comparison of production rates is shown in Fig. 5.27. The rates of bitumen production differ by 0.0003 grams per second, the heterogeneous permeability field having an average production rate $\approx$ 5% higher than the original experiment three simulation. This agrees with the results in [32] where the researcher conducted experiments with heterogeneous stratified permeability fields and compared production rates to the homogeneous results.
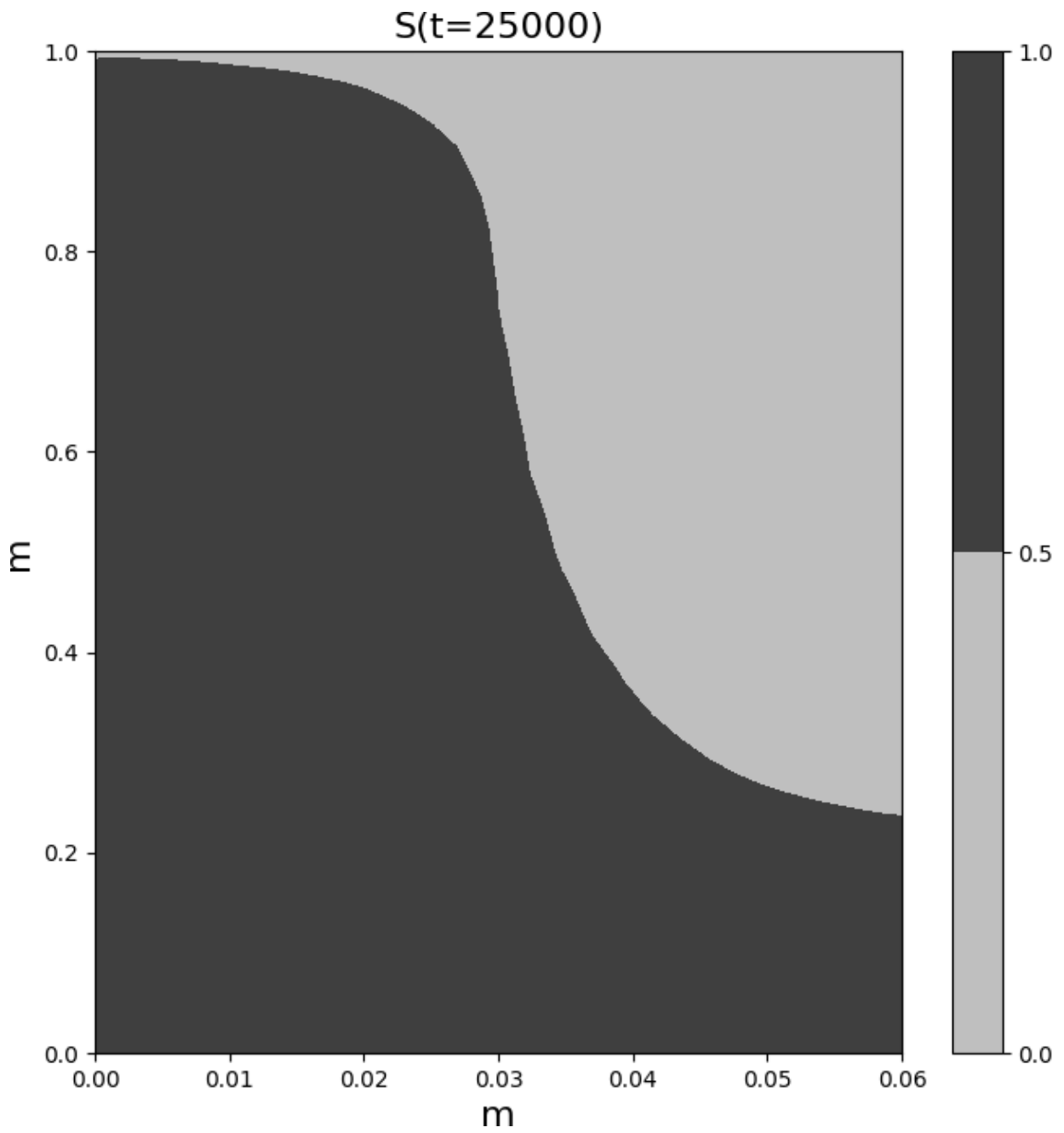
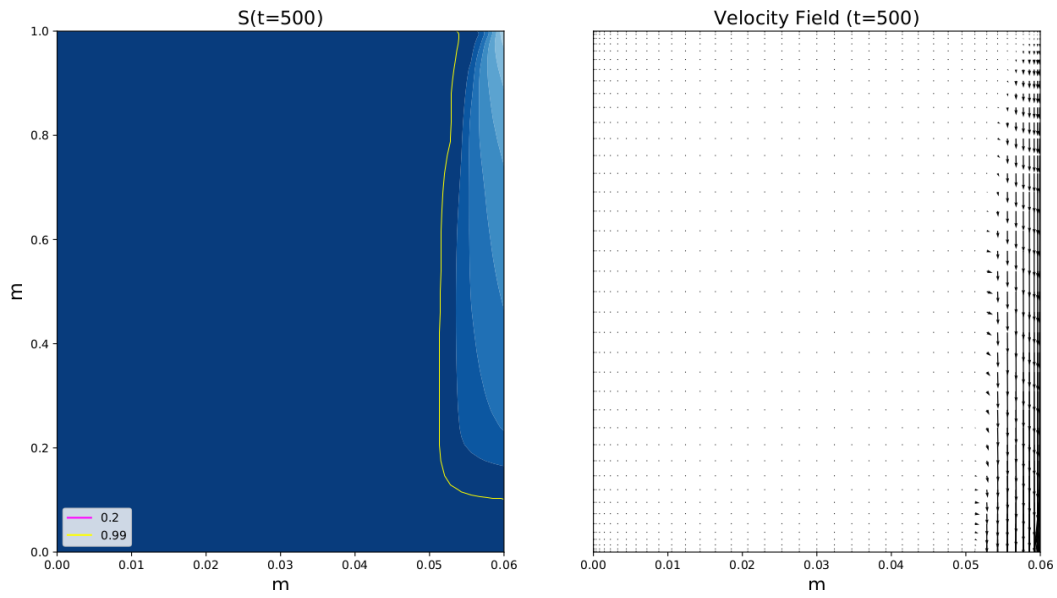Figure 5.16: Binary saturation for qualitative comparison of S shaped curve with $S = 0.5$r.

Figure 5.17: Saturation and velocity field at $t = 500$, the start of pseudo-steady-state for simulation of experiment 3
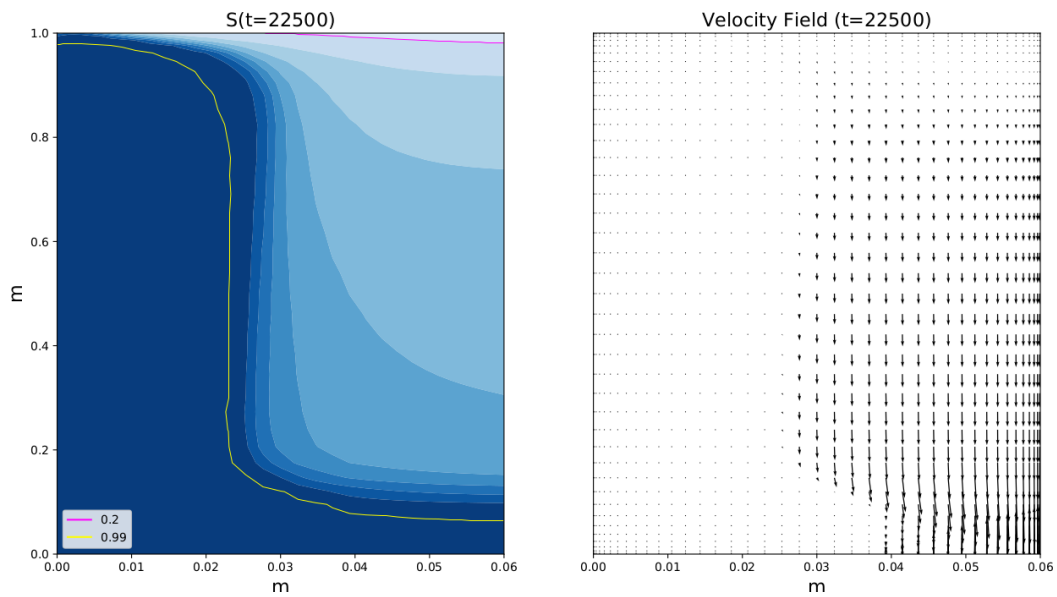

Figure 5.18: Saturation and velocity field at $t = 22500$, the point during pseudo-steady-state when vapour chamber reaches $x = 0$ axis for simulation of experiment 3
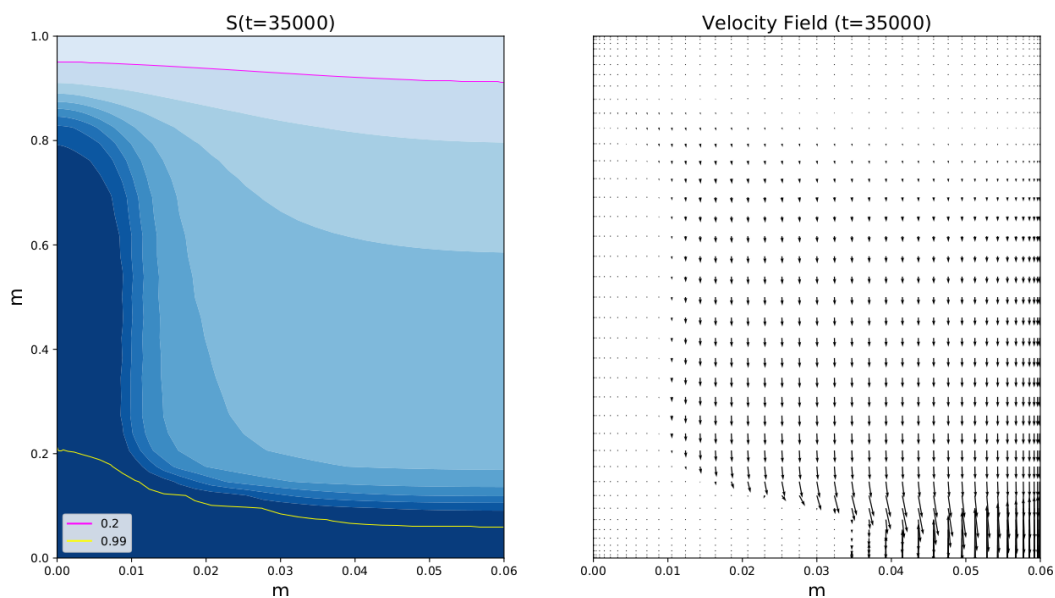
Figure 5.19: Saturation and velocity field at $t = 35000$, the end of pseudo-steady-state for simulation of experiment 3
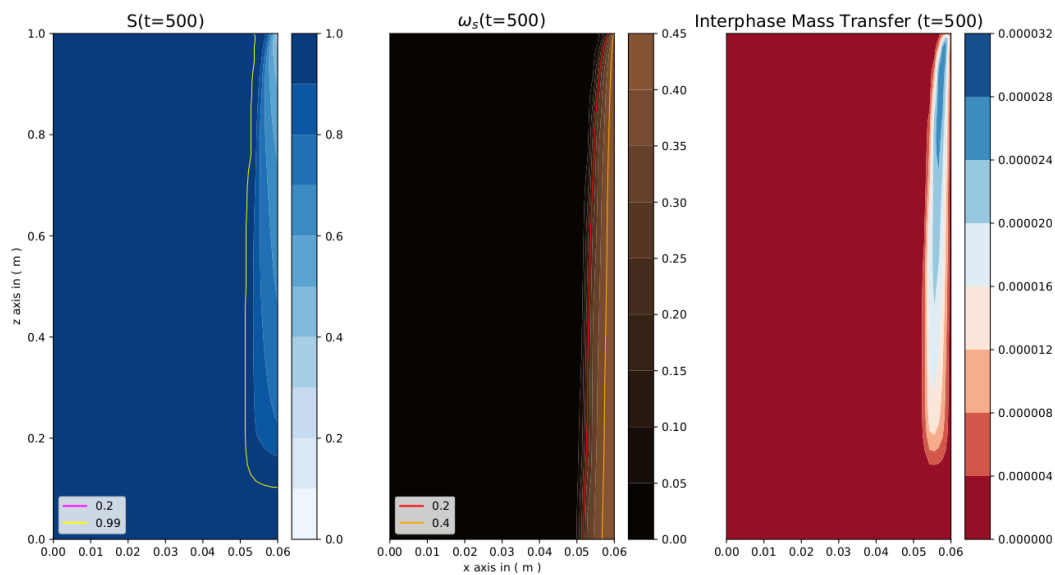

Figure 5.20: Saturation, mass fraction of butane, and interphase mass transfer contribution at $t = 500$, the start of pseudo-steady-state for simulation of experiment 3
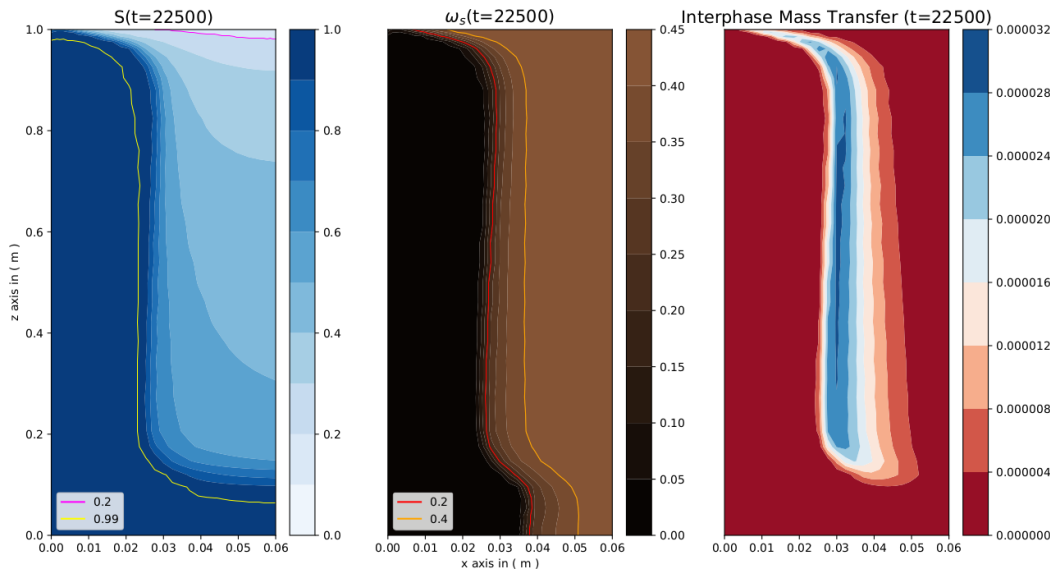
Figure 5.21: Saturation, mass fraction of butane, and interphase mass transfer contribution at $t = 22500$, the point during pseudo-steady-state when vapour chamber reaches $x = 0$ axis for simulation of experiment 3
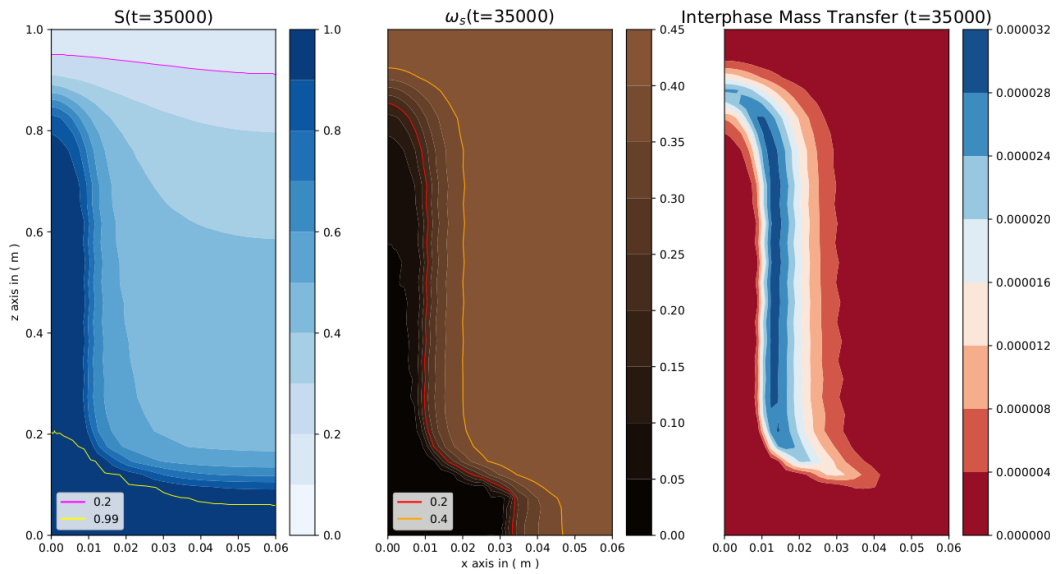

Figure 5.22: Saturation, mass fraction of butane, and interphase mass transfer contribution at $t = 35000$, the end of pseudo-steady-state for simulation of experiment 3

Figure 5.23: Production rate for the simulation of experiment 1 in [1]
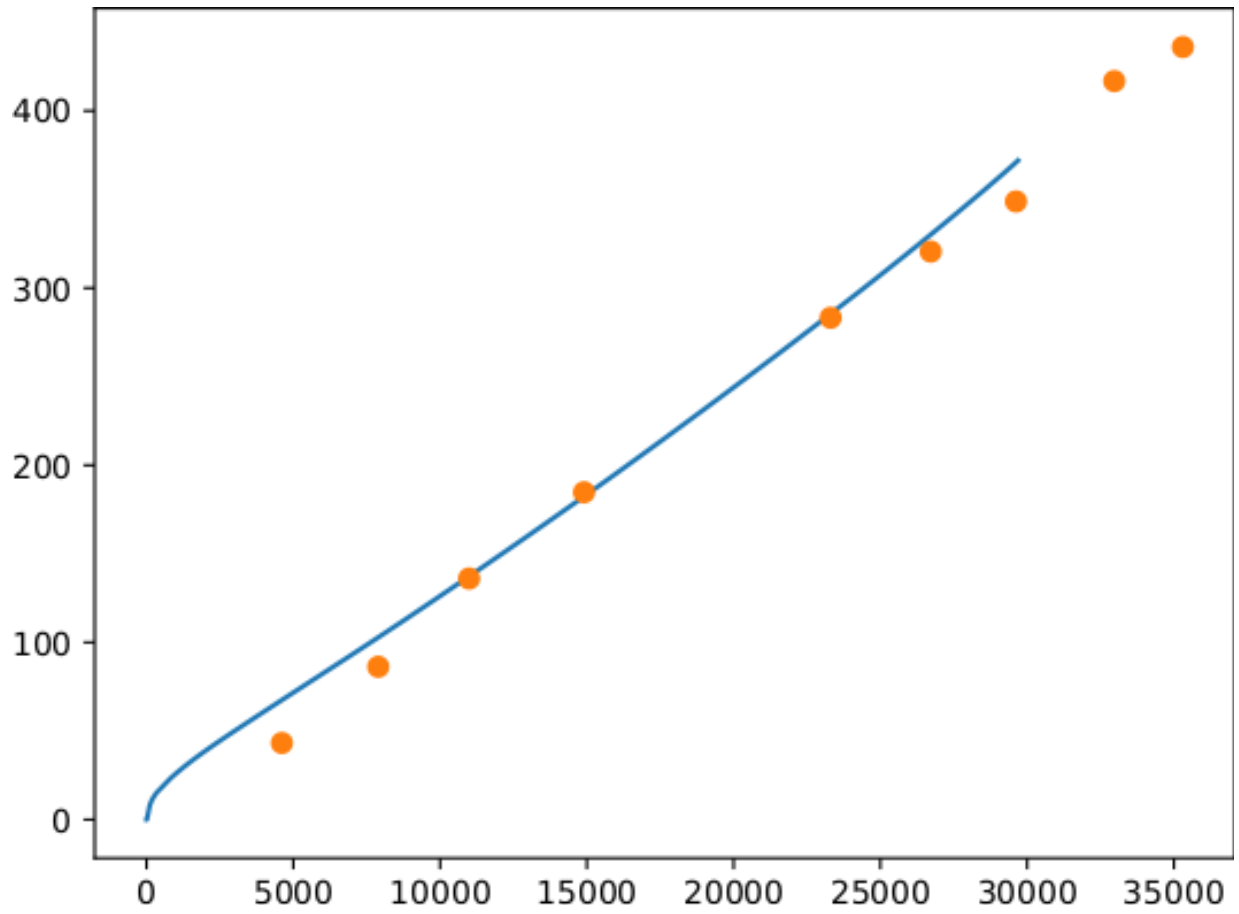
Figure 5.24: Saturation, mass fraction of butane, interphase mass transfer contribution, and scaled permeability field at $t = 500$ for a heterogeneous permeability field solution

Figure 5.25: Saturation, mass fraction of butane, interphase mass transfer contribution, and scaled permeability field at $t = 1500$ for a heterogeneous permeability field solution
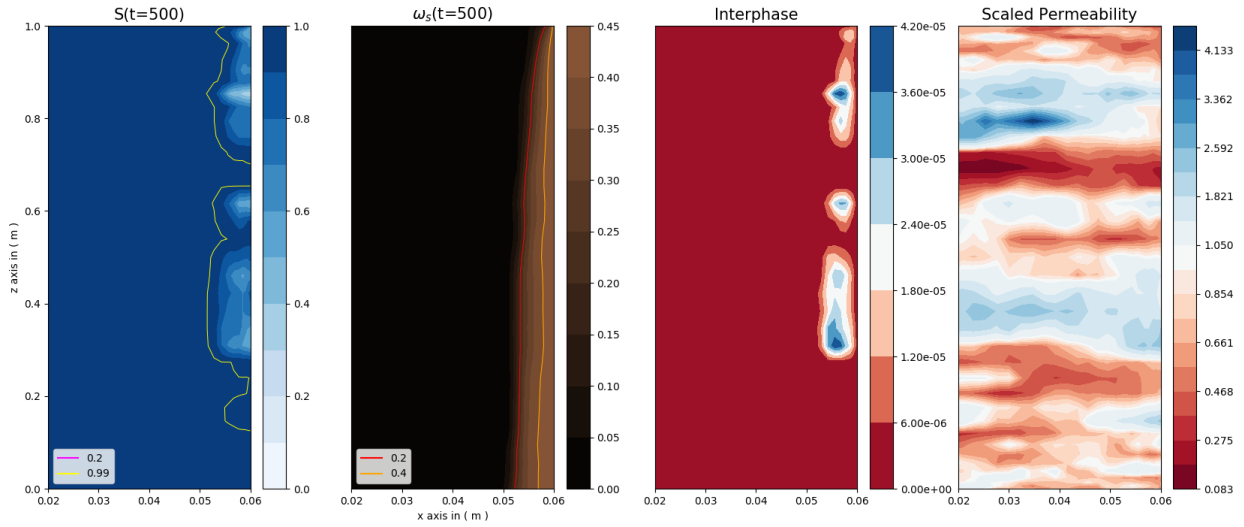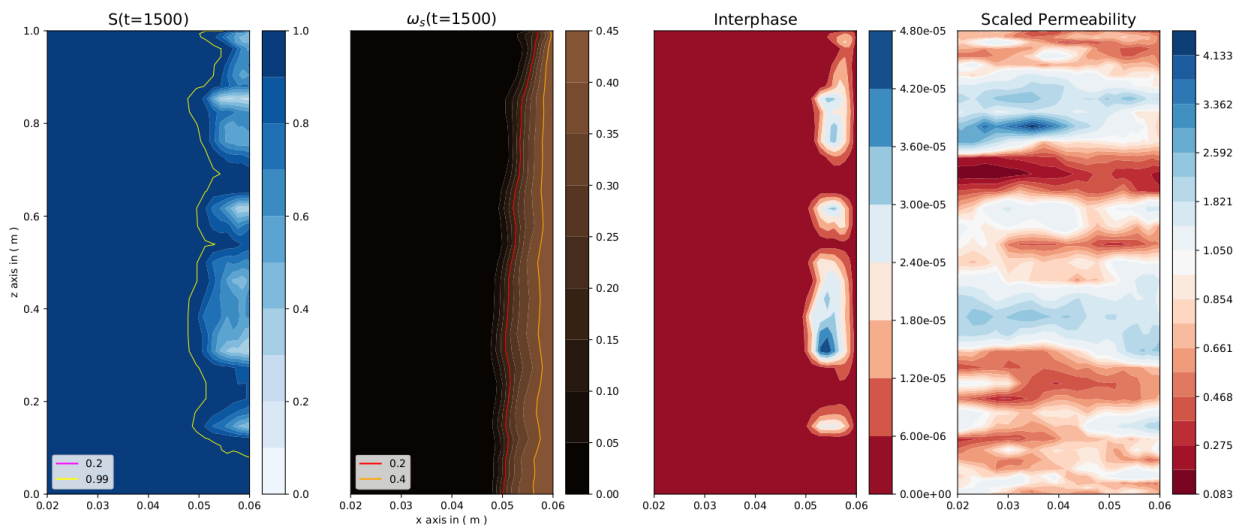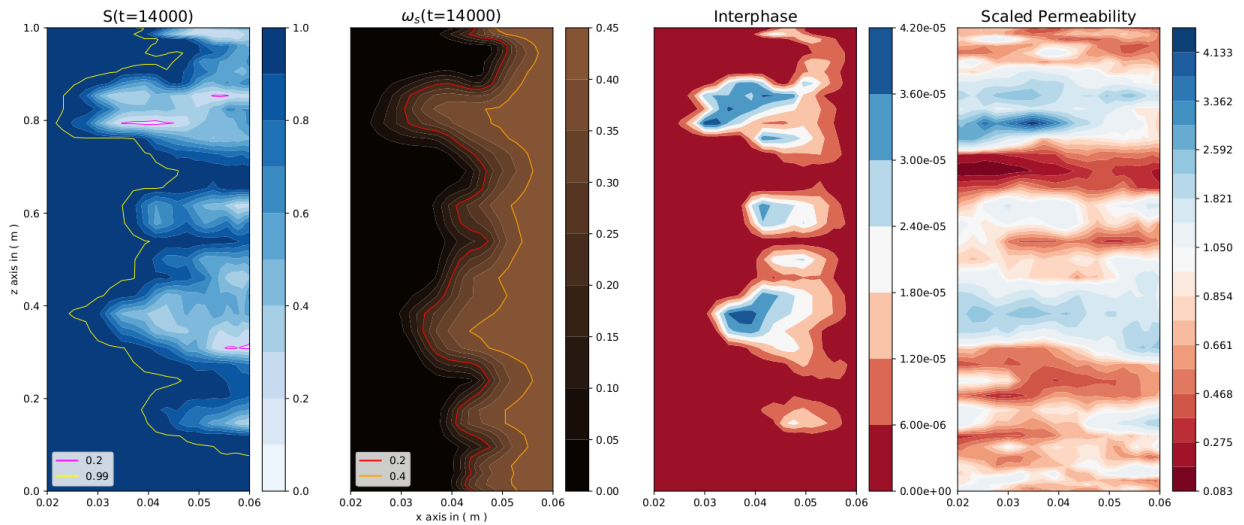
Figure 5.26: Saturation, mass fraction of butane, interphase mass transfer contribution, and scaled permeability field at $t = 14000$ for a heterogeneous permeability field solution
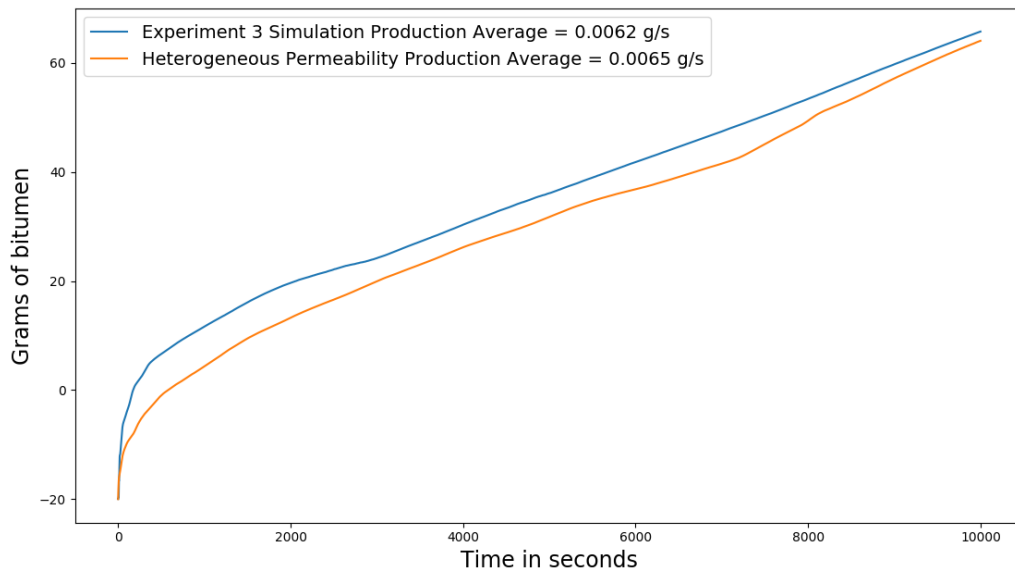

Figure 5.27: Comparison of bitumen production and production rates of experiment 3 simulation and heterogeneous permeability field simulation.

Chapter 6

Concluding Summary

The VAPEX model proposed in this project was capable of predicting production of bitumen of experiments accurately, and showed invariance in accuracy when experimental parameters are changed. The Chebyshev spectral collocation method proved adequate in solving the coupled PDE model for VAPEX.

6.1 Conclusions

The model proposed in this work is derived from conservation of mass, and populated with empirical correlations from previous works which are specific to the modelled system. With the exception of the interphase mass transfer term, there are no tunable parameters in the model used to match an experiment in order to form a prediction of bitumen production. The interphase mass transfer term was not chosen arbitrarily in this work, but approximated from mass transfer theory and interfacial area empirical correlations of two phase flow in porous media. The approximation of a constant prefactor in the interphase mass transfer term was used to verify that production of bitumen can be predicted from a VAPEX experiment. Therefore, there are no tunable parameters in this model that would be used to match production rates. This implies the implementation of physics and correlation was appropriate.

The high order polynomial solutions provided by the Chebyshev spectral collocation numerical method were extremely helpful in solving this VAPEX model with minimal grid points. The duration of simulations is prohibitively long for few grid points due to the non-linearity of the model, so any means of reducing the computational time must be

explored. The requirement of a spectral method to have smooth initial conditions and limited capability on the boundary condition implementations, specifically with respect to convergence time when implementing an outflow condition, were mitigated by the approximations to physical experiments of VAPEX with respect to communication of the injector well and producer well. The initial saturation of butane in the bitumen mixture was likely an overestimation of the communication requirement, as was evidenced by the offset of bitumen production when compared to experimental production. The metric of interest to a potential VAPEX implementation would be the rate at which production of bitumen could be achieved, that pseudo-stead-state rate being established in these simulations with reasonable accuracy (to within 10% of experimental rates).

The evolution of the vapour chamber is another metric by which the solutions to the VAPEX model derived can be compared to experimentation. The apparent S-shaped curve of the transition zone was well established in the simulation saturation domain indicates that the solution of the system is behaving as expected based on literature and experimentation on VAPEX systems.

6.2 Recommendations for future work

- Attempt VAPEX using a discontinuous method, such as the discontinuous Galerkin family of finite element methods. The sharp interface of the mass fraction solution is prohibitively hard to solve for in a spectral environment due to the Gibbs phenomenon. Scale up would be easier with an adaptive mesh refinement scheme, as spectral fails to properly capture the transition zone interface efficiently in larger domains.

- Include variable density in the model. It is already obvious that the density of the liquid phase changes, and although there may be no major benefit to re-deriving and solving a system of three coupled domains, it is understood from the work of [46] that swelling of bitumen when exposed to butane vapour is non-negligible. Insight into how much of an impact swelling would have on production rates and diffusion rates would provide more insight into VAPEX as a method of extended oil recovery.

- Add an energy equation, and account for solvent condensation. There are experimental and field studies in using a VAPEX method which introduces warm butane vapour into a domain with the intention of condensing in the porous medium. This would fundamentally change the problem from one of mass transfer between a gaseous and

a liquid phase, to one of mixing of two liquid phases (bitumen and condensate-rich phase).

- Further explore the effect of heterogeneity on capillary trapping.

References

[1] Sindy Pui Yin Tam. *VAPEX Experiments in an Annular Packing of Glass Beads and the Numerical Simulation of VAPEX using Comsol ®*. Masc, University of Waterloo, 2007.

[2] M A Ioannidis, I Chatzis, C Lemaire, and R Perunarkilli. Unsaturated hydraulic conductivity from nuclear magnetic resonance measurements. 42(February):1–6, 2006.

[3] R M Butler and Igor Mokrys. Solvent Analog Model of Steam Assisted Gravity Drainage, 1989.

[4] Leslie Anne James. *Mass transfer mechanisms during the solvent recovery of heavy oil*. PhD thesis, University of Waterloo, Waterloo, Ontario, Canada, 2009.

[5] D. Klotz, K. P. Seiler, H. Moser, and F. Neumaier. Dispersivity and velocity relationship from laboratory and field experiments. *Journal of Hydrology*, 45(3-4):169–184, 1980.

[6] C E Schaefer, D A Dicarlo, and M J Blunt. Experimental measurement of air-water interfacial area during gravity drainage and secondary imbibition in porous media. *Water Resources Research*, 36(4):885–890, 2000.

[7] R B Bird, W E Stewart, and E N Lightfoot. *Transport Phenomena*. Wiley International edition. Wiley, 2007.

[8] Lloyd N Trefethen. *Spectral Methods in MatLab*. Society for Industrial and Applied Mathematics, Philadelphia, PA, USA, 2000.

[9] Giancarlo Giacchetta, Mariella Leporini, and Barbara Marchetti. Economic and environmental analysis of a Steam Assisted Gravity Drainage (SAGD) facility for oil recovery from Canadian oil sands. *Applied Energy*, 142:1–9, 2015.

[10] R M Butler and Igor J Mokrys. Solvent analog model of steam-assisted gravity drainage. *AOSTRA Journal of Research*, 5, 1989.

[11] Daniel Yergin. *The Prize: The Epic Quest for Oil, Money, & Power*. Simon & Schuster, 1991.

[12] David Talbot. The End of Easy Oil. *MIT Technology Review*, 2010.

[13] Larry W Lake. *Enhanced Oil Recovery*. Prentice-Hall, Inc., Englewood Cliffs, New Jersey, 1989.

[14] Carlton Beal. The Viscosity of Air, Water, Natural Gas, Crude Oil and Its Associated Gases at Oil Field Temperatures and Pressures, 1946.

[15] Y Wen and A Kantzas. Evaluation of Heavy Oil / Bitumen-Solvent Mixture Viscosity Models. pages 1–8, 2004.

[16] J Peter Findlay. *The Future of the Canadian Oil Sands: Growth potential of a unique resource amidst regulation, egress, cost, and price uncertainty*. Number February. 2016.

[17] Steve E Hrudey and Zhenghe Xu. Environmental and Health Impacts of Canada ' s Oil Sands Industry. *The Royal Society of Canada*, (December):22, 2010.

[18] Franck Stefani, Nathalie Isabel, Marie-Josée Morency, Manuel Lamothe, Simon Nadeau, Denis Lachance, Edith H. Y. Li, Charles Greer, Étienne Yergeau, Bradley D. Pinno, and Armand Séguin. The impact of reconstructed soils following oil sands exploitation on aspen and its associated belowground microbiome. *Scientific Reports*, 8(1):2761, 2018.

[19] Sarah M. Jordaan. Land and water impacts of oil sands production in Alberta. *Environmental Science and Technology*, 46(7):3611–3617, 2012.

[20] M.D. MacKinnon Boerger and Hans. Description of two treatment methods for detoxifying oil sands tailings pond water. *Water Pollution Resource*, (August), 2018.

[21] P. Haghighat and B. B. Maini. Role of asphaltene precipitation in VAPEX process. *Journal of Canadian Petroleum Technology*, 49(3):14–21, 2010.

[22] JE Gontijo and K Aziz. A simple analytical model for simulating heavy oil recovery by cyclic steam in pressure-depleted reservoirs. *SPE Annual Technical Conference and Exhibition*, page SPE 13037, 1984.

[23] Lesley Anne James. *Mass Transfer Mechanisms during the Solvent Recovery of Heavy Oil*. PhD thesis, University of Waterloo, 2009.

[24] Swapan Kumar Das. In situ recovery of heavy oil and bitumen using vaporized hydrocarbon solvents. 1995.

[25] Roger M Butler and Igor J Mokrys. A new process (V APEX) for recovering heavy oils using hot water and hydrocarbon vapour. *Journal of Canadian Petroleum Technology*, 30(1):97–106, 1991.

[26] Swapan K Das and Roger M Butler. 99/00196 Mechanism of the vapour extraction process for heavy oil and bitumen. *Fuel and Energy Abstracts*, 40(1):20, 1999.

[27] R M Butler I J Mokrys. Closed-Loop Propane Extraction Method for the Recovery of Heavy Oils and Bitumens Underlain B.

[28] Amin Daryasafar and Khalil Shahbazi. The effect of different solvents on the density of undersaturated athabasca bitumen: Application in VAPEX and ES-SAGD. *Petroleum Science and Technology*, 36(3):222–226, 2018.

[29] R El-Haj, A Lohi, and S R Upreti. Experimental determination of butane dispersion in vapor extraction of heavy oil and bitumen. *Journal of Petroleum Science and Engineering*, 67:41–47, 2009.

[30] Lixing Lin, Fanhua Zeng, and Yongan Gu. A circular solvent chamber model for simulating the VAPEX heavy oil recovery process. *Journal of Petroleum Science and Engineering*, 118:27–39, 2014.

[31] Hongze Ma, Gaoming Yu, Yuehui She, and Yongan Gu. A parabolic solvent chamber model for simulating the solvent vapor extraction (VAPEX) heavy oil recovery process. *Journal of Petroleum Science and Engineering*, 149(October 2016):465–475, 2017.

[32] A R Oduntan and University of Waterloo. Department of Chemical Engineering. *Heavy Oil Recovery Using the VAPEX Process: Scale-up and Mass Transfer Issues*. Masc, 2001.

[33] Spri Project and Agreement Number. Winter Pilot Expansion SPRI Final Report.

[34] Adam Szymkiewicz. *Modelling Water Flow in Unsaturated Porous Media: Accounting for Nonlinear Permeability and Material Heterogeneity*, volume 9. 2013.

[35] L. A. Richards. Capillary conduction of liquids through porous mediums. *Journal of Applied Physics*, 1(5):318–333, 1931.

[36] Lixing Lin, Fanhua Zeng, and Yongan Gu. A circular solvent chamber model for simulating the VAPEX heavy oil recovery process. *Journal of Petroleum Science and Engineering*, 118:27–39, 2014.

[37] M. C. Leverett. Capillary Behavior in Porous Solids. *Journal fur die Reine und Angewandte Mathematik*, 1958(200):129–139, 1958.

[38] M. Th. van Genuchten. A Closed-form Equation for Predicting the Hydraulic Conductivity of Unsaturated Soils1, 1980.

[39] S K Das. *In-situ recover of heavy oil and bitumen using vaporized hydrocarbon solvents*. PhD thesis, University of Calgary, Calgary, Alberta, Canada, 1995.

[40] W.R. Shu. A Viscosity Correlation for Mixtures of Heavy Oil, Bitumen, and Petroleum Fractions. *Society of Petroleum Engineers Journal*, 24(3):277–282, 1984.

[41] J. H. Donaldson, J. D. Istok, and K. T. O'Reilly. Dissolved gas transport in the presence of a trapped gas phase: Experimental evaluation of a two-dimensional kinetic model, 1998.

[42] V G Levich. *Physicochemical hydrodynamics*. Prentice-Hall international series in the physical and chemical engineering sciences. Prentice-Hall, 1962.

[43] J C Mason and D C Handscomb. *Chebyshev Polynomials*. CRC Press, 2002.

[44] J P Boyd. *Chebyshev and Fourier Spectral Methods: Second Revised Edition*. Dover Books on Mathematics. Dover Publications, 2001.

[45] R Peyret. *Spectral Methods for Incompressible Viscous Flow*. Applied Mathematical Sciences. Springer New York, 2002.

[46] L A James and I Chatzis. Mass Transfer Coefficients in Vapour Extraction (VAPEX) - Extended Abstract. *Canadian International Petroleum Conference*, page 5, 2007.

[47] Hongze Ma, Gaoming Yu, Yuehui She, and Yongan Gu. A parabolic solvent chamber model for simulating the solvent vapor extraction ({VAPEX}) heavy oil recovery process. *Journal of Petroleum Science and Engineering*, 149:465–475, 2017.

[48] M. J.L. Robin, A. L. Gutjahr, E. A. Sudicky, and J. L. Wilson. Cross-correlated random field generation with the direct Fourier Transform Method. *Water Resources Research*, 29(7):2385–2397, 1993.